FIRST-PRINCIPLES STUDY OF ELECTRONIC AND OPTICAL PROPERTIES OF ALKALI METAL INTERCALATED TRANSITION METAL DICHALCOGENIDES

THANUNDON KONGNOK

A Thesis Submitted in Partial Fulfillment of the Requirements for the

Degree of Doctor of Philosophy in Applied Physics

Suranaree University of Technology

Academic Year 2021

การศึกษาคุณสมบัติเชิงอิเล็กทรอนิกส์และเชิงแสงของสารกลุ่มทรานซิชั่นเมทัลไดแคลโคจิไนด์ที่แทรกชั้นด้วยโลหะแอลคาไลโดยวิธีเฟิร์สทพรินซิเพิล

นายฐานันดร กงนอก

วิทยานิพนธ์นี้เป็นส่วนหนึ่งของการศึกษาตามหลักสูตรปริญญาวิทยาศาสตรดุษฎีบัณฑิต
สาขาวิชาฟิสิกส์ประยุกต์
มหาวิทยาลัยเทคโนโลยีสุรนารี
ปีการศึกษา 2564

FIRST-PRINCIPLES STUDY OF ELECTRONIC AND OPTICAL PROPERTIES OF ALKALI METAL INTERCALATED TRANSITION METAL DICHALCOGENIDES

Suranaree University of Technology has approved this thesis submitted in partial fulfillment of the requirements for the Degree of Doctor of Philosophy

Thesis Examining Committee

_____

(Assoc. Prof. Dr. Panomsak Meemon)

Chairperson

_____

(Assoc. Prof. Dr. Sirichok Jungthawan)

Member (Thesis Advisor)

_____
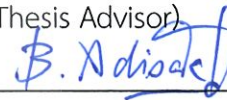
(Assoc. Prof. Dr. Adisak Boonchun)

Member

_____

(Assoc. Prof. Dr. Pakpoom Reunchan)

Member

_____

(Asst. Prof. Dr. Suwit Suthirakun)

Member

_____

(Dr. Ittipon Fongkaew)

Member

_____

(Assoc. Prof. Dr. Chatchai Jothityangkoon)

Vice Rector for Academic Affairs

and Quality Assurance

_____

(Prof. Dr. Santi Maensiri)

Dean of Institute of Science

ฐานันดร กงนอก : การศึกษาคุณสมบัติเชิงอิเล็กทรอนิกส์และเชิงแสงของสารกลุ่มทราน
ซิชั่นเมทัลไดแคลโคจิไนด์ที่แทรกชั้นด้วยโลหะแอลคาไลโดยวิธีเฟิร์สทพรินซิเพิล (FIRST-
PRINCIPLES STUDY OF ELECTRONIC AND OPTICAL PROPERTIES OF ALKALI
METAL INTERCALATED TRANSITION METAL DICHALCOGENIDES) อาจารย์ที่ปรึกษา :
รองศาสตราจารย์ ดร.สิริโชค จึงถาวรรณ, 109 หน้า.

คำสำคัญ : โครงสร้างเป็นชั้นซ้อนทับกัน/การแทรกตัวระหว่างชั้น

MoS_2 เป็นสารที่มีโครงสร้างเป็นชั้นรูปร่างคล้ายรวงผึ้งซ้อนทับกัน แต่ละชั้นดึงดูดกันแบบ
อ่อน ๆ ด้วยแรงแวนเดอวาลส์ ทำให้สามารถปรับเปลี่ยนโครงสร้างอิเล็กทรอนิกส์ได้โดยการแทรก
โลหะเข้าไปที่ช่องว่างระหว่างชั้น งานวิจัยนี้ศึกษาผลของการแทรกโลหะแอลคาไลโดยวิธีเฟิร์สทพรินซิ
เพิล ผลจากการคำนวณแสดงการขยายตัวอย่างมากของช่องว่างระหว่างชั้นและการเติมอิเล็กตรอน
จากโลหะแอลคาไลไปที่แถบการนำ การขยายตัวของช่องว่างระหว่างชั้นนั้นเห็นได้ชัดว่าเพิ่มขึ้นตาม
ขนาดอะตอมของโลหะ และการขยายนั้นยังทำให้ชนิดของช่องว่างแถบพลังงานเปลี่ยนจากแบบไม่ตรง
เป็นแบบตรงได้เนื่องจากปฏิกิริยาระหว่างชั้นที่ลดลง ค่าคงที่ของแลททิซตามแนวระนาบขยาย
เนื่องจากแรงผลักของไฟฟ้าสถิต คุณสมบัติอื่นที่สามารถนำไปเปรียบเทียบกับการทดลองได้ เช่น
ค่าคงที่เชิงโครงสร้าง กำแพงพลังงานของการแพร่กระจาย และค่าสัมประสิทธิ์การดูดกลืนยังถูก
คำนวณอีกด้วย ทั้งนี้จากผลการคำนวณบ่งชี้ให้เห็นว่าเราสามารถปรับเปลี่ยนโครงสร้างอิเล็กทรอนิกส์
ของสารกลุ่มทรานซิชั่นเมทัลไดแคลโคจิไนด์เพื่อนำไปประยุกต์ใช้กับอุปกรณ์อิเล็กทรอนิกส์เชิงแสงได้
โดยการใช้ขนาดอะตอมที่แตกต่างกันและการเปลี่ยนความเข้มข้นของโลหะ

สาขาวิชาฟิสิกส์   ลายมือชื่อนักศึกษา_____ฐานันดร กงนอก____
ปีการศึกษา 2564   ลายมือชื่ออาจารย์ที่ปรึกษา_____สิริโชค_____

THANUNDON KONGNOK : FIRST-PRINCIPLES STUDY OF ELECTRONIC AND
OPTICAL PROPERTIES OF ALKALI METAL INTERCALATED TRANSITION METAL
DICHALCOGENIDES. THESIS ADVISOR : SIRICHOK JUNGTHAWAN, Ph.D. 109 PP.

Keyword : Layered structure/Intercalation

MoS$_2$ has a layered honeycomb structure with strong in-plane bonding and
weak out-of-plane vdW interactions, which enables the engineering of electronic
structures by intercalation. In this work, the effects of alkali metal intercalation on
MoS$_2$ are investigated by using first-principles calculations. The results show a
significant expansion of the interlayer spacing and contribution of electron donation
from alkali metal to the conduction band of MoS$_2$. The expansion obviously depends
on the atomic radii of the intercalated metals. Moreover, the bandgap type changes
from indirect to direct bandgap because of the reduction of electronic interactions
between adjacent layers. In-plane lattice parameters increase proportionally to the
concentration due to electrostatic repulsion. Other properties (such as structural
parameters, diffusion barriers, absorption coefficients, etc.) that can be compared
with experiments were calculated as well. Our results suggest that different atomic
radii and concentrations of intercalated alkali metals could provide an opportunity to
tune the electronic structures of TMDC materials and are promising in optoelectronic
devices.

School of Physics   Student's Signature_____

Academic Year 2021   Advisor's Signature _____

ACKNOWLEDGEMENTS

CONTENTS

CONTENTS (Continued)

LIST OF TABLES

LIST OF FIGURES

LIST OF FIGURES (Continued)

LIST OF FIGURES (Continued)

LIST OF ABBREVIATIONS

2D	=	Two-Dimensional
ARPES	=	Angle-Resolved Photoemission Spectroscopy
BSE	=	Bethe-Salpeter Equation
BZ	=	Brillouin Zone
CBM	=	Conduction Band Minimum
CDD	=	Charge Density Difference
CINEB	=	Climbing Image Modification
FETs	=	Field-Effect Transistors
GGA	=	Generalized Gradient Approximation
HF	=	Hatree-Fock
IPES	=	Inverse Photoemission Spectroscopy
LDA	=	Local Density Approximation
NEB	=	Nudged Elastic Band
PAW	=	Projector Augmented-Wave
PBE	=	Perdew, Burke, and Ernzerhof
PL	=	Photoluminescence
QY	=	Quantum Yield
Rel	=	Relative
TMDCs	=	Transition Metal Dichalcogenides
VASP	=	Vienna *ab initio* Simulation Package
VBM	=	Valence Band Maximum
vdW	=	van der Waals

CHAPTER I

INTRODUCTION

Throughout the past few decades, two-dimensional (2D) semiconductor materials such as graphene and thin layers of transition metal dichalcogenides (TMDCs) have attracted enormous attention due to their fascinating physical properties that arise from the quantum confinement associated with their ultrathin structure. These materials have shown promise as next-generation nanoelectronic, optoelectronic, spintronic and valleytonic devices. Several 2D materials exist in bulk form as stacks of bond layers with weak van der Waals (vdW) interlayer interactions, permitting exfoliation into 2D layers of atomically thin thickness (Novoselov *et al.*, 2005). There are many interesting layer-dependent properties in 2D materials that considerably differ from the properties in bulk form. The most interesting 2D material is graphene, which is a monolayer of graphite having a layered honeycomb structure (Novoselov *et al.*, 2004). Its electronic structure has a linear dispersion and charge carriers can be described as massless Dirac fermions (Geim and Novoselov, 2007). As a result, graphene has drawn numerous attention from experiments and theoretical works. Although graphene has unique electronic properties, pristine graphene is limited in its application due to its zero-bangap. For the mentioned reasons, it is clearly seen that we should find other 2D materials instead of graphene. However, the remarkable properties of graphene have inspired interest in TMDCs including MoS_2, $MoSe_2$, $MoTe_2$, WS_2, WSe_2 and WTe_2 which have honeycomb structures as well as graphene. In contrast, TMDC monolayers have sizeable bandgaps crossing from an indirect bandgap in bulk form to a direct bandgap in a single layer due to quantum confinement.

Electronic structures of bulk MoS_2 and WS_2 have been measured by angle-resolved photoemission spectroscopy (ARPES), as reported by Latzke *et al.* (Latzke *et al.*, 2015). In addition, they used first-principles calculations to investigate the electronic structures, which are in good agreement with their experiment. Since the

ARPES technique can measure only occupied states of electrons, it cannot probe conduction states. To investigate the conduction states of electronic structure, inverse photoemission spectroscopy (IPES) technique is needed. Komesu and Co-workers have demonstrated the electronic structure of Na doped MoS_2 (0001), whose valence and conduction band were measured from the ARPES and IPES technique, respectively. It was found that Na doped MoS_2 has an indirect bandgap of 1.46 ± 0.2 eV, which is in excellent agreement with their density functional theory (DFT) calculations (Komesu *et al.*, 2014). The influence of quantum confinement on the electronic structures of TMDCs has been investigated by Kuc *et al.* (Kuc *et al.*, 2011) and Yun *et al.* (Yun *et al.*, 2012). First-principles calculations have been carried out to investigate the trend of the electronic structures with a reduced number of layers. The results show the common features of the electronic structures of TMDCs. The electronic structures of TMDCs change from an indirect bandgap to a larger direct bandgap in single layer form. Moreover, molybdenum and tungsten based TMDCs are 2D semiconductors with a bandgap in visible light to near-infrared region (Wang *et al.*, 2015) allowing applications such as transistors and optoelectronic devices. The bulk form of MoS_2 , $MoSe_2$, WS_2, and WSe_2 are indirect bandgaps, whose measured values of bandgaps from photocurrent spectroscopy is 1.23 eV, 1.09 eV, 1.35 eV and 1.20 eV, respectively (Kam and Parkinson, 1982).

Many efforts have focused on studying the effects of strain in TMDCs (Desai *et al.*, 2014; Fan *et al.*, 2015; Chang *et al.*, 2013; Su *et al.*, 2014). Yun *et al.* have demonstrated the effects of strain on the electronic structure of single layer MoS_2 by using first-principles calculations. They found that the bandgap of monolayer MoS_2 changes from direct to indirect bandgap with a larger value under compressive strain. However, under tensile strain, the bandgap becomes an indirect bandgap with a reduced bandgap and finally becomes a metallic band with more than 11% of tensile stress (Yun *et al.*, 2012). DFT calculations of effects of the strain on electronic structures of bulk MoS_2 have been reported by Peelaers and Van de Walle. Under uniaxial tensile strain in the c direction, the bandgap of bulk MoS_2 changes to direct when the interlayer distance is increased by almost 50%. Moreover, strain also changes the effective mass of electrons and holes (Peelaers and Van de Walle, 2012).

ARPES of a quasi-freestanding monolayer of MoS_2 was investigated by Eknapakul and Co-workers in 2014 (Eknapakul *et al.*, 2014). The quasi-freestanding monolayer was established at the surface of bulk MoS_2 by intercalating potassium into the interlayer vdW gap. If the interlayer gaps of MoS_2 are sufficiently expanded by the intercalation, quasi-freestanding monolayers are created and the electronic structure changes to a direct gap. Xiong and Co-workers proposed a platform to tune the physical and chemical properties of nanoscale MoS_2. Li^+ ions were electrochemically intercalated into the MoS_2 interlayer spacing. They found significant enhancement of light transmission up to 90% and electrical conductivity in Li intercalated MoS_2 nanosheets. These enhancements in both optical transmission and electrical conductivity can be tunable through intercalation, which makes intercalation a potentially interesting technique for transparent electrode and touch screen applications (Xiong *et al.*, 2015). Intercalation in MoS_2 has reversibility during the ions-intercalation/deintercalation, which shows promise as an electrode for batteries (Li and Li, 2004; Cheng *et al.*, 2011). Lithium-ion batteries cannot meet the growing demand for energy storage at a low cost because of lithium's rarity (0.0017 weight %) in the Earth's crust. Sodium-ion batteries and potassium-ion batteries have attracted huge attention as a promising alternative to lithium-ion batteries due to their low cost and high abundance. However, the high standard reduction potential of sodium-ion batteries strongly limits their energy density of sodium-ion batteries. Potassium-ion batteries have a relatively high energy density because of their low standard reduction potential, which makes them suitable for some practical applications that require high energy density, especially electric vehicles. K^+ would enable replacing Li^+ to improve the rate capability and realize high mass loading electrodes without sacrificing specific capacity (Zhang *et al.*, 2019). Superior potassium-ion storage via vertical MoS_2 nano-rose with expanded interlayers on graphene has been demonstrated by Xie and Co-worker (Xie *et al.*, 2017), which indicates that layered metal dichalcogenides have great potential as electrode materials for high-performance potassium-ion batteries. Nevertheless, theoretical study on the electronic structures of intercalation of alkali metals in bulk MoS_2 and

other TMDCs still lacks because of the limitation of calculating electronic structure in a supercell.

Based on first-principles calculations, this research aims to study the structural, electronic, and optical properties of alkali metal intercalated TMDCs such as MoS_2. We will focus on the controllability of the electronic structures of TMDCs by intercalation with different alkali metals at various concentrations. Other properties (such as structural parameters, diffusion barrier, absorption coefficient, etc.) that can be compared with experiments will be calculated as well. We hope that this research will provide a deep understanding and useful knowledge for controlling the electronic structure of bulk TMDCs by intercalation.
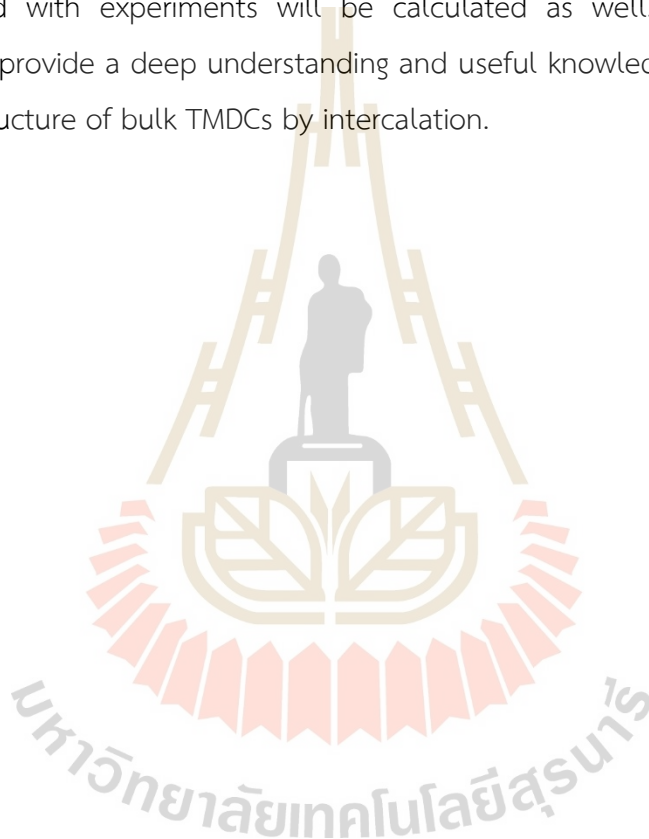
CHAPTER II

METHODOLOGY

This chapter will focus on the theoretical background for the simulation of materials. A wave function contains various types of material information, which can be obtained by solving the Schrödinger equation, for example, for the hydrogen-atom system. However, the equation is too complicated to solve when encountered with a many-electron problem. Hence, there are many approximations employed to simplify the many body problems into solvable ones. The DFT, which is the widely used method to simplify the many-electron Schrödinger equation, will be briefly explained. Approximations, methods and software used in this thesis will be introduced in this chapter.

2.1 Density Functional Theory

Recently, advanced computation systems and highly developed computational techniques have opened up an opportunity to study many physical properties of various materials. "First-principles calculations" or "*ab initio* calculations" (Brandt *et al.*, 2001; Kresse and Hafner, 1993) are theoretical calculations for studying the physical and chemical properties of condensed matter. These calculations start from basic concepts about condensed matter systems that are made of atoms and do not include any experimental parameters in the calculations. Therefore, the physics of condensed matter arises from the basic interactions of positively charged nuclei and negatively charged electrons.

2.1.1 Schrödinger Equation

The physics that describes the interactions of nuclei and electrons is relatively simple and is mostly governed by the Schrödinger equation (Schrödinger, 1926). The simplest example in the hydrogen-atom system can be written as follows:

$$\left[-\frac{\bar{h}^2}{2m}\nabla^2 - \frac{e^2}{4\pi\varepsilon_0 r_1}\right]\Psi(r_i) = E\Psi(r_i), \tag{2.1}$$

where $-\dfrac{\bar{h}^2}{2m}\nabla^2$ is the kinetic energy of the electron, $-\dfrac{e^2}{4\pi\varepsilon_0 r_1}$ potential due to the nucleus, r_i is the distant between single electron and a nucleus, $\Psi(r_i)$ is the electron wave function and E is the total energy of the electron. However, a problem arises in the practical calculations because many systems contain a very large number of atoms and an even larger number of electrons. Therefore, the interactions between electrons as well as electrons-nuclei are very complicated. The DFT is an approximation that the complication of many-body interactions between electrons is reduced by simplifying the exchange-correlation term in the potential (Kohn and Sham, 1965).

2.1.2 The Hohenberg and Kohn Theorem

Hohenberg and Kohn (Hohenberg and Kohn, 1964) proposed that the ground state energy and all properties of the electron wavefunction in the external potential $v_{ext}(\vec{r})$ can be determined from the electron density, $n(\vec{r})$. The ground-state energy of many electron wavefunctions is defined as

$$E[n(\vec{r})] = \int V_{ext}(\vec{r})n(\vec{r})d^3r + F[n(\vec{r})], \tag{2.2}$$

where $V_{ext}(\vec{r})$ is the external potential, which is generated by the interaction between nuclei and electrons, and $F[n(\vec{r})]$ is an unknown function, but it is a universal function of the electron density $n(\vec{r})$. It does not depend on the external potential and includes all kinetic energy and electron-electron interaction terms.

2.1.3 Kohn and Sham Equation

Based on Hohenberg and Kohn theorems, Kohn and Sham proposed that the universal functional $F[n(\vec{r})]$ in Equation 2.2 can be separated into three parts as,

$$F[n(\vec{r})] = V_H[n(\vec{r})] + T_s[n(\vec{r})] + E_{xc}[n(\vec{r})], \tag{2.3}$$

where $V_H[n(\vec{r})]$ is the electron-electron Coulomb energy can be defined as $V_H = \dfrac{e^2}{2}\iint \dfrac{n(\vec{r})n(\vec{r}')}{|\vec{r}-\vec{r}'|}d^3rd^3r'$, $T_s[n(\vec{r})]$ is the kinetic energy of the non-interacting system with the same density and it is not the exact kinetic energy function

$T\left[n(\vec{r})\right]$. The last term $E_{xc}\left[n(\vec{r})\right]$ is exchange-correlation energy which basically includes all the stuff, therefore the small different energy between $T_s\left[n(\vec{r})\right]$ and $T\left[n(\vec{r})\right]$ can be concluded in this term.

Therefore, the Kohn-Sham-effective potential can be written as (Kohn and Sham, 1965),

$$V_{eff}\left(\vec{r}\right) = V_{ext}\left(\vec{r}\right) + e^2 \int \frac{n(\vec{r}')}{\left|\vec{r} - \vec{r}'\right|} d^3 r' + \frac{\delta E_{xc}\left[n(\vec{r})\right]}{\delta n}. \tag{2.4}$$

Finally, Kohn-Sham equation involving a single electron is given by

$$\left[-\frac{\hbar^2}{2m}\nabla^2 + V_{eff}\left(r\right)\right]\psi_i\left(r\right) = \varepsilon_i \psi_i\left(r\right), \tag{2.5}$$

where $\psi_i\left(r\right)$ and ε_i are the single-electron Kohn-Sham orbitals and energies, respectively.

Only N (number of electrons) single-electron equations need to be solved self-consistently for non-interacting electrons in an effective potential due to the nuclei and the other N-1 electrons. An initial guess of electron density $n(r)$ is used to construct V_{eff}. Therefore, the wavefunctions ψ_i can be obtained by solving the Kohn-Sham equation. An improved $n(r)$ which can be given by

$$n(r) = \sum_{i-1}^{N}\left|\psi_i\left(r\right)\right|^2. \tag{2.6}$$

This loop can be repeated until reaching the convergence.

2.2   The Exchange Correlation Function

The $E_{xc}\left[n(\vec{r})\right]$ in Equation 2.4 includes all the stuff, so it cannot be known exactly. The most commonly used approximations are based on DFT with the local density approximation (LDA) or generalized gradient approximation (Grimme). LDA is the assumption that the electron density can be treated locally as a uniform electron gas, as proposed by Kohn and Sham in 1965. It is suitable for systems whose charge density does not change rapidly. However, it usually fails to describe weak atomic bonds. Therefore, GGA is used to improve the LDA. $E_{xc}\left[n(\vec{r})\right]$ is expanded as a function of the electron densities and their gradients, $\left|\nabla n(\vec{r})\right|$ (Kohn, 1999). The $E_{xc}^{GGA}\left[n(\vec{r})\right]$ can be written as,

$$E_{xc}^{GGA}\left[n(\bar{r})\right]=\int f\left[n(\bar{r}),\nabla n(\bar{r})\right]n(\bar{r})d^3r \tag{2.7}$$

GGA reduces the errors in blinding energy of weak atomic bonds. It can improve ground state properties. GGA usually underestimates the bandgap of solids, while LDA overestimates. Alternatively, hybrid functionals are constructed by mixing exact exchange energy from Hatree-Fock (HF) with exchange and correlation from other functionals (Becke, 1993). Generally, the hybrid functionals provide better accuracy for bandgap and total energy, but the methods are more computationally intensive than LDA or GGA (Hafner, 2008).

In some cases, LDA and GGA fail to describe the structural properties of materials, especially in layered materials, due to long-range electron correlations, where vdW interactions between atoms and molecules play an important role. For the long-range electron correlations, the asymptotic tail of the energy approaches zero exponentially in standard LDA and GGA. Hence, the vdW correction to GGA has been proposed by Grimme, which introduces dispersion force field parameters to the conventional DFT, so called the DFT-D2 method (Grimme, 2006). The general form of DFT energy with vdW correction can be written as

$$E_{DFT+D2}=E_{DFT}-E_{disp} . \tag{2.8}$$

The E_{disp} is the correction term which take the form as following

$$E_{disp}=-\frac{1}{2}\sum_{i=1}^{N_{at}}\sum_{j-1}^{N_{at}}\sum_{L}\frac{C_{6ij}}{r_{ij,L}^6}f_{d,6}(r_{ij,L}), \tag{2.9}$$

where the summations are over all N_{at} and all translations of the unit cell $L=(l_1,l_2,l_3)$, $i\neq j$ for reference cell $L=0$, C_{6ij} is dispersion coefficient for the atom pair ij, $r_{ij,L}$ is interatomic distance and the term $f(r_{ij})$ is a damping function, which is given by

$$f_{d,6}(r_{i,j})=\frac{s_6}{1+e^{-d(r_{ij}/(s_R R_{0ij})-1)}} , \tag{2.10}$$

where s_6 is the global scaling parameter which has been optimized to 0.75 for PBE, the parameter s_R is equal to 1 and $d=20$. The combination rules which are used to compute the parameters C_{6ij} and R_{0ij} are defined as

$$C_{6ij}=\sqrt{C_{6ii}C_{6jj}} \quad \text{and} \quad R_{0ij}=R_{0i}+R_{0j}. \tag{2.11}$$

The values of C_{6ij} and R_{0ij} are tabulated for each element by Grimme (Grimme, 2006; Bucko et al., 2010; Kerber et al., 2008).

2.3   Unfolding of an Electronic Structure

The electronic structures are calculated along the high symmetry points in the first BZ. However, the Bloch theorem (Bloch, 1929), which is used in DFT calculations, builds upon the translational symmetry of the periodic crystal systems. A problem arises in the practical use of DFT calculations whenever we encounter systems whose original translational symmetry is broken. Therefore, we must employ large supercells whose size determines the periodicity of the band structure through the Bloch theorem. This results in a smaller Brillion zone compared with the Brillion zone of the primitive cell and a folded band structure consisting of primitive bands and folded bands. The folded band structure is very complicated and difficult to compare to the results of the ARPES technique, which is a direct measurement of band structures. The problem can be alleviated by unfolding the folded electronic structure through induced representations of space groups, as reported by Tomić and Co-workers (Tomić et $al.$, 2014). Assume that localized electronic states are given by $|0,\mu\rangle$ centered at position s_μ of unit cell located at origin and the folded band structure is given in the Bloch basis $|k,\mu\rangle = \dfrac{1}{\sqrt{N}}\sum_n \exp(ik \cdot R_n)|R_n,\mu\rangle$ where R_n is position vectors of unit cells in crystal lattice, N is a number of unit cell and μ is localized electronic state at wave vector k in Brillion zone. To unfold the folded band structure, matrix elements for the projector operator $\hat{P}_{k\alpha}$ need to be calculated. The matrix elements are given by

$$[\hat{P}_{k\alpha}]_{\gamma\delta} = \langle k,\gamma|\hat{P}_{k\alpha}|k,\delta\rangle = \frac{1}{K}\sum_i \exp(\frac{2\pi i\alpha f_i^\alpha}{K})\exp(ik \cdot \tau_i)W_{\gamma\delta}(\hat{C}_i) \qquad (2.12)$$

where α is irreducible representation index, i is lattice vector index, K is reciprocal lattice vector, f_i^α is an integer such that $0 \le f_i^\alpha < K$, τ is fractional translation and $W_{\gamma\delta}(\hat{C}_i)$ is their matrix element which can be written as $W_{\gamma\delta}(\hat{C}_i) = r_{\gamma\delta}\delta(s_\delta - \hat{C}_i s_\gamma)$ where δ is Kronecker delta and sites s_δ and $\hat{C}_i s_\gamma$ are equal if they differ by a lattice vector. In this research, band structures $|k,n\rangle$ where n is the band index will be obtained by using VASP. The folded band can be unfolded by applying the projectors to the column vector containing the projections of bands onto the localized states $w_{k,n}^\mu = \langle 0,\mu|k,n\rangle$. The exponential factors $\exp(-ik \cdot s_\mu)$ can be omitted because they are already included in the projections $w_{k,n}^\mu = \langle 0,\mu|k,n\rangle$ within

the VASP package. Figure 2.1 indicates the unfolding method of $2\times2\times1$ supercell of MoS$_2$. The BZ of the supercell is smaller than the BZ of primitive cell because the reciprocal lattice vector a is reduced to ½ where divisor corresponds to the multiplier of the supercell. To achieve unfolding, the reduction of reciprocal lattice vector needs to be recovered by multiplying the calculated path ($\Gamma K'$) of k-point with the multiplier, which is 2 in this case. The information about primitive bands is now recovered, as shown in Figure 2.1(f). However, the folded bands remain, which makes it very complicated as an example of a folded band structure in Figure 2.2(a). The problem can be alleviated by reducing the weight of the folded band through a Python script, so-called vasp_unfold developed by Milan Tomić based on his approach mentioned before. The script can be downloaded by using the following link: https://github.com/tomkeus/vasp_unfold. After removing the folded bands, the result of the unfolded band structure is exhibited in Figure 2.2(b). The unfolding method gives us an opportunity to study the electronic structures of real materials, which are not perfect, allowing one to compare the unfolded band structure with the experimental results from the ARPES technique, *etc*.

Moreover, a Python script was written for plotting the unfolded band with orbital-projected. The orbital-projected wavefunctions are obtained by decomposing the confined wavefunction into the $l = 0$, 1 and 2 spherical harmonics. The script will be described in the appendices section.
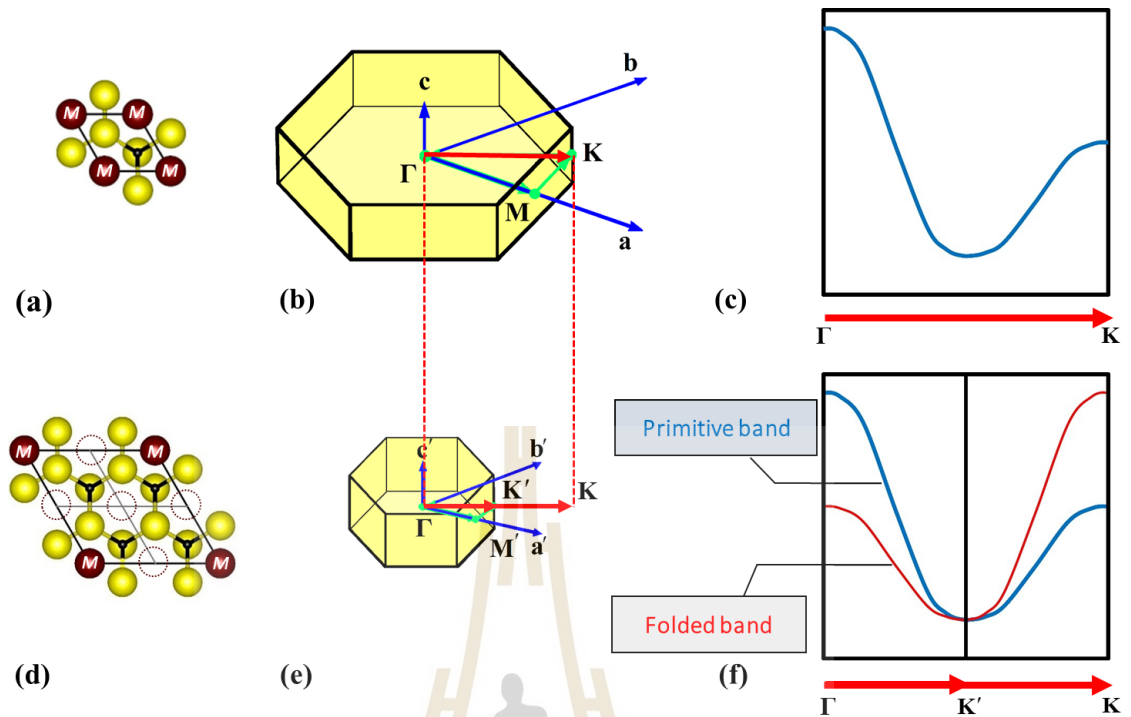
Figure 2.1   Unfolding method. (a, d) Crystal structures of MoS$_2$ in primitive cell and $2 \times 2 \times 1$ supercells. (b, c) The BZ of the primitive cell and supercell. (c) Schematic electronic structure of the primitive cell. (d) The schematic electronic structure of the folded band.
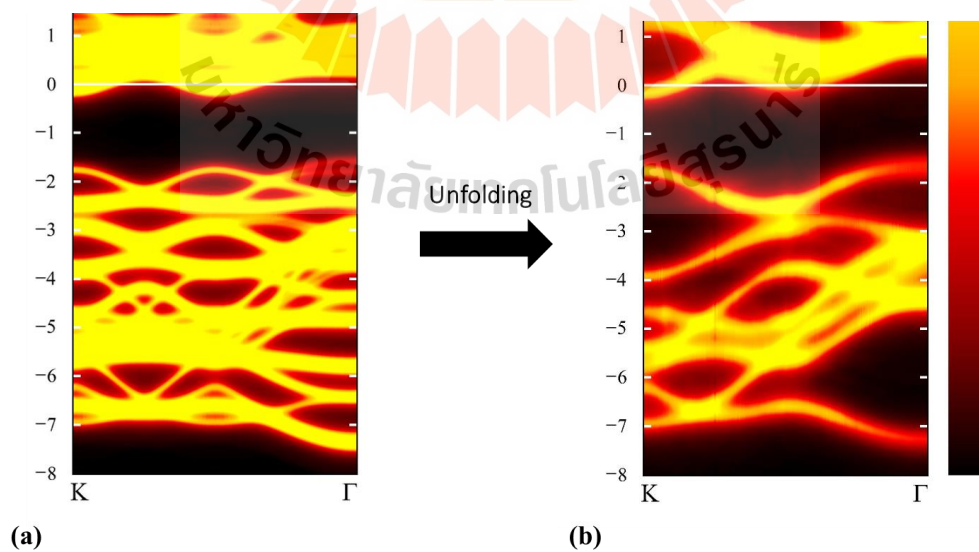
Figure 2.2   Comparison between (a) folded band structure and (b) unfolded band structure.

2.4   Nudged Elastic Band

The diffusion barrier is important because it indicates how easy it is to move an intercalated or an adsorbed atom from an initial state to a final state. The nudged elastic band method (NEB) (Mills *et al.*, 1995; Jónsson *et al.*, 1998) was introduced to find saddle points and minimum paths between known reactants and products by optimizing a number of intermediate images along a reaction path. Equidistant images are created by using geometries interpolated between the initial and final states. The optimization is constrained by adding a tangential spring force to keep the image equidistant during relaxation. The effective forces F_i^{NEB} can be written as,

$$F_i^{NEB} = F_i^{S\parallel} + F_i^{\perp}$$
(2.13)

where, $F_i^{S\parallel}$ is a parallel spring force and $F_i^{\perp}$ is the real force acting on each atom, ignoring the component that minimizes energy parallel to the path. The parallel spring force is given by

$$F_i^{S\parallel} = k\left(\left|R_{i+1} - R_i\right| - \left|R_i - R_{i-1}\right|\hat{\tau}_i\right)$$
(2.14)

where, $\hat{\tau}_i$ is unit vector of local tangent.

However, NEB does not guarantee reaching the transition state where the energy barrier is at the saddle point. The transition state can be found by using climbing image modification (CINEB) to improve NEB. In this method, the forces of the highest energy image along the band are modified by removing the spring force and inverting parallel forces along the band to push the maxima uphill as following,

$$F_{i,\max}^{NEB} = F_i - 2F_i \cdot \hat{\tau}_i\hat{\tau}_i .$$
(2.15)

CINEB allows us to find transition states and minimum paths between known reactants and products, which is important information to describe the diffusion of an atom in a material.

2.5   Optical Calculations

The optical properties of materials, such as transmission, reflection and absorption, can be quantified by a number of parameters. The parameters can be determined by optical processes of materials at a microscopic or quantum mechanical level. At the quantum mechanical level, complex dielectric function is closely connected with the band structure. The imaginary part of the frequency

dependent dielectric $\varepsilon_{\alpha\beta}^{(2)}(\omega)$ is determined by a summation over empty states as in the following equation,

$$\varepsilon_{\alpha\beta}^{(2)}(\omega) = \frac{4\pi^2 e^2}{\Omega} \lim_{q \to 0} \frac{1}{q^2} \sum_{c,v,k} 2w_k \delta(\varepsilon_{ck} - \varepsilon_{vk} - \omega) \times \langle u_{ck+\varepsilon_\alpha q} | u_{vk} \rangle \langle u_{ck+\varepsilon_\alpha q} | u_{vk} \rangle^* \quad (2.16)$$

where, c and v are referred to conduction and valence band states, respectively, and u_{ck} is the cell periodic part of the orbital at the k-point k. The transition is made from occupied to unoccupied states within the first BZ. The real parts of the dielectric tensor $\varepsilon_{\alpha\beta}^{(1)}(\omega)$ can be determined by using the Kramers-Kroning relation as follows:

$$\varepsilon_{\alpha\beta}^{(1)}(\omega) = 1 + \frac{2}{\Pi} P \int_0^\infty \frac{\varepsilon_{\alpha\beta}^{(2)}(\omega')\omega'}{\omega'^2 - \omega^2 + i\eta} d\omega' \quad (2.17)$$

The frequency dependent dielectric can be used to find reflectivity $R(\omega)$,

Since the optical transition operator between two states is proportional to the momentum ($-i\hbar\nabla$) operator, the transition from the valence state ψ_v to the conduction state ψ_c is obtained from $\langle \psi_c | \nabla | \psi_v \rangle$ (Gajdoš et al., 2006). The quantity of $|\langle \psi_c | \nabla | \psi_v \rangle|^2$ is calculated where ψ_c and ψ_v are restricted to the conduction band minimum (CBM) state and the valence band states at Γ, respectively. The quantity indicates the transition strength and can be used to determine which band is the optical bandgap in the electronic structures to compare with the optical bandgap from experiments. This method has been proven to be useful to identify an optical bandgap where the transition between the valence band maximum (VBM) and the CBM is forbidden (Jiamprasertboon et al., 2017).

2.6 The Vienna *Ab initio* Simulation Package (VASP)

In this research, the first principles calculations will be performed by employing the projector augmented-wave method (Siriroj et al.) (Blöchl, 1994; Kresse and Joubert, 1999; Kresse and Furthmüller, 1996) as implemented in the Vienna *ab initio* simulation package (VASP) developed by Kresse, Hafner and Furthmüller (Kresse and Hafner, 1993; Kresse and Furthmüller, 1996). Based on DFT, the GGA functionals will be used with the parameterization of the Perdew, Burke, and Ernzerhof (PBE) (Perdew et al., 1996) exchange-correlation function. The vdW interactions are

corrected by using the DFT-D2 approach of Grimme (Grimme, 2006; Bucko *et al.*, 2010), which has been effectively used for layered structures such as graphene and layered TMDC materials. VASP uses a self-consistent scheme to optimize wavefunctions, as shown in the flowchart in Figure 2.3. The self-consistency begins with the trial charge density and trial wavefunctions. The input charge density and wavefunctions are independent quantities. Within each self-consistent loop, the charge density is used to set up the Hamiltonian, and then the wavefunctions are optimized iteratively so that they get closer to the exact wavefunctions of this Hamiltonian. From the optimized wavefunctions, a new charge density is calculated, which is then mixed with the old input-charge density. If the change of energy ΔE is less than the required accuracy or tolerance, the iteration is done and the minimized energy, force, equilibrium volume, *etc*. will be obtained.
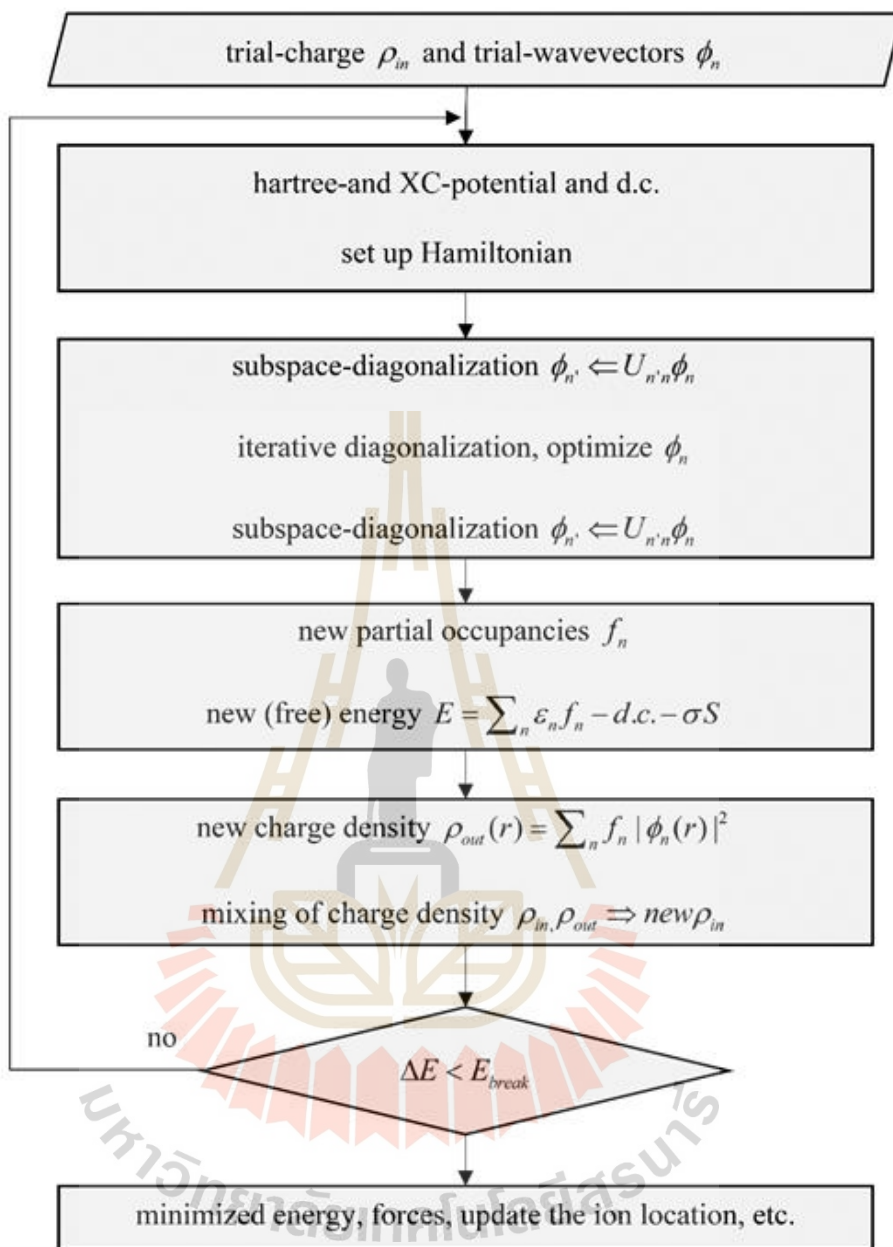
Figure 2.3   The self-consistent scheme used in the VASP codes.

CHAPTER III

BULK, MONOLAYER AND ALKALI METAL INTERCALATED MoS$_2$

In this chapter, properties of bulk, monolayer and alkali metal intercalated MoS$_2$, such as crystal structures and electronic structures, will be described.

3.1   Crystal Structure of MoS$_2$

Molybdenum disulfide (MoS$_2$) is one of the members of the TMDC family, which is commonly used as a dry lubricant. It is a promising low-cost material for commercial fabrication of nanoelectronic and optoelectronic devices. Pristine bulk MoS$_2$ and other TMDCs have a honeycomb structure of strongly boned layers with weak vdW interaction between layers, as shown in Figure 3.1(a). The weak interlayer attraction allows exfoliation into a monolayer (see Figure 3.1(b)) (Mak *et al.*, 2010). MoS$_2$ monolayer is a flexible material and one of the strongest semiconductor materials. MoS$_2$ monolayer is 30 times stronger than steel and can be deformed up to 11% before breaking (Bertolazzi *et al.*, 2011). Ultrathin layers of MoS$_2$ have been attracted as a channel material in field-effect transistors (FETs) due to its interesting features including the stability of the structure, the lack of dangling bonds and high mobility (Fivaz and Mooser, 1967).

The optimized structures of pristine bulk and monolayer MoS$_2$ were calculated by using the PAW method as implemented in the VASP package based on DFT. The GGA functional was used with the parameterization of PBE as an exchange-correlation function. The vdW interaction was included using the D2 approach of Grimme. The cutoff energy of the plane wave expansion is 500 eV. The Γ-centered Monkhorst-Pack with $24 \times 24 \times 5$ k-mesh was used for Brillouin zone (BZ) integration. The unit cell of bulk MoS$_2$ is composed of AB stacks of X-M-X layers, so-called 2H-MoS$_2$, where the chalcogen atoms (X) are in two hexagonal planes separated by a plane of metal atoms (M). The stacking is the net result of the attractive Coulomb

interactions of M-X atoms and the repulsive Coulomb interactions between X atoms in adjacent layers. The lattice vectors can be written as

$$\vec{a}_1 = \frac{a}{2}\left(\hat{x} + \sqrt{3}\hat{y}\right), \qquad \vec{a}_2 = \frac{a}{2}\left(\hat{x} - \sqrt{3}\hat{y}\right), \qquad \vec{a}_3 = c\hat{z}, \qquad (3.1)$$

where a and c are lattice parameters. The hexagonal reciprocal lattice in the Figure 3.1(c) can be built up from reciprocal lattice vectors as following,

$$\vec{b}_1 = \frac{2\pi}{a}\left(\hat{x} + \sqrt{3}\hat{y}\right), \qquad \vec{b}_2 = \frac{2\pi}{a}\left(\hat{x} - \sqrt{3}\hat{y}\right), \qquad \vec{b}_3 = \frac{2\pi}{c}\hat{z}. \qquad (3.2)$$

The high symmetry points of the hexagonal reciprocal lattice that have been used in this calculation are listed in Table 3.1.

The optimized lattice parameters a and c of pristine bulk MoS$_2$ are 3.189 Å and 12.426 Å. They are slightly larger than the experimental results (3.160 Å and 12.294 Å, respectively) (Bronsema $et\ al.$, 1986). The tiny overestimate of the lattice parameter is usually found in PBE. A unit cell of a monolayer was constructed by fixing the lattice parameter c at 20 $\overset{\circ}{A}$, which creates a vacuum space to separate periodic layers. The optimized lattice parameter a of the monolayer is equal to the value of pristine bulk and atomic positions have no change. This indicates the stability of the isolated layer structure.

Table 3.1   High symmetry points of the reciprocal lattice and their coordinates in unit of $\frac{2\pi}{a}$.

High symmetry points	b_1	b_2	b_3
Γ	0	0	0
M	1	0	0
K	0.667	0.667	0
Σ	0.333	0.333	0

3.2   Electronic Structure of MoS$_2$

The electronic structure of MoS$_2$ and other TMDCs has a similar feature of crossing over from indirect bandgap in bulk form to direct bandgap in monolayer form. Optical spectroscopy of N-monolayers of MoS$_2$ (N = 1, 2, 3;...;6) has been demonstrated by Mak *et al.* (Mak *et al.*, 2010). From photoluminescence (PL), it was found that the bandgap increases with a reduced number of layers. At the limit of a single layer, the bandgap becomes a direct bandgap of 1.8 eV. PL quantum yield (QY) of monolayer MoS$_2$ shows more than 10^4-fold enhancement compared to PL QY of bulk MoS$_2$. Although the PL QY of monolayer MoS$_2$ has shown a dramatic enhancement, it is still lower than the expected theoretical value because of considerable defect density (Mak *et al.*, 2010; Yuan and Huang, 2015). The monolayer of TMDCs has strong spin-orbit coupling, making them a potential candidate for application in spintronic devices. The strong spin-orbit coupling is a result of the lack of inversion symmetry, quantum confinement, and *d* electrons in the TMDC materials (Zhu *et al.*, 2011).
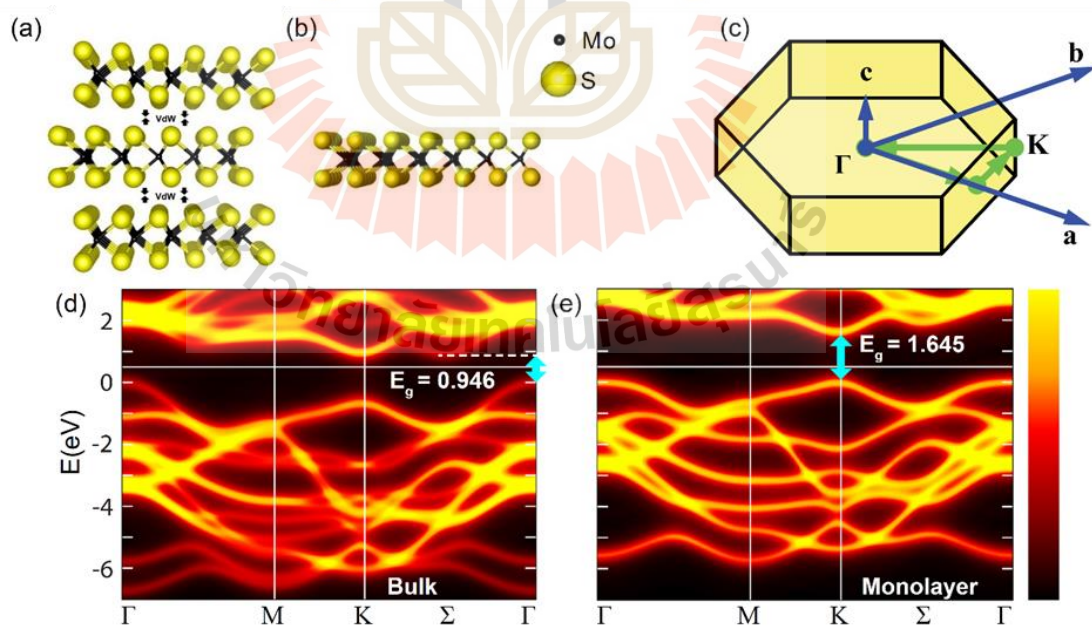
Figure 3.1   Crystal structures and electronic structures of MoS$_2$. (a, b) Crystal structures of bulk and monolayer. (c) BZ of hexagonal unit cell. Electronic structures of (d) pristine bulk MoS$_2$ and (e) monolayer MoS$_2$ along high symmetry $\Gamma - M - K - \Sigma - \Gamma$.

The electronic structures of pristine bulk and monolayer MoS_2 were calculated along high symmetry $\Gamma-M-K-\Sigma-\Gamma$ in the first Brillouin zone. Bulk MoS_2 has an indirect bandgap of 0.939 eV (Figure 3.1(d)), where VBM and CBM are located at K point and Σ point, respectively. The bandgap is an underestimated value compared to 1.23 eV from photocurrent spectroscopy by Kam and Parkinson (Kam and Parkinson, 1982). The calculated bandgap is lower than the experimental results due to an underestimation of the bandgap by the approximation of the many-body interactions. However, the bandgap of monolayer MoS_2 changes to direct bandgap of 1.645 eV at K point, as shown in Figure 3.1(e) due to quantum confinement. This is in good agreement with the photoluminescence measurement of 1.88 eV by Mak *et al.* (Mak *et al.*, 2010). Molybdenum and tungsten-based TMDCs are 2D semiconductors with bandgaps ranging from visible light to the near-infrared region, allowing applications such as transistors and optoelectronic devices (Wang *et al.*, 2015).

3.3   Influence of Quantum Confinement on the Electronic Structures of MoS$_2$

The crossover from indirect to direct bandgap in monolayer MoS_2 is the result of quantum confinement and changes in hybridization between p_z orbitals on S atoms and d orbitals on Mo atoms (Kuc *et al.*, 2011; Splendiani *et al.*, 2010). To study the influence of quantum confinement on the electronic structure of MoS_2, tensile strain was applied to pristine bulk MoS_2 by extending the lattice parameter c. Since each layer of bulk MoS_2 is barely changed after applying the strain, the interlayer gap increases with the lattice parameter c proportionally. The wider interlayer gap enables us to investigate the impact of layer coupling on electronic structure. Theoretically, the energy spitting decreases with decreasing interaction strength, as shown in the schematic in Figure 3.2.
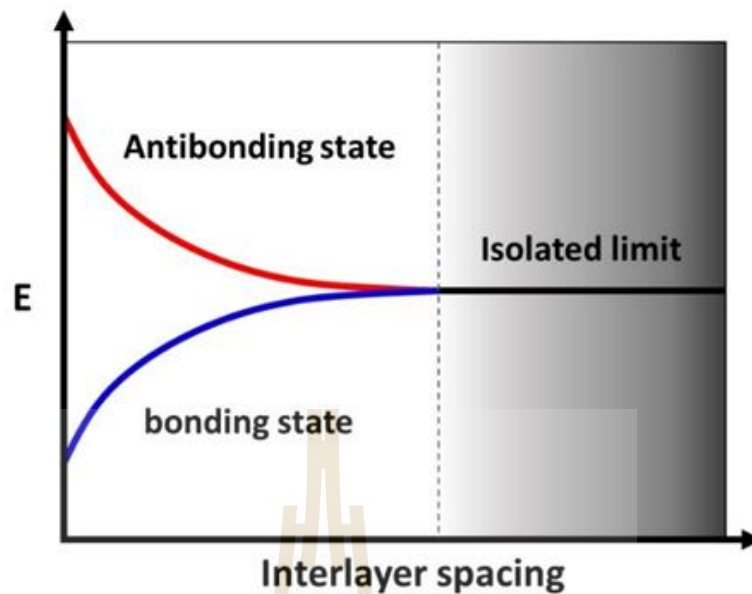
Figure 3.2 Schematic of the reduction in energy splitting due to the increased interlayer spacing.

Bulk MoS_2 was optimized while the extended lattice parameter c was fixed for each different value, such as $1.2c_0$ and $1.4c_0$, where c_0 is the value of pristine bulk. Electronic structures were calculated with orbital-projected along high symmetry $K - \Sigma - \Gamma$. Spin-orbit interactions were neglected in this calculation. The results indicate that the increasing of lattice parameter c weakens the interaction between layers. Therefore, the characteristics of MoS_2 electronic structures with extended lattice parameter c change similarly to the electronic structure of monolayer MoS_2 as shown in Figure 3.3. The black arrows in Figure 3.3(a) denote indirect bandgap between VBM at Γ point and CBM at K point $\left(E_g\left(K_c - \Gamma_v\right)\right)$, indirect bandgap between VBM at Γ point and CBM at Σ point $\left(E_g\left(\Sigma_c - \Gamma_v\right)\right)$ and direct bandgap between VBM at K point and CBM at K point $\left(E_g\left(K_c - K_v\right)\right)$ that have been tracked while increasing the lattice parameter c. The relationship between the tracked bandgaps of MoS_2 and lattice parameter c in Figure 3.3(e) indicates that the direct bandgap $E_g\left(K_c - \Gamma_v\right)$ increases rapidly and then converges to the bandgap of the monolayer (dash line in the Figure 3.3(e)), leading to the crossing over to the direct bandgap. This is the result of the exponential decreasing of energy splitting shown as red arrow in Figure 3.3(a), especially the splitting of d_z^2
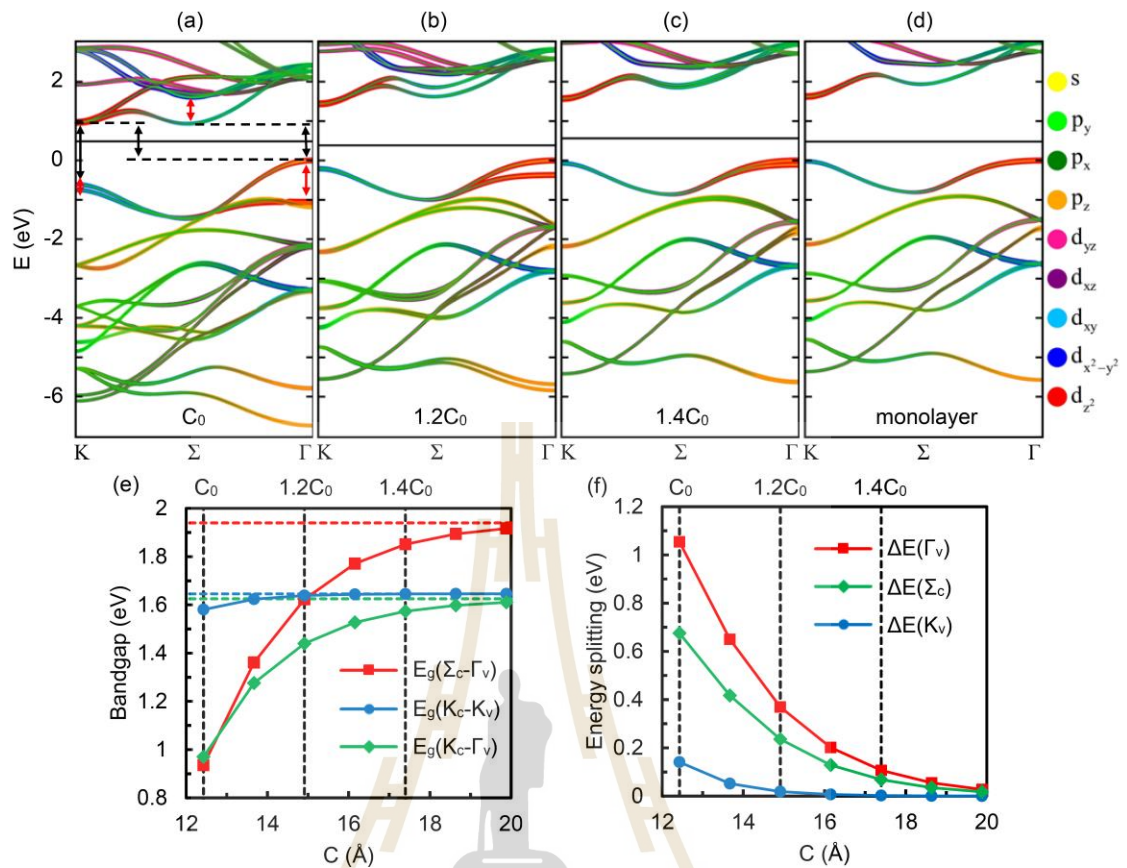
Figure 3.3 Electronic structures of MoS$_2$ with different lattice parameter c including the value of (a) c_0, (b) $1.2c_0$ and (c) $1.4c_0$. (d) Electronic structure of monolayer MoS$_2$ where orbital-projected are shown in different colors for each orbital. (e) Relationship between bandgaps of MoS$_2$ and the lattice parameter c where dashed lines denote the bandgap of monolayer MoS$_2$. (f) Energy spitting reduction upon increasing of the lattice parameter c.

orbital of Mo atom at Γ point. These results give us an opportunity to tune the size and type of electronic structure of MoS$_2$ and other TMDCs by controlling the gap between layers, such as by intercalating alkali metals into the interlayer gap.

3.4   Alkali Metal Intercalated MoS$_2$

The intercalation of alkali metal on bulk MoS$_2$ has two significant effects, including the expansion of the interlayer spacing and the contribution of electrons. The $2\times2\times1$ supercell was used to simulate alkali metal intercalated MoS$_2$ with various concentrations ($\mathbf{MoS_2}A_x$, where A is alkali metal and x is concentration). The intercalated alkali metals have an energetically favorable position at the center of the hexagonal interstitial site (Hex-site), as indicated by the brown atom or dashed circle in Figure 3.4(b). The intercalations expand the interlayer vdW gap of MoS$_2$ bulk while layer thickness barely changes. Therefore, the lattice parameter c was considerably increased due to the expansion. The blue line in Figure 3.5(i) shows that at the same concentration but with different intercalated alkali metal atomic sizes, the lattice parameter c increases. However, the increasing of the lattice parameter a is irrelevant to the atomic size. The higher the concentration, the more the lattice parameter a increases (see red line in Figure 3.5(i)) because of charge repulsion from the donated electron. We note that the concentration above $x=0.25$ introduces a phase transition, leading to a mixed state between semiconducting 2H and metallic 1T.
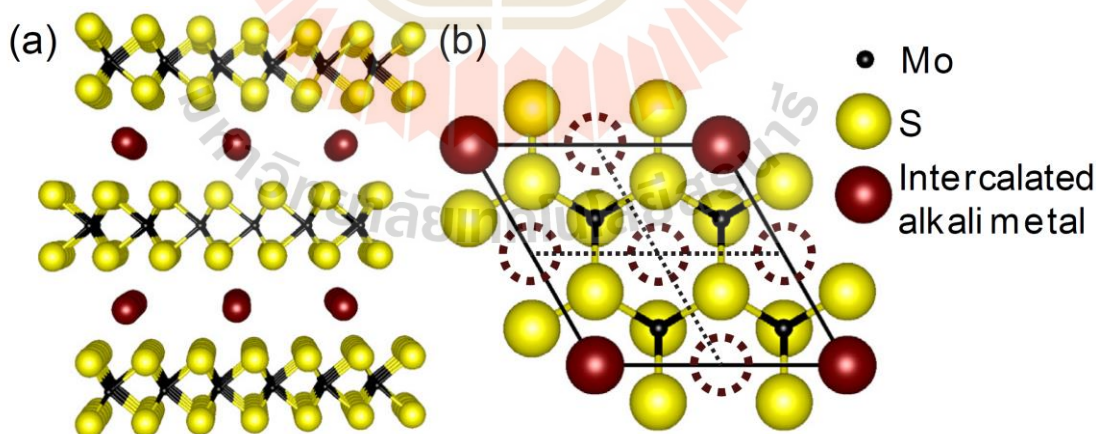
Figure 3.4   Alkali metal intercalated MoS$_2$ with a concentration of $x=0.25$ in the (a) cross-section and (b) top views, where dashed circles indicate other positions of the Hex-site.

3.5   Electronic Structure of Alkali Metal Intercalated MoS$_2$

Since DFT builds upon the translational symmetry of the periodic crystal systems through the Bloch theorem. The electronic structures of $2 \times 2 \times 1$ supercell calculations are folded band structures, which cannot be compared to the experiment. The unfolding method proposed by Tomić and Co-workers (Tomić *et al.*, 2014) was used to alleviate the problem. The results showed that both bandgap size and type are tunable through intercalation. The electronic structures of Li and Na intercalation have an indirect bandgap of 1.011 eV and 1.241 eV, respectively, which are similar to pristine bulk but with a larger bandgap. The same feature of crossing over from indirect to direct bangap that has been found in monolayer occurs in K and Rb intercalation. Since K and Rb intercalation greatly increase the lattice parameter c, the interaction between layers is greatly reduced, reaching an isolated condition as described in Section 3.3. The bandgaps of K and Rb intercalation changed to the direct bandgaps of 1.598 eV and 1.600 eV, respectively, located at K point (see Figures 3.5(c) and 3.5(d)). These are very close to the direct bandgap of monolayer MoS$_2$ of 1.645 eV from our calculation as well as 1.86 eV from Eknapakul *et al.'s* ARPES measurement of a quasi-freestanding monolayer of K intercalated in MoS$_2$ (Eknapakul *et al.*, 2014). Alkali metals contribute electrons to the layer of MoS$_2$, and Fermi levels thus increase. Hence, enhancement of electrical conductivity can be tunable. Moreover, the metallic band structure (the Fermi level lies in an incompletely filled band) decreases the probability of light absorption, which enhances the optical transmission of MoS$_2$ even further (Xiong *et al.*, 2015). The tunable bandgap, the enchantment in conductivity and the improved transparency of MoS$_2$ through intercalation have shown promise for optoelectronic, electronic and touch screen devices.
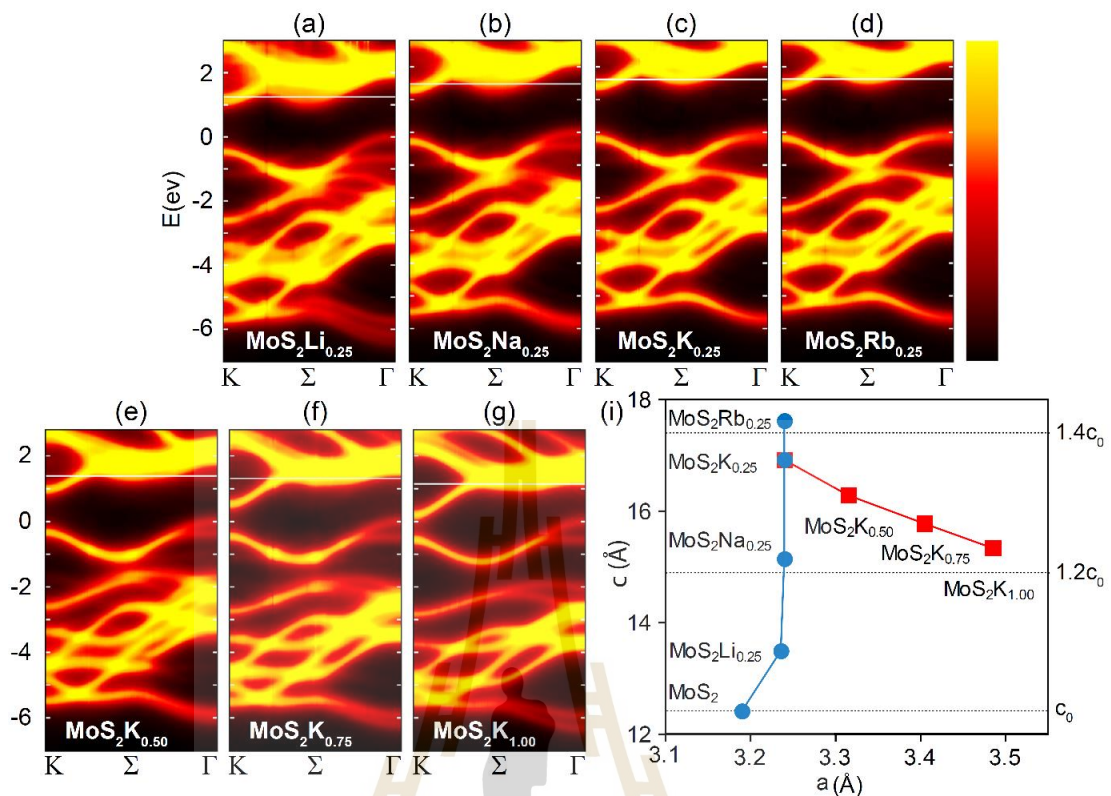
Figure 3.5 Unfolded electronic structures of alkali metal intercalated TMDCs, including (a) $MoS_2Li_{0.25}$, (b) $MoS_2Na_{0.25}$, (c) $MoS_2K_{0.25}$, (d) $MoS_2Rb_{0.25}$, (e) $MoS_2K_{0.50}$, (f) $MoS_2K_{0.75}$ and (g) $MoS_2K_{1.00}$. The white horizontal lines denote Fermi energy. (i) Graph of lattice parameter a versus c of pristine MoS_2 and alkali metal intercalated MoS_2, the blue line exhibits the result of different alkali metals M and the red line indicates the result of varying concentrations x.

3.6   Effect of Increasing the Lattice Parameter a and Contribution of Electrons to Electronic Structure

The enhancement of electrical conductivity can be tuned depending on electron contribution. To investigate the effect of electron contribution to electronic structure, different values of electrons (such as 0.5, 1.0, 1.5 and 2.0 (e/unit cell) corresponding to x = 0.25, 0.50 and 0.75, respectively) were added to the unit cell of bulk MoS_2 while the lattice parameter c was fixed at c_0. This allows us to observe the increase of the lattice parameter a in terms of electron contribution due to charge repulsion. The results indicate that the lattice parameter a increases linearly with the electron contribution, causing the angle of S-Mo-S (θ_{S-Mo-S}) to decrease, as

shown in Figure 3.6(e). The θ_{S-Mo-S} controls the strength of the coupling of the d orbital from the Mo-S bond. With the decreasing of θ_{S-Mo-S}, a pair of bonding and antibonding states with major $4d_z^2$ (out-of-plane orbital) is weakened (see the red line in Figure 3.6(e)), causing the energy change of the state at K_c and Γ_v. Bandgap becomes more metallic with electron contribution because of the rapidly decreasing energy of the state at K_c and the increasing energy of the state at Γ_v. However, a pair of bonding and antibonding states with major $4d_{xy}$ (in-plane orbital) was strengthened with the decrease of θ_{S-Mo-S}. We noted that the weakened coupling of out-of-plane orbital results in the metallic band structure of MoS_2.
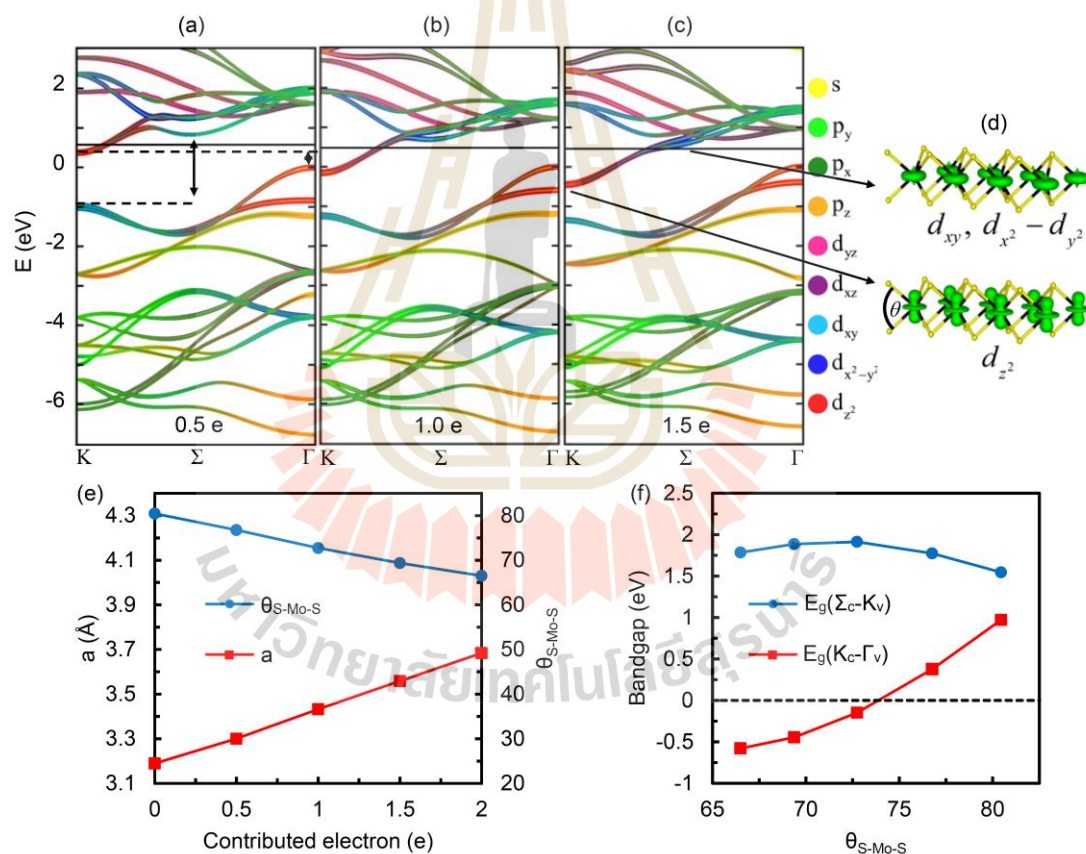
Figure 3.6 Electronic structures of MoS_2 with added (a) 0.5, (b) 1.0 and (c) 1.5 electrons/unit cell where the lattice parameter c is fixed at c_0. (d) Isosurfaces of band with band-decomposed charge density at Σ_c and K_c dominated by the major $4d_{xy}$ and $4d_z^2$ orbitals, respectively. (e) Contributed electron *vs.* lattice parameter a and θ_{S-Mo-S}. (f) Energy splinting of a pair of bonding and antibonding states with major $4d_{xy}$ (red line) and $4d_z^2$ (blue line) characters.

CHAPTER IV

ELECTRONIC AND OPTICAL PROPERTIES OF ALKALI METAL

INTERCALATED MoS$_2$

From the previous chapter, the changing of the electronic structures of MoS$_2$ through intercalation indicates that intercalation is a good technique to improve the electronic and optical properties of MoS$_2$ and the TMDC family. In this chapter, the electronic and optical properties of alkali metal intercalated MoS$_2$ will be discussed.

4.1 Alkali Metal Diffusion

The large interlayer distance and the weak van der Waals interaction between layers in MoS$_2$ make it an ideal host for reversible and fast alkali metal insertion/extraction in principle. In this section, the diffusion of alkali metal in MoS$_2$ was investigated by using the NEB method with CINEB improvement to study how easy it is to move an intercalated alkali metal to the next energetically favorable position. This method was introduced to find the minimum path between reactants and products, where the diffusion barrier can be found at the saddle point where its relative (Rel.) energy is at its maximum. In this study, a $2 \times 2 \times 1$ supercell of MoS$_2$ was used, where 11 images were created by using geometries interpolated between the initial and final states. The spring force used to keep the image equidistant during relaxation is the adjusted parameter to make the NEB calculation converge. The diffusion of alkali metal from Hex-site (A point) to another Hex-site (C point) was investigated along 2 paths, including the first path that alkali metal diffuses directly from A point to C point (AC path) and the second path that alkali metal diffuses from A point to B point located at the top of the Mo atom (Mo-top) and then diffuses to C point (ABC path), as shown in Figure 4.1. The results show that the Li atom moves toward the Mo atom at the B point when diffuses along an ABC path. However, this offset does not occur when the Li atoms diffuse along an AC path. The offset was

also found in Na, K and Rb diffusion along the ABC path, which results in a lower diffusion barrier compared to that of the AC path, as indicated by Rel. energy in Figure 4.2. At the saddle point, the distance between the Li and S atoms of the image is the shortest, as indicated in Tables 4.1 and 4.2 for ABC and AC paths, respectively. The Rel. energy of Li diffusion indicates that there is a local minimum at the B point and the diffusion barrier is about 0.53 eV. However, the diffusion barrier of Na in MoS_2 is considerably high at 1.04 eV. The expanded interlayer spacing through intercalation results in relatively low diffusion barriers in K and Rb diffusion (0.28 and 0.26, respectively). This indicates that MoS_2 has the potential to be an electrode material for ion batteries. Although Li-ion batteries can archive high gravimetric and volumetric energy densities, the crust abundance of Li is very low, which cannot meet the growth demand of rechargeable batteries. Potassium has its own unique advantages over lithium or sodium as a charge carrier. However, K-ion batteries lack suitable electrode materials to host the relatively large K^+ ions. Our findings suggest that MoS_2 could host large K^+ ions as an electrode material for K-ion batteries.
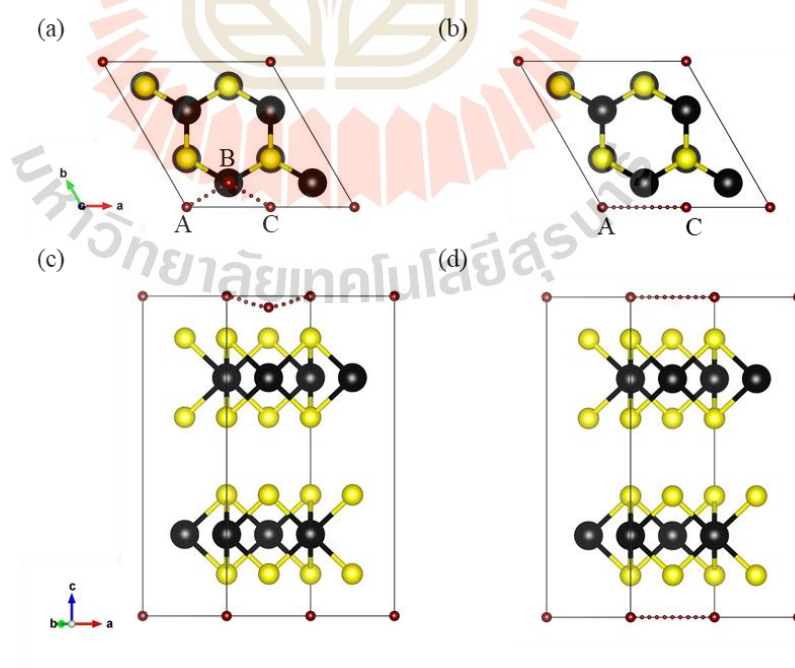
Figure 4.1   Minimum paths of Li diffusion along (a and c) the ABC path and (b and d) the AC path.

Rel. Energy of Li diffusion

Rel. Energy of Na diffusion

(a)

(b)

Rel. Energy of K diffusion

Rel. Energy of Rb diffusion

(c)

(d)
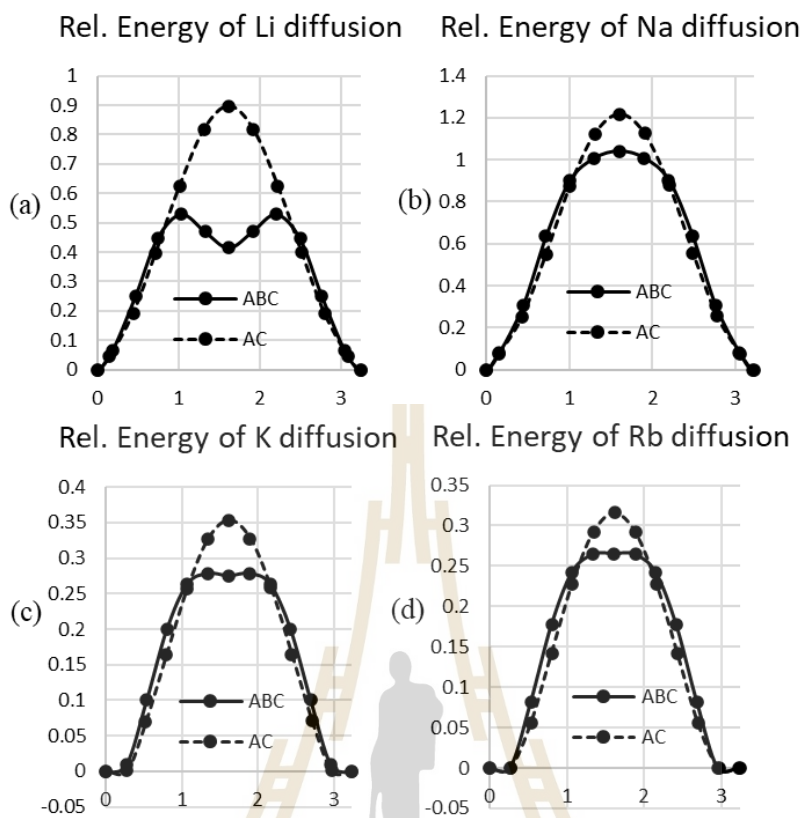
Figure 4.2   Rel. energy of Li, Na, K and Rb diffusion, respectively.

Table 4.1   Nearest neighbor of Li diffusion in MoS_2 along ABC where AB and CB paths are symmetric (* indicates the image that whose energy is the highest).

Images	nearest neighbor (Å)
0 (A)	2.49^S, 2.49^S, 2.49^S, 2.49^S, 2.49^S, 2.49^S, 3.66^{Mo}, 3.66^{Mo}, 3.66^{Mo}, 3.66^{Mo}, 3.66^{Mo}, 3.66^{Mo}
1	2.39^S, 2.43^S, 2.43^S, 2.61^S, 2.61^S, 2.65^S, 3.57^{Mo}, 3.68^{Mo}, 3.68^{Mo}, 3.75^{Mo}, 3.75^{Mo}, 3.84^{Mo}
2	2.28^S, 2.32^S, 2.32^S, 2.82^S, 2.82^S, 2.86^S, 3.35^{Mo}, 3.72^{Mo}, 3.72^{Mo}, 3.79^{Mo}, 3.79^{Mo}, 3.93^S
3	2.22^S, 2.25^S, 2.25^S, 3.07^S, 3.07^S, 3.10^S, 3.16^{Mo}, 3.80^{Mo}, 3.80^{Mo}, 3.86^{Mo}, 3.86^{Mo}, 3.89^S
4*	2.19^S, 2.21^S, 2.21^S, 2.88^S, 2.98^{Mo}, 3.34^S, 3.34^S, 3.87^S, 3.90^{Mo}, 3.90^{Mo}, 3.96^{Mo}, 3.96^{Mo}
5	2.19^S, 2.23^S, 2.23^S, 2.56^S, 2.84^{Mo}, 3.62^S, 3.62^S, 3.87^S, 4.02^{Mo}, 4.02^{Mo}, 4.10^{Mo}, 4.10^{Mo}
6 (B)	2.21^S, 2.30^S, 2.30^S, 2.31^S, 2.80^{Mo}, 3.88^S, 3.88^S, 3.88^S, 3.96^S, 4.12^{Mo}, 4.12^{Mo}, 4.12^{Mo}

Table 4.2   Nearest neighbor of Li diffusion in MoS$_2$ along AC (* indicates the image that whose energy is the highest).

Images	nearest neighbor (Å)
0 (A)	2.49^S, 2.49^S, 2.49^S, 2.49^S, 2.49^S, 2.49^S, 3.66^{Mo}, 3.66^{Mo}, 3.66^{Mo}, 3.66^{Mo}, 3.66^{Mo}, 3.66^{Mo}
1	2.44^S, 2.44^S, 2.52^S, 2.52^S, 2.61^S, 2.61^S, 3.64^{Mo}, 3.64^{Mo}, 3.71^{Mo}, 3.71^{Mo}, 3.78^{Mo}, 3.78^{Mo}
2	2.31^S, 2.31^S, 2.56^S, 2.56^S, 2.81^S, 2.81^S, 3.56^{Mo}, 3.56^{Mo}, 3.76^{Mo}, 3.76^{Mo}, 3.77^S, 3.94^{Mo}
3	2.22^S, 2.22^S, 2.63^S, 2.63^S, 3.04^S, 3.04^S, 3.49^{Mo}, 3.49^{Mo}, 3.57^S, 3.82^{Mo}, 3.82^{Mo}, 4.11^{Mo}
4	2.15^S, 2.15^S, 2.72^S, 2.72^S, 3.29^S, 3.29^S, 3.38^S, 3.44^{Mo}, 3.44^{Mo}, 3.90^{Mo}, 3.90^{Mo}, 4.29^{Mo}
5	2.11^S, 2.11^S, 2.85^S, 2.85^S, 3.18^S, 3.18^S, 3.40^{Mo}, 3.40^{Mo}, 3.54^S, 4.00^{Mo}, 4.00^{Mo}, 4.06^S
6*	2.10^S, 2.10^S, 3.00^S, 3.00^S, 3.00^S, 3.00^S, 3.39^{Mo}, 3.39^{Mo}, 3.80^S, 3.80^S, 4.11^{Mo}, 4.11^{Mo}
7	2.11^S, 2.11^S, 2.85^S, 2.85^S, 3.18^S, 3.18^S, 3.40^{Mo}, 3.40^{Mo}, 3.54^S, 4.00^{Mo}, 4.00^{Mo}, 4.06^S
8	2.15^S, 2.15^S, 2.72^S, 2.72^S, 3.29^S, 3.29^S, 3.38^S, 3.44^{Mo}, 3.44^{Mo}, 3.90^{Mo}, 3.90^{Mo}, 4.29^{Mo}
9	2.22^S, 2.22^S, 2.63^S, 2.63^S, 3.04^S, 3.04^S, 3.49^{Mo}, 3.49^{Mo}, 3.57^S, 3.82^{Mo}, 3.82^{Mo}, 4.11^{Mo}
10	2.31^S, 2.31^S, 2.56^S, 2.56^S, 2.81^S, 2.81^S, 3.56^{Mo}, 3.56^{Mo}, 3.76^{Mo}, 3.76^{Mo}, 3.77^S, 3.94^{Mo}
11	2.44^S, 2.44^S, 2.52^S, 2.52^S, 2.61^S, 2.61^S, 3.64^{Mo}, 3.64^{Mo}, 3.71^{Mo}, 3.71^{Mo}, 3.78^{Mo}, 3.78^{Mo}
12 (C)	2.49^S, 2.49^S, 2.49^S, 2.49^S, 2.49^S, 2.49^S, 3.66^{Mo}, 3.66^{Mo}, 3.66^{Mo}, 3.66^{Mo}, 3.66^{Mo}, 3.66^{Mo}

4.2   Co-intercalation

Since the atomic size of the intercalated alkali metal determines the expansion of interlayer spacing, co-intercalation with a larger atom cloud reduces the diffusion barrier of the smaller one. Co-interactions of Li and a larger-sized alkali metal (such as Na, K or Rb) were studied by calculating Li diffusions in bulk MoS$_2$ with various lattice parameters c. Figure 4.3(a) indicates Rel. energy of Li diffusion in MoS$_2$, monolayer MoS$_2$ and MoS$_2$ with a lattice parameter c equivalent to that of Na, K and Rb intercalation (C_{Na}=12.40, C_K=14.23 and C_{Rb}=14.52, respectively) along AC and ABC paths. In this graph, the Rel. energy of Li diffusion along the AC path is
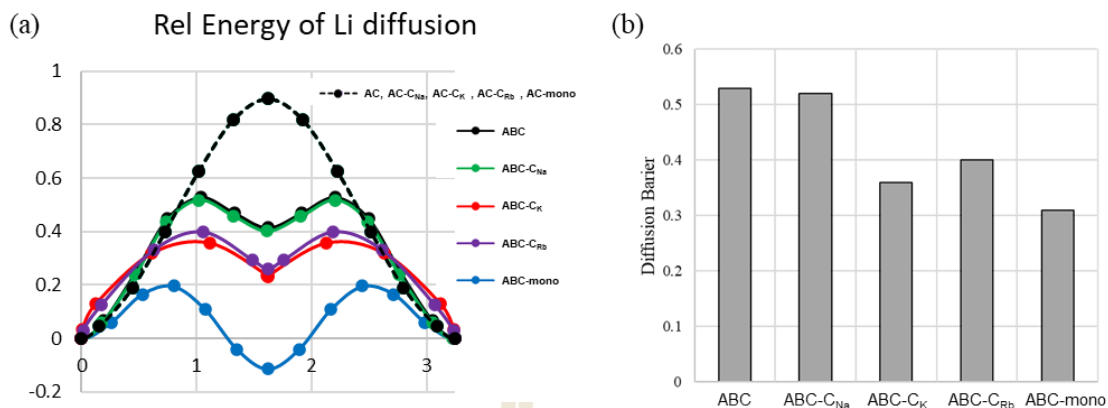
Figure 4.3   Rel. energy of Li diffusion in MoS_2, monolayer MoS_2 and MoS_2 with a lattice parameter c equivalent to that of Na, K, Rb intercalation and diffusion barriers with different lattice parameter c along the ABC path.

perfectly overlapping on the same line for every case. The results show that the diffusion barrier of Li along the AC path does not change with the lattice parameter c. However, the diffusion barrier of Li along the ABC path reduced by the increased lattice parameter c (see Figure 4.3(b)). Li diffusion in monolayer MoS_2 along the ABC path has the lowest diffusion barrier, where the energetically favorable position of Li changes to the B point instead. We proposed that this method has the potential to improve the charging ability of Li-ion batteries by varying the diffusion barrier of Li through co-intercalation.

The reaction rate, also known as the diffusion rate, indicates how easily atoms may flow into the electrodes of substances and can be a good indicator of how fast a battery can be charged. The Arrhenius equation can be used to estimate the reaction rate (k) as follows:

$$k = A_0 \exp\left(-E_b / k_B T\right), \tag{4.1}$$

where A_0 is diffusion pre-factor, E_b is the diffusion barrier, k_B is the Boltzmann constant and T is temperature. The ratio of the diffusion rate at a particular condition to the diffusion rate of Li–ions in MoS_2 having a lattice parameter $c = C*$ at 50 K is described as selectivity (S) which is given by

$$S = \frac{A_C(T)}{A_{C*}(T = 50K)} = \frac{A_{0,C} \exp(-E_b / k_B T)}{A_{0,C*} \exp(-E_b / 50 \cdot k_B)}, \tag{4.2}$$

where $A_C(T)$ is the diffusion rate in MoS$_2$ having a lattice parameter c at a given temperature, $A_{0,C}$ is diffusion pre–factor, E_b is the diffusion barrier, k_B is the Boltzmann constant and T is temperature. The diffusion barriers from Figure 4.3 (b) were used to calculate the selectivity as a function of temperature for the Li and co-intercalation atoms (Na, K and Rb). The lattice parameters change depending on the co-intercalation atom. To simplify the selectivity equation, the ratio of the diffusion pre–factor was assumed to be 1. Figure 4.4 shows the selectivity of Li and the co-intercalation of Na atoms, K atoms and Rb atoms as a function of temperature. The results indicate that the selectivity of the diffusion along the ABC path is slightly higher than that of the AC path. In the case of co-intercalation of Na, the selectivity of Li is higher than that of the co-intercalation atom. However, in the case of co-intercalation of K and Rb, the selectivity of Li is lower than that of the co-intercalation atom. The higher selectivity indicates that the atom can diffuse more easily compared to another one. For battery applications, Na has the potential to be a good co-intercalation atom because, during the deintercalation process, the expander (which is Na in this case) is expected to stay in MoS$_2$ to maintain volume and keep the diffusion barrier of the charge carrier (Li) low. On the other hand, co-intercalation of K and Rb diffuses more easily than the charge carrier (Li). Therefore, the electrode's volume is unstable and the diffusion barrier of Li changes during the deintercalation process. We suggested that the co-intercalation of Na could enhance the performance of Li-ion batteries with MoS$_2$ electrodes. Co-intercalation of Na can reduce volume changes during the charged/discharged process, leading to improved cycle stability over the long term for rechargeable batteries.
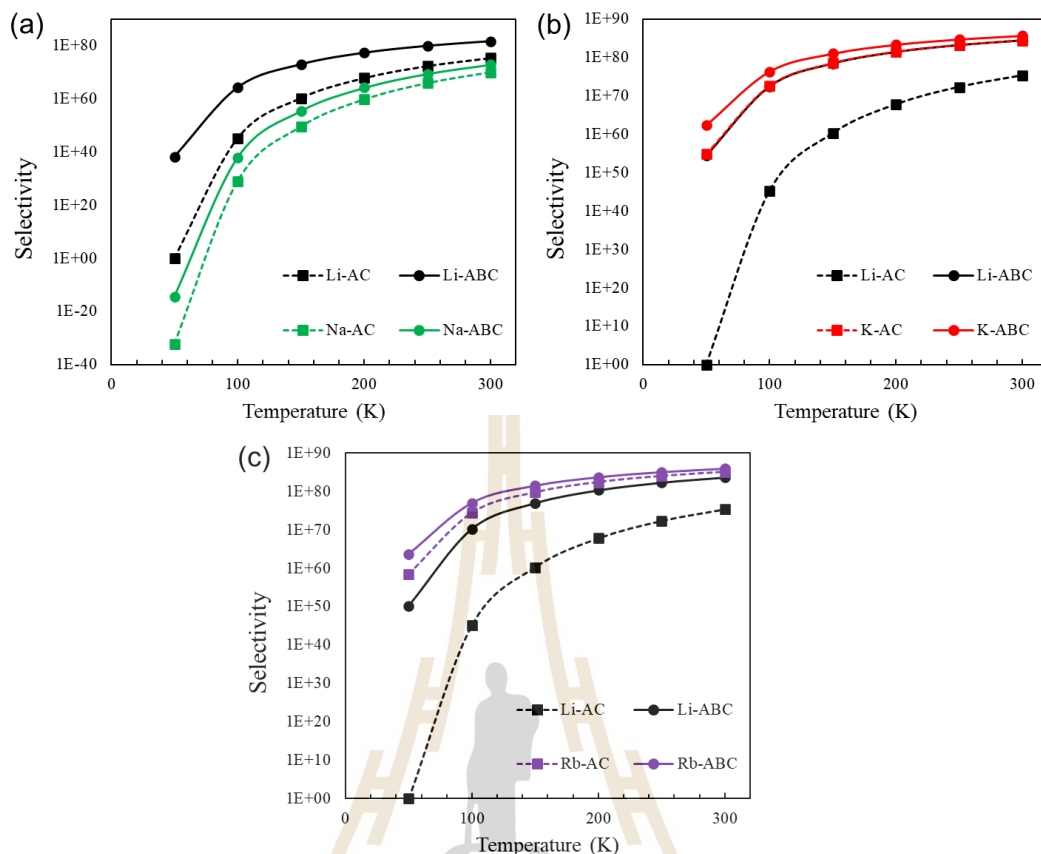
Figure 4.4 Selectivity of Li and the co-intercalation of (a) Na atom, (b) K atom and (c) Rb atom as a function of temperatures.

4.3 Charge Density Difference

In this section, charge density difference (CDD) was introduced to study the charged contribution of alkali metal to the MoS_2 layers. The CDD plot $(\Delta\rho)$ can be calculated as following,

$$\Delta\rho = \rho_{AB} - \rho_A - \rho_B \tag{4.3}$$

Where, ρ_{AB} is the full system, ρ_A is the substrate and ρ_B is the intercalating system.

The CDD plots of alkali metal intercalated MoS_2 at Hex-site in Figure 4.5 show that charge accumulated between alkali metal and S atoms indicated covalent bonds between alkali metal and S atoms, while charge accumulated at Mo atoms indicated ionic bonds between alkali metal and Mo atoms. The accumulated charge in the MoS_2 layer leads to charge repulsion, which makes the lattice parameter a

Table 4.3   The nearest neighbor of alkali metal (A) intercalated MoS_2 at Hex-site and Mo-top, where Li_{mono} denotes Li intercalated monolayer MoS_2.

Intercalated alkali metal (A)	A-Mo (Hex-site)	A-S (Hex-site)	A-Mo (Mo-top)	A-S (Mo-top)
Li_{mono}	3.33	2.28	2.85	2.33
Li	3.66	2.49	2.80	2.30
Na	3.78	2.61	3.09	2.50
K	4.52	3.20	3.93	3.07
Rb	4.65	3.33	3.84	2.98

increase as mentioned in Chapter III. In Figure 4.6, CDD plots of alkali metal intercalated MoS_2 at Mo-top indicate tetrahedral geometry between alkali metal and S atoms and the movement of alkali metal toward Mo atoms. Li intercalation has the most accumulated charge as shown in Figure 4.6(f) and has the shortest bond distance according to the Table 4.3. This could be the outcome of the local minimum at the B point for Li intercalation from the previous section.
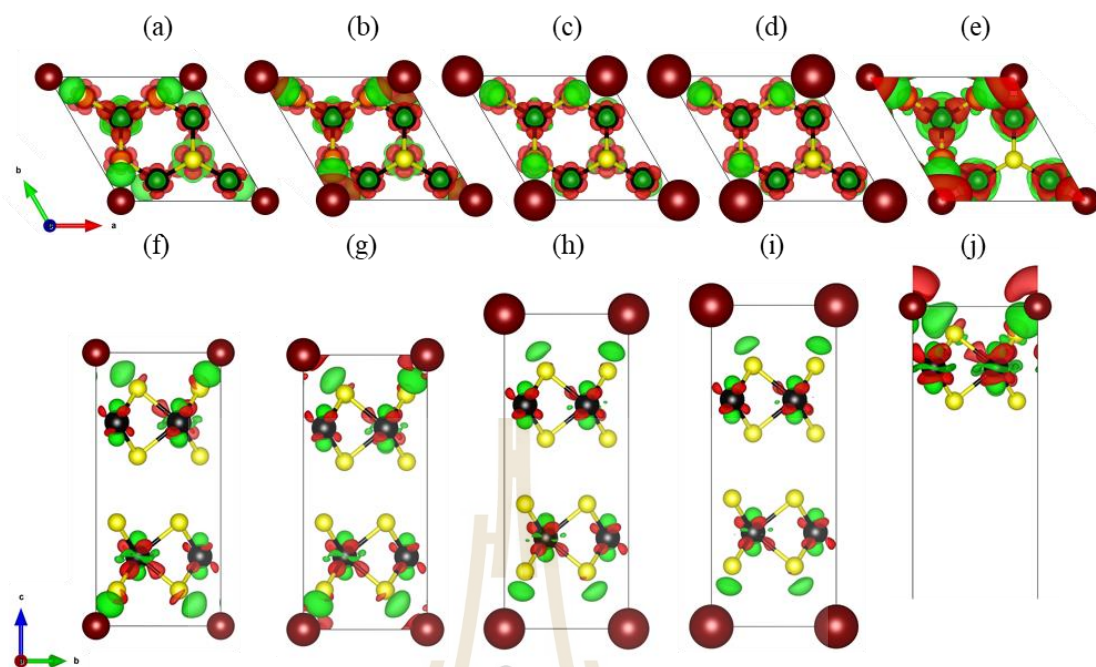
Figure 4.5 The CDD plot of (a, f) Li, (b, g) Na, (c, h) K, (d, i) Rb intercalated MoS_2 and (e, j) Li intercalated monolayer MoS_2 at Hex-site using isosurface = 0.002.
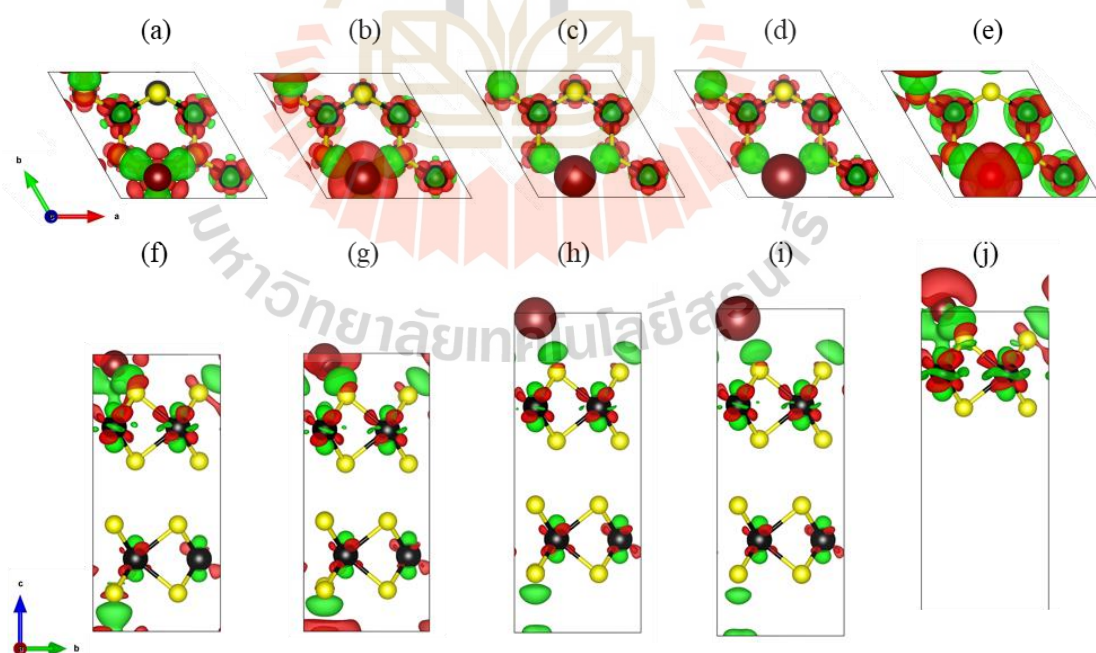
Figure 4.6 The CDD plot of (a, f) Li, (b, g) Na, (c, h) K, (d, i) Rb intercalated MoS_2 and (e, j) Li intercalated monolayer MoS_2 at Mo-top using isosurface = 0.002.

4.4   Optical Properties

At the microscopic level, the optical properties of MoS$_2$ and alkali metal intercalated MoS$_2$ will be described in this section. The Bethe-Salpeter equation (Jónsson *et al.*) was introduced to calculate frequency-dependent complex dielectric as a function of photon frequency $\varepsilon(\omega)$

$$\varepsilon(\omega) = \varepsilon_1(\omega) + i\varepsilon_2(\omega),\tag{4.4}$$

where $\varepsilon_1(\omega)$ and $\varepsilon_2(\omega)$ are real and imaginary parts of the dielectric function, respectively. The linear optical properties including refractive index $n(\omega)$, extinction coefficient $k(\omega)$, absorption coefficient $\alpha(\omega)$, energy-loss function $L(\omega)$ and reflectivity $R(\omega)$ can be calculated as following,

$$n(\omega) = \left[\frac{\sqrt{\varepsilon_1^2 + \varepsilon_2^2} + \varepsilon_1}{2} \right]^{\frac{1}{2}}\tag{4.5}$$

$$k(\omega) = \left[\frac{\sqrt{\varepsilon_1^2 + \varepsilon_2^2} - \varepsilon_1}{2} \right]^{\frac{1}{2}}\tag{4.6}$$

$$\alpha(\omega) = \frac{\sqrt{2}\omega}{c} \left[\sqrt{\varepsilon_1^2 + \varepsilon_2^2} - \varepsilon_1 \right]^{\frac{1}{2}}\tag{4.7}$$

$$L(\omega) = \frac{\varepsilon_2}{\varepsilon_1^2 + \varepsilon_2^2}\tag{4.8}$$

$$R(\omega) = \frac{(n-1)^2 + k^2}{(n+1)^2 + k^2}\tag{4.9}$$

Due to the intensive computation of BSE calculations, ENCUT =250 and KPOINT 3x3x3 were employed for optical calculations. Absorption coefficients of MoS$_2$ with different lattice parameters c and monolayer MoS$_2$ were calculated as shown in Figure 4.7. The results show that the absorption coefficient of pristine bulk MoS$_2$ (C$_0$) has a peak at 2.4 eV, which perhaps occurs during the direct transition between valence and conduction bands at Γ points. However, there is no peak that corresponds to calculated bandgaps of 0.93 or 0.97 eV from Section 3.3 of Chapter III due to the competition of the $E_g\left(\mathrm{K}_c - \Gamma_v\right)$ and $E_g\left(\Sigma_c - \Gamma_v\right)$ bandgaps. The absorption coefficient of monolayer MoS$_2$ occurs at a peak of 1.8 eV, which is a linear combination of the direct bandgap $E_g\left(\mathrm{K}_c - \mathrm{K}_v\right)$ of 1.65 eV and the indirect bandgap $E_g\left(\Sigma_c - \Gamma_v\right)$ of 1.95 eV. The increasing lattice parameter c corresponding

to the alkali metal intercalation indicates blue shifts ranging between 1.8-1.9 eV depending on atomic size. These peaks are in the visible range, which shows promise as optoelectronic devices.

However, the intercalation not only increases the lattice parameter c but also contributes electrons to the MoS_2 layers. Absorption coefficients of MoS_2 with lattice parameter c that equivalence to the MoS_2Li were calculated by varying the contributed electrons in the dilute limit. The increasing electron contribution leads to the red shifts with lower intensity, as indicated in Figure 4.8. Due to the drawback of decreasing intensity, we suggest keeping the smallest intercalated alkali metals to maximize the absorption coefficient for optoelectronic devices. In the case of high concentrations, the lower absorption coefficient enhances transparency in MoS_2, making it suitable for transparent electrodes such as touchscreen devices.
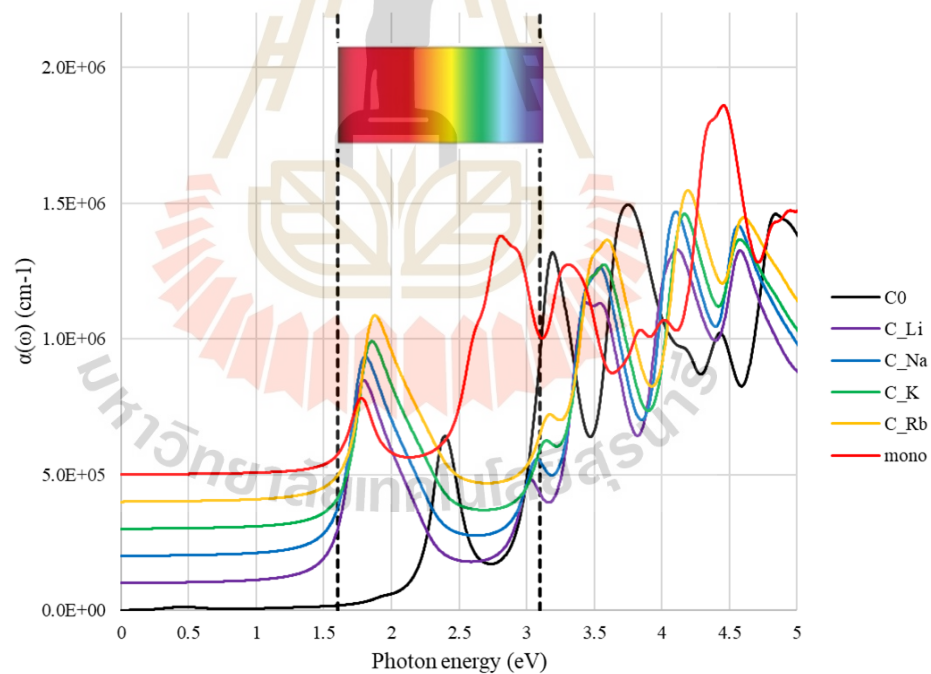
Figure 4.7 Absorption coefficients of MoS_2 with different lattice parameters c and monolayer MoS_2.
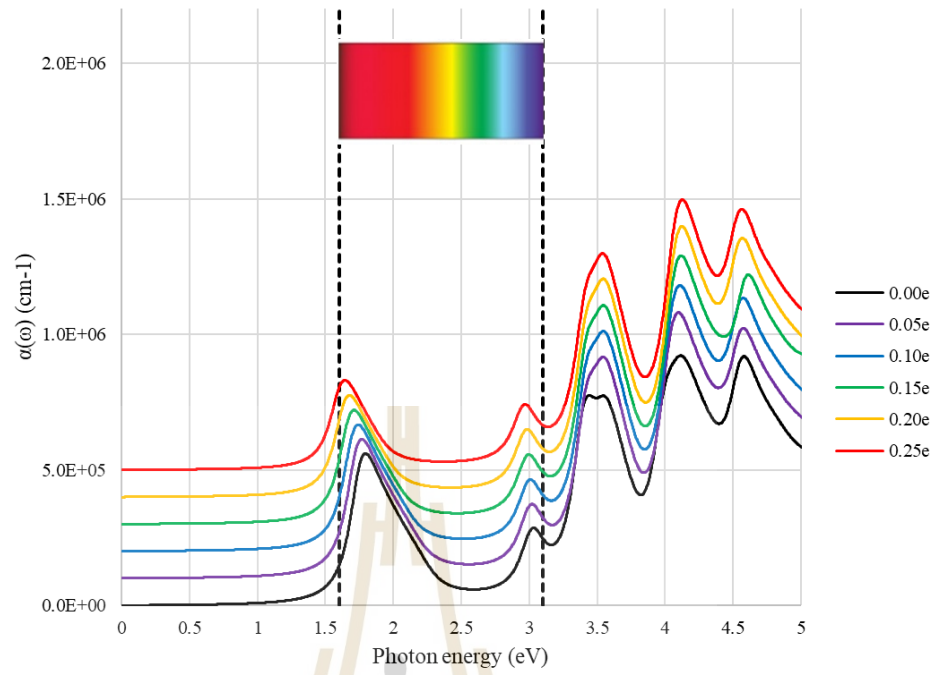
Figure 4.8 Absorption coefficients of MoS$_2$ where the lattice parameter c equivalence to that of MoS$_2$Li with various contributed electrons.

CHAPTER V

CONCLUSIONS AND FUTURE RESEARCH PLAN

5.1   Conclusions

In this thesis, the electronic and optical properties of MoS_2 intercalated alkali metal, which is a family member of transition metal dichalcogenide, were calculated by employing the first principles method. Crystal structure, electronic structure, electronic property and optical property were studied and discussed. The results are concluded as follows:

Pristine bulk MoS_2 and other TMDCs have a honeycomb structure of strongly boned layers with weak vdW interaction between layers, allowing exfoliation into monolayers. Bulk MoS_2 has an indirect bandgap, while the bandgap of monolayer MoS_2 changes to a direct bandgap due to quantum confinement. To study the influence of quantum confinement on the electronic structure of MoS_2, tensile strain was applied to pristine bulk MoS_2 by increasing the lattice parameter c. The increasing of c significantly alters the electronic structure and leads to the crossing over to a direct bandgap. These results give us an opportunity to tune the size and type of electronic structure of MoS_2 and other TMDCs by controlling interlayer spacing, such as by applying tensile strain and intercalating alkali metals into the interlayer gap.

The results of alkali metal intercalated MoS_2 indicate two significant effects on bulk MoS_2, including the expansion of interlayer spacing and the contribution of electrons. Due to the interlayer expansion, the lattice parameter c increased with the atomic size of the intercalated alkali metal. However, the increasing lattice parameter a is irrelevant to the atomic size. The high concentration makes the lattice parameter a increase because of charge repulsion from the donated electron. The results showed that both bandgap size and type are tunable through intercalation. The electronic structures of Li and Na intercalation have an indirect bandgap, which is similar to pristine bulk but with a larger bandgap. The same

feature of crossing over from indirect to direct bangap that has been found in monolayer occurs in K and Rb intercalation. Because K and Rb intercalations greatly increase the lattice parameter c, the interaction between layers is considerably reduced, reaching the isolated condition. The tunable bandgap, the enchantment in conductivity and the improved transparency of MoS_2 through intercalation have shown promise for optoelectronic, electronic and touch screen devices.

Alkali metal diffusion in MoS_2 was investigated by using the NEB method with CINEB improvement. The ABC path is the minimum path of alkali metal diffusion where A, B and C points are Hex-site, Mo-top and neighboring Hex-site, respectively. The Rel. energy of Li diffusion indicates that there is a local minimum at B point and the diffusion barrier is about 0.53 eV. However, the diffusion barrier of Na in MoS_2 is considerably high at 1.04 eV. The expanded interlayer spacing through intercalation results in relatively low diffusion barriers in K and Rb diffusion (0.28 and 0.26, respectively). This indicates that MoS_2 has the potential to be an electrode material for ion batteries. Since the atomic size of the intercalated alkali metal determines the expansion of interlayer spacing, co-intercalation with a larger atom cloud reduces the diffusion barrier of the smaller one. co-intercalation of Na, the selectivity of Li is higher than that of the co-intercalation atom. The higher selectivity indicates that the atom can diffuse more easily compared to another one. For battery applications, Na has the potential to be a good co-intercalation atom because, during the deintercalation process, the expander (which is Na in this case) is expected to stay in MoS_2 to maintain volume and keep the diffusion barrier of the charge carrier (Li) low. We suggested that the co-intercalation of Na could enhance the performance of Li-ion batteries with MoS_2 electrodes. Co-intercalation of Na can reduce volume changes during the charged/discharged process, leading to improved cycle stability over the long term for rechargeable batteries.

The charge density difference (CDD) was introduced to study the charged contribution of alkali metal to the MoS_2 layers. The results indicate that charge accumulated between alkali metal and S atoms indicated covalent bonds between alkali metal and S atoms, while charge accumulated at Mo atoms indicated ionic

bonds between alkali metal and Mo atoms. The accumulated charge in the MoS_2 layer leads to charge repulsion, which makes the lattice parameter a increase.

At the microscopic level, the optical properties of MoS_2 and alkali metal intercalated MoS_2 were calculated by using Bethe-Salpeter equation. The results show that the absorption coefficients of pristine bulk and monolayer MoS_2 have peaks at 2.4 eV and 1.8 eV, respectively. The increasing lattice parameter c corresponding to the alkali metal intercalation indicates blue shifts ranging between 1.8-1.9 eV depending on atomic size. These peaks are in the visible range, which shows promise as optoelectronic devices. However, the intercalation not only increases the lattice parameter c but also contributes electrons to the MoS_2 layers. The increasing electron contribution leads to red shifts with lower intensity. Due to the drawback of decreasing intensity, we suggest keeping the smallest intercalated alkali metals to maximize the absorption coefficient for optoelectronic devices. In the case of high concentrations, the lower absorption coefficient enhances transparency in MoS_2, making it suitable for transparent electrodes such as touchscreen devices.

5.2   Future Research Plan

The study of the electronic and optical properties of alkali metal intercalation can be extended across the entire family of TMDCs and other 2D layered structure materials such as MXenes, etc. The First-principal calculation to study electronic and optical properties can be performed using the same approach described in Chapter II.

The Python script written for plotting the unfolded band with orbital-projected needs to be improved further, such as by adding more functions for smearing and fixing band crossing interpolation.

REFERENCES
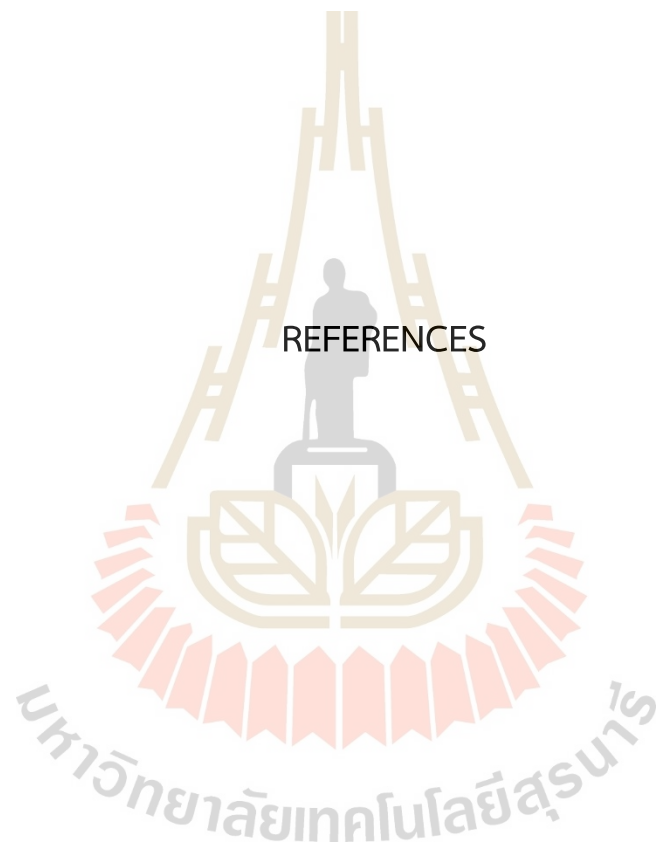
REFERENCES

Becke, A. D. (1993). A new mixing of Hartree–Fock and local density-functional theories. *J. Chem. Phys.*, *98*, 1372.

Bertolazzi, S., Brivio, J. and Kis, A. (2011). Stretching and breaking of ultrathin MoS_2. *ACS Nano*, *5*, 9703.

Bloch, F. (1929). Uber die quantenmechanik der elektronen in kristallgittern. *Z. Phys.*, *52*, 555.

Blöchl, P. E. (1994). Projector augmented-wave method. *Phys. Rev. B*, *50*, 17953.

Brandt, A., Bernholc, J. and Binder, K. (2001). *Multiscale computational methods in chemistry and physics*. IOS Press.

Bronsema, K. D., De Boer, J. L. and Jellinek, F. (1986). On the structure of molybdenum diselenide and disulfide. *Z. Anorg. Allg. Chem.*, *540*, 15.

Bucko, T., Hafner, J., Lebegue, S. and Angyan, J. G. (2010). Improved description of the structure of molecular and layered crystals: ab initio DFT calculations with van der Waals corrections. *J. Phys. Chem. A*, *114*, 11814.

Chang, C.-H., Fan, X., Lin, S.-H. and Kuo, J.-L. (2013). Orbital analysis of electronic structure and phonon dispersion in MoS_2, $MoSe_2$, WS_2, and WSe_2 monolayers under strain. *Phys. Rev. B*, *88*.

Cheng, F., Liang, J., Tao, Z. and Chen, J. (2011). Functional materials for rechargeable batteries. *Adv. Mater.*, *23*, 1695.

Desai, S. B., Seol, G., Kang, J. S., Fang, H., Battaglia, C., Kapadia, R., . . . Javey, A. (2014). Strain-induced indirect to direct bandgap transition in multilayer WSe_2. *Nano Lett.*, *14*, 4592.

Eknapakul, T., King, P. D., Asakawa, M., Buaphet, P., He, R. H., Mo, S. K., . . . Meevasana, W. (2014). Electronic structure of a quasi-freestanding MoS_2 monolayer. *Nano Lett.*, *14*, 1312.

Fan, X., Chang, C. H., Zheng, W. T., Kuo, J.-L. and Singh, D. J. (2015). The electronic properties of single-layer and multilayer MoS_2 under high pressure. *J. Phys. Chem. C*, *119*, 10189.

Fivaz, R. and Mooser, E. (1967). Mobility of charge carriers in semiconducting layer structures. *Phys. Rev.*, *163*, 743.

Gajdoš, M., Hummer, K., Kresse, G., Furthmüller, J. and Bechstedt, F. (2006). Linear optical properties in the projector-augmented wave methodology. *Phys. Rev. B*, *73*, 045112.

Geim, A. K. and Novoselov, K. S. (2007). The rise of graphene. *Nat. Mater.*, *6*, 183.

Grimme, S. (2006). Semiempirical GGA-type density functional constructed with a long-range dispersion correction. *J. Comput. Chem.*, *27*, 1787.

Hafner, J. (2008). Ab-initio simulations of materials using VASP: Density-functional theory and beyond. *J. Comput. Chem.*, *29*, 2044.

Hohenberg, P. and Kohn, W. (1964). Inhomogeneous electron gas. *Phys. Rev.*, *136*, B864.

Jiamprasertboon, A., Kongnok, T., Jungthawan, S., Kidkhunthod, P., Chanlek, N. and Siritanon, T. (2017). Investigation on crystal structures, optical properties, and band structure calculations of $In_{2-x}M_xTeO_6$ (M = Ga, Bi, La). *J. Alloys Compd.*, *702*, 601.

Jónsson, H., Mills, G. and Jacobsen, K. W. (1998) Nudged elastic band method for finding minimum energy paths of transitions. *Classical and quantum dynamics in condensed phase simulations*. (pp. 385). WORLD SCIENTIFIC.

Kam, K. K. and Parkinson, B. A. (1982). Detailed photocurrent spectroscopy of the semiconducting group VIB transition metal dichalcogenides. *J. Phys. Chem.*, *86*, 463.

Kerber, T., Sierka, M. and Sauer, J. (2008). Application of semiempirical long-range dispersion corrections to periodic systems in density functional theory. *J. Comput. Chem.*, *29*, 2088.

Kohn, W. (1999). Nobel Lecture: Electronic structure of matter---wave functions and density functionals. *Rev. Mod. Phys.*, *71*, 1253.

Kohn, W. and Sham, L. J. (1965). Self-consistent equations including exchange and correlation effects. *Phys. Rev.*, *140*, A1133.

Komesu, T., Le, D., Zhang, X., Ma, Q., Schwier, E. F., Kojima, Y., . . . Dowben, P. A. (2014). Occupied and unoccupied electronic structure of Na doped $MoS_2(0001)$. *Appl. Phys. Lett.*, *105*, 241602.

Kresse, G. and Furthmüller, J. (1996). Efficiency of ab-initio total energy calculations for metals and semiconductors using a plane-wave basis set. *Comput. Mater. Sci.*, *6*, 15.

Kresse, G. and Furthmüller, J. (1996). Efficient iterative schemes for ab initio total-energy calculations using a plane-wave basis set. *Phys. Rev. B*, *54*, 11169.

Kresse, G. and Hafner, J. (1993). Ab initiomolecular dynamics for open-shell transition metals. *Phys. Rev. B*, *48*, 13115.

Kresse, G. and Joubert, D. (1999). From ultrasoft pseudopotentials to the projector augmented-wave method. *Phys. Rev. B*, *59*, 1758.

Kuc, A., Zibouche, N. and Heine, T. (2011). Influence of quantum confinement on the electronic structure of the transition metal sulfideTS_2. *Phys. Rev. B*, *83*.

Latzke, D. W., Zhang, W., Suslu, A., Chang, T.-R., Lin, H., Jeng, H.-T., . . . Lanzara, A. (2015). Electronic structure, spin-orbit coupling, and interlayer interaction in bulk MoS_2 and WS_2. *Phys. Rev. B*, *91*.

Li, X.-L. and Li, Y.-D. (2004). MoS_2 Nanostructures: Synthesis and Electrochemical Mg^{2+} Intercalation. *J. Phys. Chem. B*, *108*, 13893.

Mak, K. F., Lee, C., Hone, J., Shan, J. and Heinz, T. F. (2010). Atomically thin MoS_2 : a new direct-gap semiconductor. *Phys. Rev. Lett.*, *105*, 136805.

Mills, G., Jónsson, H. and Schenter, G. K. (1995). Reversible work transition state theory: application to dissociative adsorption of hydrogen. *Surf Sci.*, *324*, 305.

Novoselov, K. S., Geim, A. K., Morozov, S. V., Jiang, D., Zhang, Y., Dubonos, S. V., . . . Firsov, A. A. (2004). Electric field effect in atomically thin carbon films. *Science*, *306*, 666.

Novoselov, K. S., Jiang, D., Schedin, F., Booth, T. J., Khotkevich, V. V., Morozov, S. V. and Geim, A. K. (2005). Two-dimensional atomic crystals. *Proc. Natl. Acad. Sci. U.S.A.*, *102*, 10451.

Peelaers, H. and Van de Walle, C. G. (2012). Effects of strain on band structure and effective masses in MoS_2. *Phys. Rev. B*, *86*.

Perdew, J. P., Burke, K. and Ernzerhof, M. (1996). Generalized gradient approximation made simple. *Phys. Rev. Lett.*, *77*, 3865.

Schrödinger, E. (1926). An undulatory theory of the mechanics of atoms and molecules. *Phys. Rev.*, *28*, 1049.

Siriroj, S., Simakachorn, P., Khumtong, N., Sukhonthamethirat, T., Chaiyachad, S., Chanprakhon, P., . . . Meevasana, W. (2018). *Statistical mechanics guides the motions of cm scale objects*. doi:10.48550/arXiv.1805.10812.

Splendiani, A., Sun, L., Zhang, Y., Li, T., Kim, J., Chim, C.-Y., . . . Wang, F. (2010). Emerging photoluminescence in monolayer MoS_2. *Nano Lett.*, *10*, 1271.

Su, X., Zhang, R., Guo, C., Zheng, J. and Ren, Z. (2014). Band engineering of dichalcogenide MX_2 nanosheets (M = Mo, W and X = S, Se) by out-of-plane pressure. *Phys. Lett. A*, *378*, 745.

Tomić, M., Jeschke, H. O. and Valentí, R. (2014). Unfolding of electronic structure through induced representations of space groups: Application to Fe-based superconductors. *Phys. Rev. B*, *90*, 195121.

Wang, H., Yuan, H., Sae Hong, S., Li, Y. and Cui, Y. (2015). Physical and chemical tuning of two-dimensional transition metal dichalcogenides. *Chem. Soc. Rev.*, *44*, 2664.

Xie, K., Yuan, K., Li, X., Lu, W., Shen, C., Liang, C., . . . Wei, B. (2017). Superior Potassium Ion Storage via Vertical MoS_2 "Nano-Rose" with Expanded Interlayers on Graphene. *Small*, *13*, 1701471.

Xiong, F., Wang, H., Liu, X., Sun, J., Brongersma, M., Pop, E. and Cui, Y. (2015). Li intercalation in MoS_2 : In situ observation of its synamics and tuning optical and electrical properties. *Nano Lett.*, *15*, 6777.

Yuan, L. and Huang, L. (2015). Exciton dynamics and annihilation in WS_2 2D semiconductors. *Nanoscale*, *7*, 7402.

Yun, W. S., Han, S. W., Hong, S. C., Kim, I. G. and Lee, J. D. (2012). Thickness and strain effects on electronic structures of transition metal dichalcogenides: 2H-MX_2 semiconductors (M=Mo, W;X=S, Se, Te). *Phys. Rev. B*, *85*.

Zhang, W., Liu, Y. and Guo, Z. (2019). Approaching high-performance potassium-ion batteries via advanced design strategies and engineering. *Sci Adv*, *5*, eaav7412.

Zhu, Z. Y., Cheng, Y. C. and Schwingenschlögl, U. (2011). Giant spin-orbit-induced spin splitting in two-dimensional transition-metal dichalcogenide semiconductors. *Phys. Rev. B*, *84*.
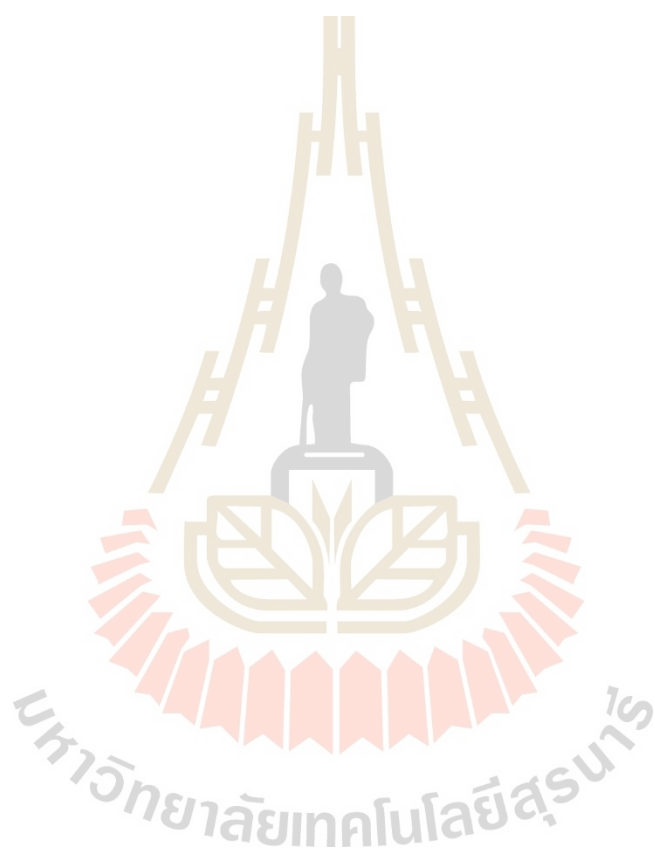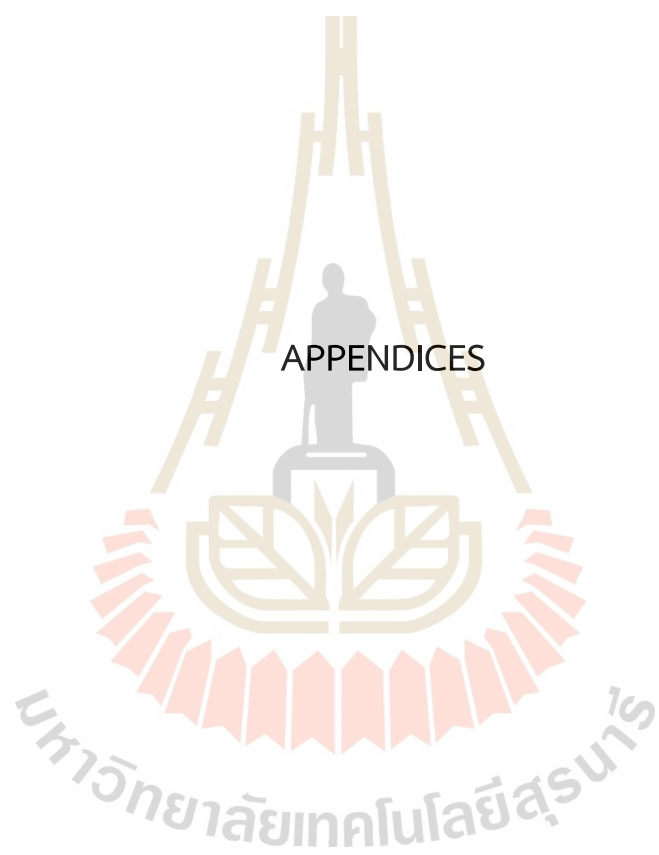
APPENDICES

APPENDIX A

ORBITAL-PROJECTED BAND STRUCTURE PLOTTING

Orbital-projected band structure is very useful information for studying physical properties of materials which includes the contribution of each atomic orbital of an atom to each band. However, conventional plots of band structure, including spaghetti diagrams, represent only energy and k-point data. Therefore, more information needs to be added in terms of colors and smearing. In the case of colors, they are used to exhibit each orbital or different atom. In the case of smearing, the weights of each orbital are translated into the thickness of the line by using a smearing function. This way, the orbital-projected band structure can be visualized. A Python script called PROPLOT was written to visualize an orbital-projected band structure. In this script, Laurent distribution was employed as a smearing function and discrete data obtained from VASP were interpolated by using Cubic spline method. The Python script for plotting band structure can be download by following link: https://www.dropbox.com/s/i8ov7m3sxct4v93/PROPLOT-setup.7z ?dl=0&fbclid=IwAR0MItXIyEuK66pBu9ixDnjNbQRIptpRZfWEFInOJKNmL1qoDyzkTMIkgus.

APPENDIX B

PUBLICATIONS AND PRESENTATIONS

B.1   List of publications

Jiamprasertboon, A., Kongnok, T., Jungthawan, S., Kidkhunthod, P., Chanlek, N. & Siritanon, T. (2017). Investigation on crystal structures, optical properties, and band structure calculations of $In_{2-x}M_xTeO_6$ (M = Ga, Bi, La). *J. Alloys Compd.*, *702*, 601.

Waehayee, A., Eknapakul, T., Chanlek, N., Kongnok, T., Rattanasuporn, S., Nakajima, H., . . . Siritanon, T. (2017). Electrical properties of (Cs1−xAx)Al0.33Te1.67O6 (A = K and Rb) mixed valence pyrochlores. *J. Alloys Compd.*

Siriroj, S., Simakachorn, P., Khumtong, N., Sukhonthamethirat, T., Chaiyachad, S., Chanprakhon, P., . . . Meevasana, W. (2018). *Statistical mechanics guides the motions of cm scale objects*. doi:10.48550/arXiv.1805.10812.

Kolodiazhnyi, T., Tipsawat, P., Charoonsuk, T., Kongnok, T., Jungthawan, S., Suthirakun, S., . . . Maensiri, S. (2019). Disentangling small-polaron and Anderson-localization effects in ceria: Combined experimental and first-principles study. *Phys. Rev. B*, *99*.

Pandech, N., Kongnok, T., Palakawong, N., Limpijumnong, S., Lambrecht, W. & Jungthawan, S. (2020). Effects of the van der Waals Interactions on Structural and Electronic Properties of CH_3NH_3 $(Pb,Sn)(I,Br,Cl)_3$ Halide Perovskites. *ACS Omega*, *5*, 25723.

B.2   List of presentation (oral)

Kongnok, T., Jungthawan, S., Limpijumnong, S. (November 2015). First-Principles Study of Alkali Metal Intercalated in 2H-MoS$_2$. In *Congress on Science and Technology of Thailand 2015*. Nakhon Ratchasima, Thailand.

Kongnok, T., Jungthawan, S., Limpijumnong, S. (June 2016). First-Principles Study of Alkali Metal Intercalated in 2H-MoS$_2$. In *Siam Physics Congress 2016*. Ubon Ratchathani, Thailand.

Kongnok, T., Jungthawan, S., Limpijumnong, S. (February 2020). Unfolding of supercell-band structure from density functional theory calculation and visualization of the unfolded band with orbital-projected. In *International Union of Materials Research Societies- International Conference in Asia 2020*. Chiang Mai, Thailand.

B.3   List of presentation (poster)

Kongnok, T., Jungthawan, S., Limpijumnong, S. (June 2015). First-Principles Study of Alkali Metal Intercalated in Transition Metal Dichalcogenides. In *Asian Consortium on Computational Materials Science 2015 (ACCMS-8)*. Taipei, Taiwan.

Kongnok, T., Jungthawan, S., Limpijumnong, S. (August 2017). First-Principles Study of Electronic and Optical Properties of Alkali Metal Intercalated Transition Metal Dichalcogenides. In *Asian Consortium on Computational Materials Science 2017 (ACCMS-9)*. Kuala Lumpur, Malaysia.

Kongnok, T., Jungthawan, S., Limpijumnong, S. (November 2017). First-Principles Study of Electronic and Optical Properties of Alkali Metal Intercalated Transition Metal Dichalcogenides. In *Asian Network School and Workshop on Complex Condensed Matter Systems 2017*. Hanoi, Vietnam.

ELSEVIER

CrossMark

Investigation on crystal structures, optical properties, and band structure calculations of $In_{2-x}M_xTeO_6$ (M = Ga, Bi, La)

Arreerat Jiamprasertboon [a], Thanundon Kongnok [b], Sirichok Jungthawan [b, c], Pinit Kidkhunthod [d], Narong Chanlek [d], Theeranun Siritanon [a, c, e, *]

[a] School of Chemistry, Institute of Science, Suranaree University of Technology, 111 University Avenue, Muang, Nakhon Ratchasima, 30000, Thailand
[b] School of Physics, Institute of Science, Suranaree University of Technology, 111 University Avenue, Muang, Nakhon Ratchasima, 30000, Thailand
[c] NANOTEC-SUT Center of Excellence on Advanced Functional Nanomaterials, Suranaree University of Technology, 111 University Avenue, Muang, Nakhon Ratchasima, 30000, Thailand
[d] Synchrotron Light Research Institute, Nakhon Ratchasima, 30000, Thailand
[e] Center of Excellence-Advanced Functional Materials, Suranaree University of Technology, 111 University Avenue, Muang, Nakhon Ratchasima, 30000, Thailand

ARTICLE INFO

ABSTRACT

The study of structure, optical properties, and band structure of M substituted-In_2TeO_6 (M = Ga^{3+}, Bi^{3+}, and La^{3+}) is presented. Solubility limit of each cation is different varying from 10% for La^{3+} to 20% for Ga^{3+} and 25% for Bi^{3+}. Both XANES and XPS confirm the oxidation states of Bi^{3+} and Te^{6+}. Crystallographic data of bond lengths and bond angles suggest no significant distortion of M-O_6 octahedra for all samples; however, the stereoactive $6s^2$ lone-pair electrons in Bi cause In/Bi cation in In/Bi–O_6 to shift toward one edge of the octahedra. The band structure calculation was useful to clarify that the fundamental band gap energies of all series originate from the direct allowed transition. Interestingly, Bi greatly influences the conduction band dispersion and Bi 6s state additionally contributes at the valence band maximum, while the valence band of other M-doped samples are mainly O 2p and In 4d in character. All compounds similarly exhibit photoluminescence properties. The strong PL peak mainly originated from the near band edge transition and the broad peak from Te^{6+}–O charge transfer are observed in all samples.

1. Introduction

Ternary metal tellurates with the general formula M_2TeO_6, when M is a trivalent cation, crystallize in different crystal structures: trirutile ($P4_2/mnm$), Na_2SiF_6-type (P_{321}), and orthorhombic La_2TeO_6-type ($P2_12_12_1$). The size of M^{3+} in M_2TeO_6 plays an important role in its crystal structure. Trirutile structure is formed when M, such as Cr, Fe, Rh [1], Ga [2,3], and Al [3], has ionic radii in the range of 0.5–0.7 Å. The bigger M cations (r = 0.745–0.87 Å) like In Ref. [4], Lu [4,5], and Sc [6,7] prefer Na_2SiF_6-type structure. The even bigger M cation (>0.87 Å), such as Gd, La, Sm, and Y [8], usually form La_2TeO_6-type structure. Nevertheless, there are some exceptions. Na_2SiF_6-type structure is also formed for Tl^{3+} (0.885 Å) [9], although the size of

Tl^{3+} drops into the last category. Both Na_2SiF_6-type and La_2TeO_6-type structure could be formed with Yb^{3+} as its size (0.868 Å) is in the borderline [10,11]. Additionally, Bi_2TeO_6 prefers a layered structure with orthorhombic lattice ($Cmca$) [12] because of the constituent $6s$ stereoactive lone-pair electrons.

Indium tellurium oxide (In_2TeO_6) was first prepared from In_2O_3 and H_6TeO_6 by solid state reaction [10]. Redman et al. later found that In_2TeO_6 is formed after heating $In_2Te_3O_9$ at temperature higher than 650 °C in air [13]. Two space groups have been reported for In_2TeO_6 as P_{321} [14] and $P\bar{3}\,m_1$ [15]. There are only few reports on electronic properties of In_2TeO_6 related compounds. Here, the stoichiometric In_2TeO_6 is insulator [16], oxygen-deficient In_2TeO_{6-x} behaves as a degenerate semiconductor [15]. $In_2Te_{6-x}Re_xO_6$ is also reported to be a semiconductor having lower conductivity [15]. Few elements have been used to substitute In in In_2TeO_6 in attempt to create extrinsic semiconductors. Only Sn and Zr doped In_2TeO_6 have been reported to show n-type semiconducting behavior. On the other hand, Zn-doped In_2TeO_6 is insulating and there is no

* Corresponding author. School of Chemistry, Institute of Science, Suranaree University of Technology, 111 University Avenue, Muang, Nakhon Ratchasima, 30000, Thailand.
E-mail address: theeranun@sut.ac.th (T. Siritanon).

Manuscript published in Journal of Alloys and Compounds

report of p-type semiconducting behavior for doped-In_2TeO_6 samples [16]. Recently, compositionally controlled metal insulator transition was observed in $Tl_{2-x}In_xTe_xO_6$ solid solution [17]. As the optical band gap of In_2TeO_6 is large and some compounds in this family have been reported to show semiconducting behavior, it might be possible to design transparent conducting oxides (TCOs) based on In_2TeO_6. In addition, the theoretical study, derived from the density functional theory (DFT), suggests that In_2TeO_6 has the capability to be a good n-type TCO considering its low effective mass, which result in high carrier mobility. On the other hand, the relatively large E_g (slightly lower than 3 eV) could result in little light absorption [18]. Information on the structure, electronic, and optical properties of the related compounds are, therefore, the important keys to develop these materials for future applications.

In the present article, we report the preparation, structural studies, optical properties, and electronic band structure calculations of Ga, Bi, and La-doped In_2TeO_6. The Rietveld refinement is carried out to solve the crystallographic information including cell parameters, cell volumes, bond lengths, and occupancies. Oxidation states of cations are investigated by X-ray absorption near-edge spectroscopy (XANES) and X-ray photoelectron spectroscopy (XPS) technique. In addition, scanning electron microscopy coupled with energy dispersive X-ray spectroscopy (SEM-EDS) is used to study morphology, particle size, and elemental composition of the samples. The optical properties are studied via UV—Visible spectroscopy and photoluminescence (PL) experiment to explore the absorption and re-emitting phenomena. Additionally, the electronic band structure calculation supplies more information about electronic structure of the compounds. The obtained results are used to explain the relationships between structure, composition, and properties of the materials.

2. Experimental details

Pure phase of all polycrystalline samples were obtained by conventional solid state reaction. High purity of In_2O_3 (Sigma-Aldrich, 99.99%), TeO_2 (Sigma-Aldrich, 99+%), Bi_2O_3 (Acros organic, 99.9%), Ga_2O_3 (Sigma-Aldrich, 99.99%), and La_2O_3 (Acros
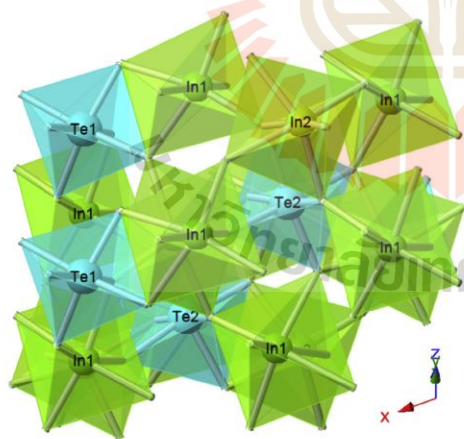
Fig. 1. Crystal structure of ideal In_2TeO_6.
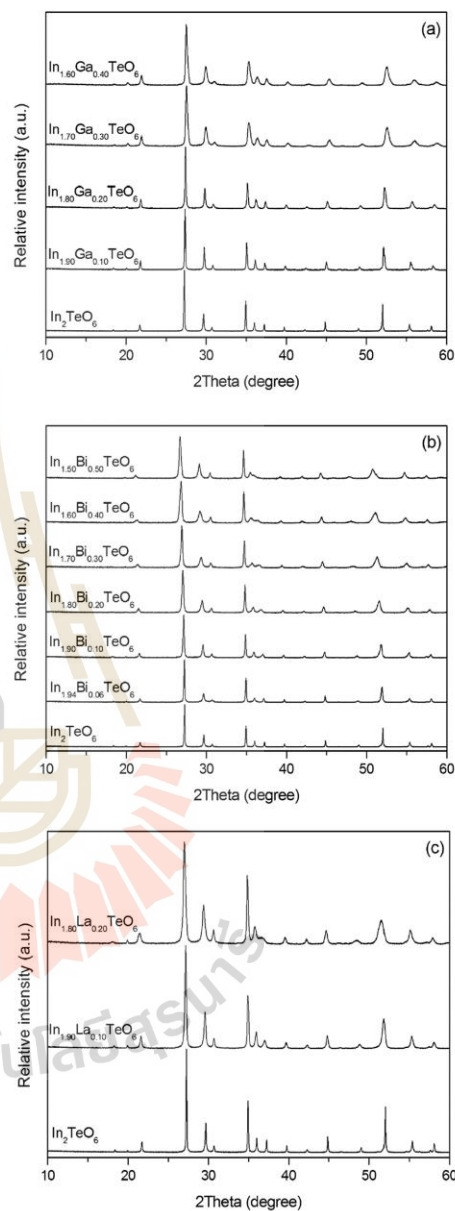
Fig. 2. X-ray diffraction patterns of (a) $In_{2-x}Ga_xTeO_6$ (x = 0—0.40), (b) $In_{2-x}Bi_xTeO_6$ (x = 0—0.50), and (c) $In_{2-x}La_xTeO_6$ (x = 0—0.20).

Manuscript published in Journal of Alloys and Compounds
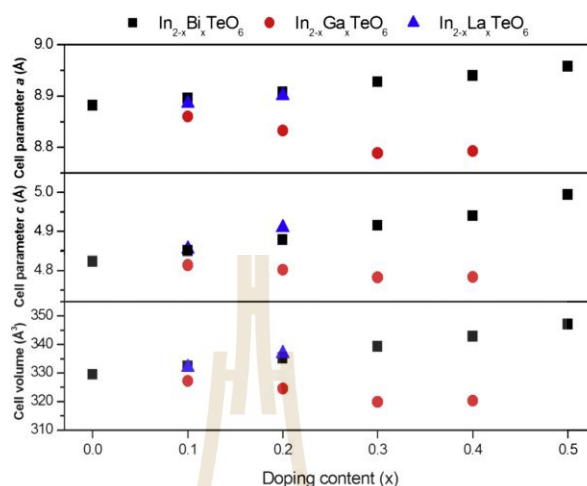
Fig. 3. Cell parameters a, c, and cell volume of $In_{2-x}Ga_xTeO_6$ (red circle), $In_{2-x}Bi_xTeO_6$ (black square), and $In_{2-x}La_xTeO_6$ (blue triangle). (For interpretation of the references to colour in this figure legend, the reader is referred to the web version of this article.)

organic, 99.99%) were used as starting materials. La_2O_3 was preheated at 850 °C prior to weighting. In the procedure, the stoichiometric mixtures were heated at 700 °C with different holding time and atmosphere. $In_{2-x}Bi_xTeO_6$ (x = 0, 0.1, 0.2, 0.3, 0.4, 0.5), $In_{2-x}Ga_xTeO_6$ (x = 0, 0.1, 0.2, 0.3, 0.4), and $In_{2-x}La_xTeO_6$ (x = 0, 0.1, 0.2) were heated for 12 h in air, 12—24 h in air, and 4 h in O_2, respectively. To solve the issue of Te volatilization in In_2TeO_6 and $In_{2-x}Ga_xTeO_6$, extra TeO_2 was added and the samples were washed with hot 50% v/v HCl to remove the excess TeO_2 after heating.

To identify the phase purity, powder X-ray diffraction (XRD) measurement was carried out by a Bruker D2 Phaser diffractometer with Cu Kα radiation (λ = 1.5406 Å). High quality XRD patterns were collected in the 2-theta range of 12—120° with an increment of 0.02° by a scan rate of 2s/step. Rietveld refinement, using TOPAS software, was applied to collect crystallographic data. Scanning electron microscopy (SEM) images were taken using a FEI quanta 450 SEM with a magnification of 24,000, operated with the accelerating voltage of 20 kV and working distance of 9.9 mm. Energy dispersive X-ray spectroscopy (EDS), using the Oxford instrument (model X-Max 50 mm) was utilized with area analysis. X-ray absorption near-edge structure (XANES) and X-ray photoelectron spectroscopy (XPS) were performed at the SUT-NANOTEC-SLRI XAS Beamline (BL5.2) and the SUT-NANOTEC-SLRI XPS Beamline (BL5.1), the SUT-NANOTEC-SLRI joint research facility, Synchrotron Light Research Institute (SLRI), Thailand (electron energy of 1.2 GeV, beam current of 80—120 mA). XANES spectra of Bi M_5-edge and Te L_3-edge were obtained by using InSb (111) and Ge (220) crystal, respectively. The spectra were normalized by the ATHENA program prior to the data analysis. XPS spectra of Bi $4f_{7/2}$, Te $3d_{5/2}$, and O 1s were recorded by a PHI5000 VersaProbe II XPS instruments (ULVAC-PHI, Japan) with monochromatic X-ray of Al $K_α$ (1486.6 eV). The C 1s peaks at 284.8 eV were used as a reference for binding energy calibration. Optical diffused reflectance spectroscopy (DRS) was probed by an Agilent UV—Vis—NIR spectrophotometer (model Cary 5000). The scan wavelength range of 200—800 nm with the

double beam mode was used to collect diffused reflectance (%R) spectra. Photoluminescence measurement was carried out utilizing an AVANTES AvaSpec-2048TEC-USB2-2 spectrometer with the excitation LED light source of 255 nm. Electronic structures were calculated based on density functional theory (DFT) by using the VASP code [19]. The Perdew, Burke, Ernzerhof (PBE) [20] exchange-correlation function implemented with the projector augmented wave method (PAW) [21,22] was employed. The $2 \times 2 \times 1$ supercell, comprising of 108 atoms, was used to study $In_{2-x}M_xTeO_6$ where M_x = $Ga_{0.417}$, $La_{0.250}$, and $Bi_{0.500}$. The compounds with different compositions were modeled by placing a number of M atoms randomly on In-site (24 sites) according to
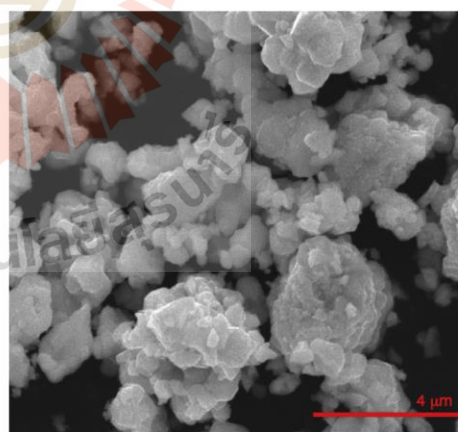
Fig. 4. SEM image of $In_{1.90}Bi_{0.10}TeO_6$.

Manuscript published in Journal of Alloys and Compounds

Table 1
Rietveld refinement parameters of $In_{2-x}Ga_xTeO_6$ (x = 0, 0.20, 0.40), $In_{2-x}Bi_xTeO_6$ (x = 0, 0.10, 0.30, 0.50), and $In_{2-x}La_xTeO_6$ (x = 0, 0.10, 0.20).

|	a (Å)	c (Å)	V (Å^3)	%R_{exp}	%R_p	%R_{wp}
In_2TeO_6	8.88211(5)	4.82304(4)	329.529(5)	2.73	7.68	9.91
$In_{1.80}Ga_{0.20}TeO_6$	8.8332(2)	4.8025(2)	324.52(2)	3.158	9.222	14.632
$In_{1.60}Ga_{0.40}TeO_6$	8.7943(4)	4.7830(3)	320.36(4)	3.177	8.571	11.164
$In_{1.90}Bi_{0.10}TeO_6$	8.8958(2)	4.8499(1)	332.38(2)	2.659	7.149	9.591
$In_{1.70}Bi_{0.30}TeO_6$	8.9278(3)	4.9149(3)	339.26(3)	2.61	7.563	10.126
$In_{1.50}Bi_{0.50}TeO_6$	8.9581(5)	4.9941(4)	347.07(5)	2.491	6.569	8.581
$In_{1.90}La_{0.10}TeO_6$	8.8863(4)	4.8550(3)	332.02(3)	3.103	11.559	15.71
$In_{1.80}La_{0.20}TeO_6$	8.9012(5)	4.9096(4)	336.88(5)	3.113	10.987	15.141

Table 2
Crystallographic data of $In_{2-x}Ga_xTeO_6$ (x = 0, 0.20, 0.40), $In_{2-x}Bi_xTeO_6$ (x = 0, 0.10, 0.30, 0.50), and $In_{2-x}La_xTeO_6$ (x = 0, 0.10, 0.20).

Atom	Site	x	y	z	Occupancy	$B_{eq.}$ (Å^2)
In_2TeO_6						
In1	3e	0.6305(2)	0	0	1	0.49
In2	3f	0.2943(2)	0	1/2	1	0.44
Te2	2d	1/3	2/3	0.5023(28)	1	0.25
O1	6g	0.0906(33)	0.8744(37)	0.7707(15)	1	0.93
O2	6g	0.4584(40)	0.5835(42)	0.7494(20)	1	2.43
O3	6g	0.2142(31)	0.7620(27)	0.2723(19)	1	1.04
$In_{1.80}Ga_{0.20}TeO_6$						
In1/Ga	3e	0.6316(3)	0	0	0.854(16)/0.146(16)	0.49
In2/Ga	3f	0.2939(4)	0	1/2	0.946(16)/0.054(16)	0.44
Te2	2d	1/3	2/3	0.5162(14)	1	0.25
O1	6g	0.1072(41)	0.8751(42)	0.7933(30)	1	0.93
O2	6g	0.4681(52)	0.5914(52)	0.7713(37)	1	2.43
O3	6g	0.2286(50)	0.7669(33)	0.2620(33)	1	1.04
$In_{1.60}Ga_{0.40}TeO_6$						
In1/Ga	3e	0.6302(4)	0	0	0.846(13)/0.154(13)	0.49
In2/Ga	3f	0.3004(4)	0	1/2	0.754(13)/0.246(13)	0.44
Te2	2d	1/3	2/3	0.5106(18)	1	0.25
O1	6g	0.0933(39)	0.8604(40)	0.7755(24)	1	0.93
O2	6g	0.4576(51)	0.5643(45)	0.7519(28)	1	2.43
O3	6g	0.2430(43)	0.7562(29)	0.2301(30)	1	1.04
$In_{1.90}Bi_{0.10}TeO_6$						
In1/Bi	3e	0.6293(2)	0	0	0.9/0.1	0.49
In2	3f	0.2932(2)	0	1/2	1	0.44
Te2	2d	1/3	2/3	0.5090(17)	1	0.25
O1	6g	0.0933(30)	0.8828(40)	0.7778(21)	1	0.93
O2	6g	0.4537(33)	0.5771(46)	0.7506(27)	1	2.43
O3	6g	0.2126(35)	0.7632(26)	0.2934(24)	1	1.04
$In_{1.70}Bi_{0.30}TeO_6$						
In1/Bi	3e	0.6283(2)	0	0	0.7/0.3	0.49
In2	3f	0.2917(3)	0	1/2	1	0.44
Te2	2d	1/3	2/3	0.5106(20)	1	0.25
O1	6g	0.1013(25)	0.8854(39)	0.7699(32)	1	0.93
O2	6g	0.4574(27)	0.5739(42)	0.7544(37)	1	2.43
O3	6g	0.2136(29)	0.7620(27)	0.3145(38)	1	1.04
$In_{1.50}Bi_{0.50}TeO_6$						
In1/Bi	3e	0.6255(2)	0	0	0.5/0.5	0.49
In2	3f	0.2921(3)	0	1/2	1	0.44
Te2	2d	1/3	2/3	0.5122(22)	1	0.25
O1	6g	0.1065(27)	0.8868(32)	0.7641(40)	1	0.93
O2	6g	0.4677(26)	0.5821(38)	0.7505(46)	1	2.43
O3	6g	0.2261(27)	0.7731(24)	0.3221(45)	1	1.04
$In_{1.90}La_{0.10}TeO_6$						
In1/La	3e	0.6340(3)	0	0	0.9/0.1	0.49
In2	3f	0.2874(3)	0	1/2	1	0.44
Te2	2d	1/3	2/3	0.5249(12)	1	0.25
O1	6g	0.0906(26)	0.8685(28)	0.7750(37)	1	0.93
O2	6g	0.4497(35)	0.5760(39)	0.7497(45)	1	2.43
O3	6g	0.2231(33)	0.7718(35)	0.3122(41)	1	1.04
$In_{1.80}La_{0.20}TeO_6$						
In1/La	3e	0.6314(4)	0	0	0.8/0.2	0.49
In2	3f	0.2880(4)	0	1/2	1	0.44
Te2	2d	1/3	2/3	0.4818(14)	1	0.25
O1	6g	0.1058(42)	0.8840(47)	0.7635(34)	1	0.93
O2	6g	0.4542(54)	0.5969(52)	0.7257(39)	1	2.43
O3	6g	0.2187(40)	0.7799(36)	0.3060(43)	1	1.04

$B_{eq.}$ = equivalent isotropic thermal parameters.

Manuscript published in Journal of Alloys and Compounds

Table 3
Bond lengths and average bond lengths of In–O and Te–O.

M_x	In_2TeO_6	$Ga_{0.2}$	$Ga_{0.4}$	$Bi_{0.1}$	$Bi_{0.3}$	$Bi_{0.5}$	$La_{0.1}$	$La_{0.2}$
In1−O1 (Å)	2.195(27)	2.115(30)	1.900(29)	2.250(30)	2.300(29)	2.355(25)	2.116(23)	2.274(33)
In1−O2 (Å)	2.049(29)	2.031(36)	2.064(29)	2.006(32)	1.980(29)	2.038(28)	2.031(29)	2.231(36)
In1−O3 (Å)	2.118(19)	2.163(31)	2.153(29)	2.184(21)	2.275(20)	2.400(21)	2.302(22)	2.285(28)
In2−O1 (Å)	2.050(18)	2.025(22)	2.080(21)	2.052(18)	1.989(17)	1.961(20)	2.001(18)	1.922(24)
In2−O2 (Å)	2.251(26)	2.239(34)	2.205(32)	2.298(22)	2.309(20)	2.245(21)	2.359(24)	2.279(33)
In2−O3 (Å)	2.163(20)	2.166(26)	2.332(24)	2.108(20)	2.085(22)	2.017(21)	2.028(26)	1.979(33)
Te1−O1 (Å)	2.003(32)	2.036(40)	2.083(30)	1.950(33)	2.017(31)	2.072(29)	2.084(27)	2.067(41)
Te2−O2 (Å)	2.005(37)	2.038(44)	2.079(44)	2.002(36)	2.065(33)	2.087(32)	1.935(34)	1.909(49)
Te2−O3 (Å)	1.991(28)	1.987(39)	1.917(30)	1.977(30)	1.925(29)	1.910(27)	1.953(34)	1.957(35)

the specified concentration. The cutoff energy was set at 520 eV and a Γ-centered $2 \times 2 \times 9$ Monkhorst-Pack k-mesh was used for the Brillouin zone integrations. Structural relaxation was performed until the force on each ion is below 0.01 eV/Å. The optimized lattice parameter a and c of In_2TeO_6 are 9.07 Å and 4.93 Å which are in good agreement with the cell parameters reported in Fig. 3. The electronic structures, obtained from supercell calculations, were unfolded onto the high symmetry paths as defined in the first Brillouin zone of the primitive cell [23].

3. Results and discussion

3.1. Crystal structure

In_2TeO_6 has hexagonal Na_2SiF_6-type structure (P_{321}). The structure mainly consists of the three-dimensional corner sharing network of InO_6 octahedra (Fig. 1). The octahedral units of Te are not connected with each other but connected to InO_6 units by edge sharing.
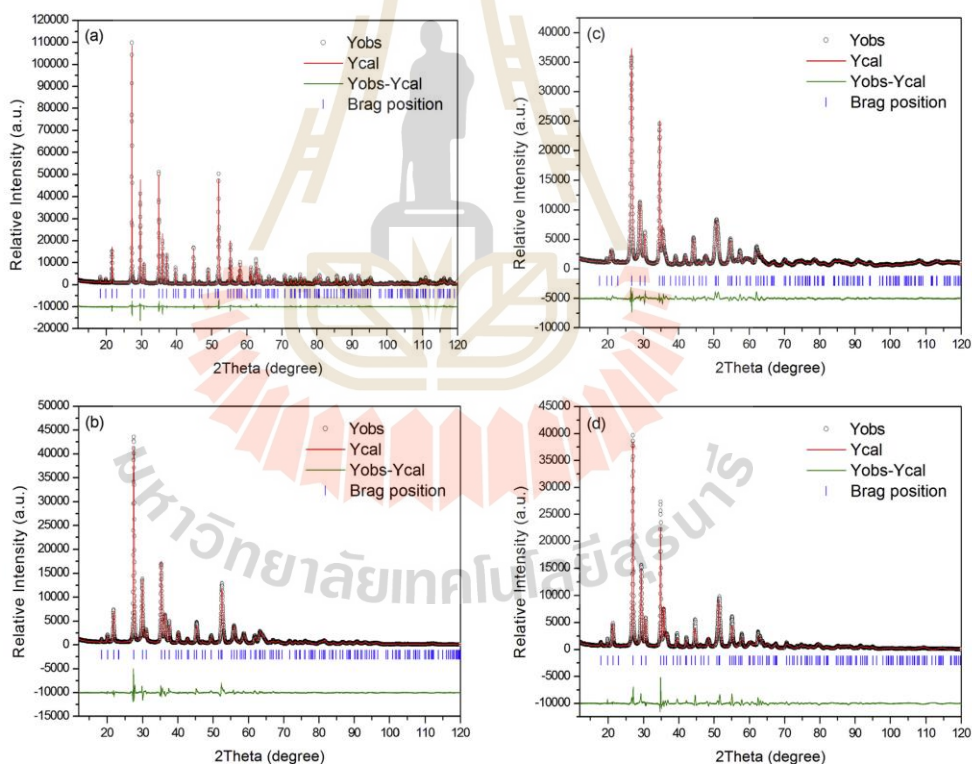
Fig. 5. Rietveld refinement plots of (a) In_2TeO_6, (b) $In_{1.60}Ga_{0.40}TeO_6$, (c) $In_{1.50}Bi_{0.50}TeO_6$, and (d) $In_{1.80}La_{0.20}TeO_6$.

Manuscript published in Journal of Alloys and Compounds

Only Sn and Tl have been reported to substitute In Refs. [16,17] in In_2TeO_6. In this work, In has been successfully substituted by Ga, Bi, and La. XRD diffraction patterns of entire series confirm the formation of solid solutions, as all diffractions can be indexed as In_2TeO_6 phase (PDF77-2044) (Fig. 2). Elemental compositions, obtained from EDS study, agree well with the nominal ones. The solubility limits of solid solutions $In_{2-x}M_xTeO_6$ with different M are different. $In_{2-x}Ga_xTeO_6$ (x = 0–0.40), $In_{2-x}Bi_xTeO_6$ (x = 0–0.50), and $In_{2-x}La_xTeO_6$ (x = 0–0.20) single phase can be obtained but the samples with higher x content contain some impurities. Therefore, the solubility limits of Ga, Bi, and La are 20%, 25%, and 10%, respectively. The incomplete solid solution is expected as Ga_2TeO_6, Bi_2TeO_6, and La_2TeO_6 are known to have different structures.

Cell parameters of the samples vary linearly with doping content, as shown in Fig. 3. Ga^{3+} (r = 0.62 Å) is smaller than In^{3+} (r = 0.80 Å) thus the cell parameters decrease when Ga content is increased. On the other hand, substituting Bi and La in In_2TeO_6 increase the cell parameters. La is well known to be La^{3+} (r = 1.032 Å) in oxides which is larger than In^{3+}. On the other hand, Bi can be in both +3 and + 5 state in oxides [12,24,25]. Nevertheless, the larger cell parameters in Bi-substituted samples suggest that it is in 3+ ($r_{Bi^{3+}}$ = 1.03 Å) rather than 5+ ($r_{Bi^{5+}}$ = 0.76 Å) in this case [26,27].

In additions, X-ray peak broadening is observed in all cases. In general, a peak broadening is a result of crystallite size or crystallite strain when instrumental error is ignored [28]. The broadening resulted from the first factor usually occurs with a crystallite size in nanoscale (<100 nm). In our cases, SEM images, as shown in Fig. 4, confirm that the particle size of the samples are large so that the broadening should come mostly from crystallite strain. While the crystal lattice can contain both homogeneous and inhomogeneous strain, the homogeneous strain only causes the peak position to shift without changing the peak profile. On the other hand, inhomogeneous or lattice strain is produced when atoms with very different sizes occupy the same site resulting in lattice plane distortion [29]. This lattice strain is reasonable in our samples as the difference in ionic size between each dopant and In^{3+} is greater than 20%. This effect becomes more obvious in heavily doped samples.

The refined parameters and crystallographic data are summarized in Tables 1 and 2, respectively. In addition, the examples of

Rietveld refinement plot are given in Fig. 5. In the refinement, the modified Thompson-Cox-Hastings pseudo-Voigt "TCHZ" peak type is utilized for Bi and La-doped samples, while PearsonVII peak type is used to refine the Ga-dopes series. Anisotropic refinement model is applied in lattice strain peak broadening but no preferred orientation is included. Although there are two distinct crystallographic sites for In in In_2TeO_6, both Bi and La prefer to occupy In1 site. Attempts to refine Bi and La in In1 and In2 sites simultaneously result in zero or slightly negative occupancies at In2 thus all Bi and La are fixed at In1 site. On the other hand, Ga occupancies are refined on both sites and the refined occupancies indicate that Ga is distributed in both In1 and In2. In all cases, the overall occupancies of substituting cations are fixed at the nominal values, which are confirmed based on the EDS technique. The equivalent isotropic thermal parameters, $B_{eq.}$, are fixed to the values obtained from crystallographic information file (CIF). Attempts to refine the thermal parameters result in negative values in some cases as the parameters are strongly correlated with each other [30].

Fig. 6. Schematic diagram of an M-O_6 octahedron for $In_{2-x}M_xTeO_6$ when M_x = $Ga_{0.40}$, $Bi_{0.50}$, and $La_{0.20}$.
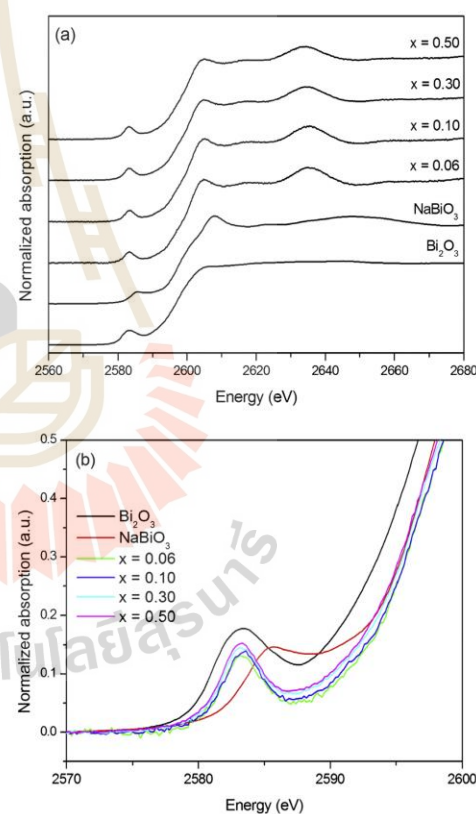
Fig. 7. (a) Normalized Bi M_5-edge XANES spectra of $In_{2-x}Bi_xTeO_6$ (x = 0.06, 0.10, 0.30, and 0.50) (b) Pre-edge region of Bi M_5-edge XANES spectra of $In_{2-x}Bi_xTeO_6$ (x = 0.06, 0.10, 0.30, and 0.50).

Manuscript published in Journal of Alloys and Compounds
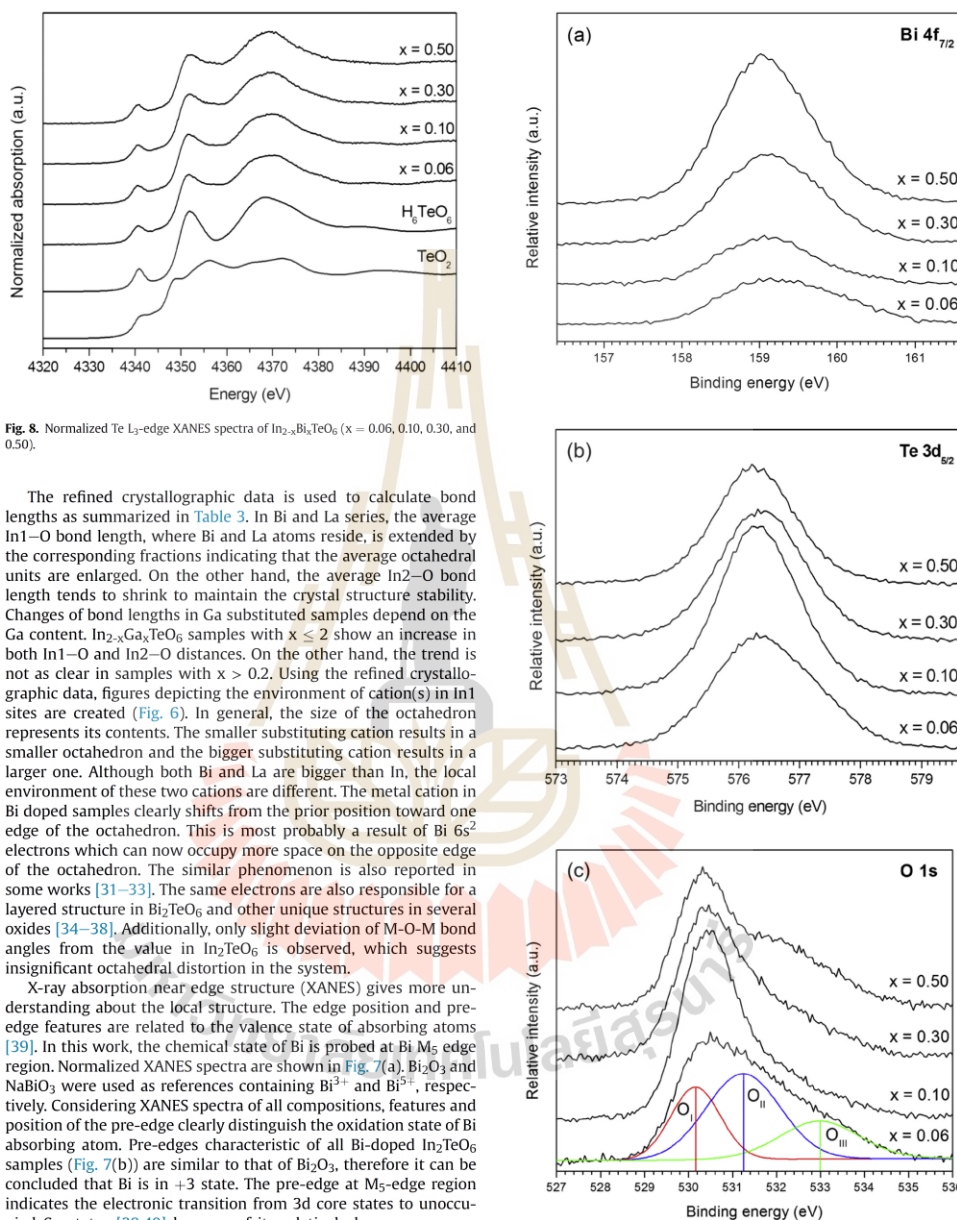
Fig. 8. Normalized Te L_3-edge XANES spectra of $In_{2-x}Bi_xTeO_6$ (x = 0.06, 0.10, 0.30, and 0.50).

The refined crystallographic data is used to calculate bond lengths as summarized in Table 3. In Bi and La series, the average In1−O bond length, where Bi and La atoms reside, is extended by the corresponding fractions indicating that the average octahedral units are enlarged. On the other hand, the average In2−O bond length tends to shrink to maintain the crystal structure stability. Changes of bond lengths in Ga substituted samples depend on the Ga content. $In_{2-x}Ga_xTeO_6$ samples with $x \leq 2$ show an increase in both In1−O and In2−O distances. On the other hand, the trend is not as clear in samples with x > 0.2. Using the refined crystallographic data, figures depicting the environment of cation(s) in In1 sites are created (Fig. 6). In general, the size of the octahedron represents its contents. The smaller substituting cation results in a smaller octahedron and the bigger substituting cation results in a larger one. Although both Bi and La are bigger than In, the local environment of these two cations are different. The metal cation in Bi doped samples clearly shifts from the prior position toward one edge of the octahedron. This is most probably a result of Bi $6s^2$ electrons which can now occupy more space on the opposite edge of the octahedron. The similar phenomenon is also reported in some works [31–33]. The same electrons are also responsible for a layered structure in Bi_2TeO_6 and other unique structures in several oxides [34–38]. Additionally, only slight deviation of M-O-M bond angles from the value in In_2TeO_6 is observed, which suggests insignificant octahedral distortion in the system.

X-ray absorption near edge structure (XANES) gives more understanding about the local structure. The edge position and pre-edge features are related to the valence state of absorbing atoms [39]. In this work, the chemical state of Bi is probed at Bi M_5 edge region. Normalized XANES spectra are shown in Fig. 7(a). Bi_2O_3 and $NaBiO_3$ were used as references containing Bi^{3+} and Bi^{5+}, respectively. Considering XANES spectra of all compositions, features and position of the pre-edge clearly distinguish the oxidation state of Bi absorbing atom. Pre-edges characteristic of all Bi-doped In_2TeO_6 samples (Fig. 7(b)) are similar to that of Bi_2O_3, therefore it can be concluded that Bi is in +3 state. The pre-edge at M_5-edge region indicates the electronic transition from 3d core states to unoccupied 6p states [39,40] because of its relatively low energy even though the transition to empty f states is also possible according to dipole selection rule [39]. As the energy levels of 6p states are close

Fig. 9. XPS spectra of (a) Bi $4f_{7/2}$, (b) Te $3d_{5/2}$, and (c) O $1s$ for $In_{2-x}Bi_xTeO_6$ series (x = 0.06, 0.10, 0.30, and 0.50).

Manuscript published in Journal of Alloys and Compounds
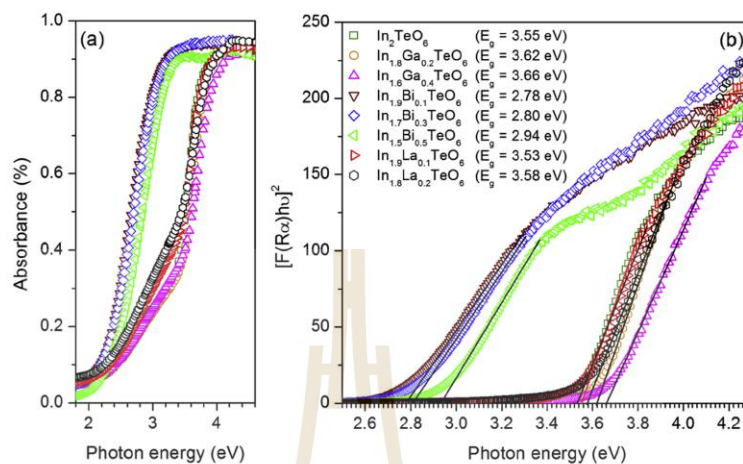
Fig. 10. (a) Absorbance UV–Visible spectra and (b) Kubelka-Munk plots of $In_{2-x}M_xTeO_6$ when M_x = $Ga_{0.2}$, $Ga_{0.4}$, $Bi_{0.1}$, $Bi_{0.3}$, $Bi_{0.5}$, $La_{0.1}$, $La_{0.2}$ according to direct allowed transition.
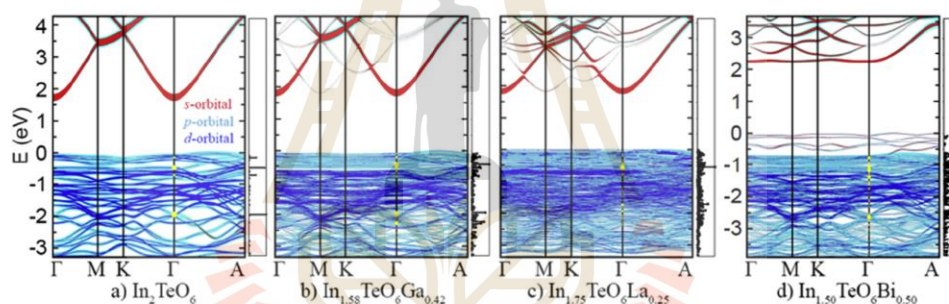
Fig. 11. The calculated orbital-projected electronic structures of In_2TeO_6, $In_{1.58}TeO_6Ga_{0.42}$, $In_{1.75}TeO_6La_{0.25}$, and $In_{1.5}TeO_6Bi_{0.5}$ along $\Gamma - M - K - \Gamma - A$ high symmetry directions. The s, p, and d-band characters are indicated by red (black), blue (grey), and dark blue (dark grey), respectively. The thickness of bands indicates the spectral weight. The spectrum of $|\langle\psi_c|\nabla|\psi_v\rangle|^2$ (see text) for all compounds is shown next to corresponding band structure plot and their magnitudes are given in arbitrary units. The transition strength contributed to prominent peaks is highlighted by yellow (white) dot on the band structure plot. (For interpretation of the references to colour in this figure legend, the reader is referred to the web version of this article.)

to that of 6s states, they have strong coupling which results in spin-orbit splittings and the hybridized sp states are generated and bonded with O 2p. This results in the multiple peaks of broad absorption above the edge energy [40]. In general, the intensity of the white line peaks is related to the symmetry. In this case, lower white line intensity is observed with increasing Bi content indicating a lowering of symmetry in the crystal [40]. Te valence state in Bi-doped In_2TeO_6 is determined at L_3-edge region. Fig. 8 illustrates normalized Te L_3-edge XANES spectra of all samples comparing to TeO_2 and $Te(OH)_6$ reference which contain Te^{4+} and Te^{6+}, respectively. Features of both pre-edge and edge energy of all samples indicate the presence of Te^{6+} [41]. The pre-edge and white line can be denoted to the transition from $2p_{3/2}$ to the empty 5s and from $2p_{3/2}$ to 5d, respectively [42]. The similar XANES spectra confirms the same local structure of Te in all samples.

X-ray photoelectron spectroscopy is utilized to confirm the oxidation state of all component cations in the compounds and

reflect their contents at the surface. The high-resolution XPS spectra of Bi $4f_{7/2}$, Te $3d_{5/2}$, and O 1s for $In_{2-x}Bi_xTeO_6$ series (x = 0.06, 0.10, 0.30, and 0.50) are shown in Fig. 9. The symmetric peaks of Bi $4f_{7/2}$ state were observed at 159.1–159.3 eV corresponding to Bi^{3+}–O bonds (Fig. 9(a)) [43,44]. The Bi $4f_{7/2}$ peak intensity also increases with the Bi content in the samples. The Te $3d_{5/2}$ peaks at 576.2–576.4 eV (Fig. 9(b)) are attributed to Te^{6+}–O bond [45–47]. The O 1s peak (Fig. 9(c)) can be deconvoluted into three main peaks using Gaussian-Lorentzian profile fitting and Shirley background subtraction. The first peak (O_I) at 530.2 eV corresponds to the lattice oxygen (O^{2-}) in the structure. The second peak (O_{II}) at 531.2 eV could be attributed to C–O bond due to the surface contamination. The third peak (O_{III}) at 533.0 eV can be assigned to surface adsorbed oxygen such as surface hydroxyls, and oxygen-contained organic species [48,49]. The oxidation states of all elemental components from XPS are consistent with XANES results.

Manuscript published in Journal of Alloys and Compounds

3.2. Optical properties and band structure calculation

The absorbance UV–Visible spectra are shown in Fig. 10(a). Based on the sharpness of absorption spectra, the samples may be divided into two groups. The first group includes Bi-doped samples exhibiting sharp absorption edge, while absorption edge of un-doped, Ga-doped, and La-doped samples clearly show two different slopes. To obtain band gap energy of the samples, Kubelka-Munk function, $F(R_\alpha)$, was applied. The relation is as follows: $F(R_\alpha) = (1-R_\alpha)^2/2R_\alpha$, where R is reflectance and $R_\alpha = R_{sample}/R_{reference}$. The plots of $[F(R_\alpha)h\upsilon]^{1/n}$ vs. $h\upsilon$ when $n = 1/2$ corresponding to direct allowed transition are shown in Fig. 10(b). Extrapolation on the highest slope onto the x axis (when $F(R_\alpha) = 0$) provides E_g.

The calculated electronic structures of In_2TeO_6, $In_{1.58}TeO_6Ga_{0.42}$, $In_{1.75}TeO_6La_{0.25}$, and $In_{1.5}TeO_6Bi_{0.5}$ are shown in Fig. 11. To compensate for the DFT underestimation, a rigid shift is applied to the conduction band to match the calculated optical band gap with the experimental observations [50]. The conduction band is shifted by 0.8 eV for In_2TeO_6, 0.9 eV for $In_{1.58}TeO_6Ga_{0.42}$ and $In_{1.5}TeO_6Bi_{0.5}$, and 0.6 eV for $In_{1.75}TeO_6La_{0.25}$. The band structure of In_2TeO_6 in Fig. 11(a) shows that valence bands are dominated by O 2p and In 4d characters while the conduction bands are mainly dominated by s-character of In 5s and O 2s. For Ga-doping (Fig. 11(b)), the character of conduction bands is barely changed and crystal symmetry is preserved. On the other hand, valence bands are much disturbed due to Ga d-characters although the intensity of main characters of valence bands still presented. For La, the valence bands are reasonably changed, while conduction bands are fairly changed due to La 6s electrons, as shown in Fig. 11(c). The parabolic dispersion of CBM at Γ is still observed. In the case of Bi-doping, band structure in Fig. 11(d) indicates much larger change due to incorporation of Bi into In site. The parabolic dispersion is lifted and s-bands of Bi 6s electrons are introduced into the previous In_2TeO_6 band gap.

Since the optical transition operator between two states is proportional to the momentum operator $(-i\hbar\nabla)$, the transition from valence state ψ_v to the conduction state ψ_c is obtained from $\langle\psi_c|\nabla|\psi_v\rangle$ [51]. The quantity of $|\langle\psi_c|\nabla|\psi_v\rangle|^2$ is calculated where ψ_c and ψ_v are restricted to the conduction band minimum (CBM) state and the valence band states at Γ, respectively. In all compounds, the top of valence band exhibits very little dispersion or nearly flat dispersion. The direct optical transitions at Γ from the valence band maximum (VBM) to the CBM are very low (Fig. 11), which can only make a very weak contribution to photon absorption under the influence of thermal vibrations. This indicates that this transition is forbidden. Similar forbidden transition from VBM and CBM is observed in several In containing oxides [50,52]. The strong transitions occur from valence bands, 2 eV below the VBM for undoped, Ga, and La-doped In_2TeO_6. The transition from VBM to CBM might be the origin of the less steep absorption at low energy region in UV–Vis spectra for these samples while the strong transitions from 2 eV below VBM is the origin of the steeper absorption edge at higher energy. Similar results are obtained for Bi-doped sample but the strong transition originates from 0.8 eV below VBM. However, VBM is mainly Bi 6s in character which have very weak or zero contribution to photon absorption as shown in the spectrum of transition strength. Therefore, there is only one sharp absorption observed in UV–Vis spectra of Bi-doped samples.

Photoluminescence (PL) spectra (Fig. 12) of all samples covers range of wavelengths varying from about 350 to 600 nm resulting in the white light emission. It is noted that the utilized excitation source of 255 nm (4.86 eV) has higher energy than the band gap energy of all samples ($E_g = 2.78$–3.66 eV). Similar to the UV–Vis spectra, PL spectra can be categorized into two groups. PL spectra of the un-doped In_2TeO_6, Ga-doped, and La-doped samples show two
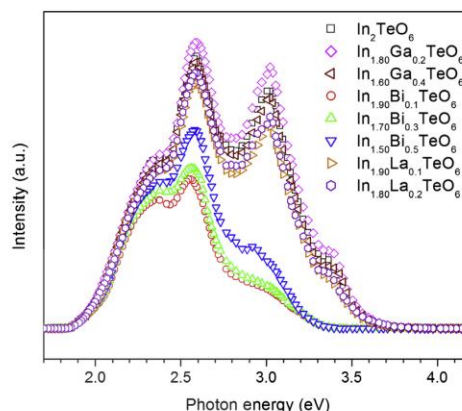

Fig. 12. Photoluminescence spectra of $In_{2-x}M_xTeO_6$ ($M_x = Ga_{0.2}$, $Ga_{0.4}$, $Bi_{0.1}$, $Bi_{0.3}$, $Bi_{0.5}$, $La_{0.1}$, $La_{0.2}$).

strong bands at 3.02 and 2.60 eV. The emission peak in UV region (~410 nm or ~3.02 eV) corresponds to near band edge transition, where the excited electrons go through non-radiative transitions from the bottom of conduction band to the sub-band or surface state first. Later, radiative transition of excited electrons in the said states to the valence band occurs, which leads to PL. The energy of this emission peaks is therefore slightly lower than the band gap energy [53,54]. The obtained results do not allow us to completely rule out the defect-originated luminescence. However, it is interesting to note that these samples were prepared under different conditions, which should have effects on type or concentration of the defect [53,55–58]. The fact that the strong luminescence peak at 2.60 eV is not significantly different from samples to samples led us to believe that this transition is either intrinsic or related to some deep defect levels. Possible mechanism includes the presence of the energy level within the band.

PL spectra of Bi-doped series show less number of peaks. As these samples have lower band gap energy, the absence of high energy peak is expected. Similar peaks at about 2.60 eV are observed in all Bi-doped samples, but they seem to be slightly broader. We believed that two mechanisms are related to this peak; the near band edge transition and, similar to the first group, the transition from an inter band to valence band. It should be noted that the peaks show a slight blue-shift when Bi content increases, which is consistent with the trend in band gap energy. The very broad shoulder is observed in PL spectra of all samples centering at ~2.95 eV. This could originate from the charge transfer of Te^{6+}–O. Similar observations are reported in many oxides containing d^{10} cations including In^{3+}, Ga^{3+}, Sb^{5+}, and Te^{6+} [59,60].

4. Conclusions

Ga, Bi, and La-doped In_2TeO_6 have been successfully synthesized with the general formula $In_{2-x}Ga_xTeO_6$ ($x = 0$, 0.20, 0.40), $In_{2-x}Bi_xTeO_6$ ($x = 0$, 0.10, 0.30, 0.50), and $In_{2-x}La_xTeO_6$ ($x = 0$, 0.10, 0.20). The chemical formula of $In_{2-x}M_x$ has been confirmed by EDS. The oxidation state of Bi and Te, confirmed by XANES and XPS, are +3 and +6, respectively. The linear relationship between the cell parameters and the composition leads us to conclude that the

Manuscript published in Journal of Alloys and Compounds

trivalent cations displace In. XRD peak broadening and SEM image imply the occurrence of internal lattice strain after cation substitution. Doping of Ga, Bi, and La cause the size of MO_6 octahedra to change corresponding to the ionic radius of dopants. Additionally, the appearance of stereochemically active lone-pair $6s^2$ electrons causes the shift of Bi^{3+} center within the octahedra. UV–Visible spectroscopy and the electronic structure calculation accompanying with the optical transition operator indicate that undoped-, Ga, Bi, and La-doped In_2TeO_6 possess direct allowed transition. In most samples, CB dominantly arises from In 5s and O 2s orbitals, while O 2p and In 4d orbitals mainly form VB. However, the interactions between Bi 6s states and O 2p states additionally influence the VB and CB of Bi doped samples. Photoluminescence property of In_2TeO_6-based samples is reported. All PL peaks are broadened over the visible region thus the samples luminate the visual white light. PL is most probably originated from the near band transition and the presence of the inter-band level.

Acknowledgements

References

[1] G. Bayer, Fortschr. Min. 46 (1969) 41–72.
[2] N. Berand, K.-J. Range, J. Alloy. Compd. 205 (1994) L3–L5.
[3] S. Ito, T. Murata, Y. Bito, Y. Togoguchi, Non-aqueous electrolyte secondary battery, US patent 6 124 057 (2000 Sept 26).
[4] J.A. Malone, J.F. Dorrian, O. Muller, R.E. Newnham, J. Am. Ceram. Soc. 52 (1969) 570–572.
[5] H.M. Kasper, Lincoln laboratory quarterly technical summary, M.I.T 3 (October 23 1969).
[6] P. Höss, T. Schleid, Z. Anorg. Allg. Chem. 633 (2007) 1391–1396.
[7] R. Pankajavalli, A. Jain, A. Sharma, S. Anthonysamy, V. Ganesan, J. Therm. Anal. Calorim. 112 (2013) 83–93.
[8] J. Llanosa, R. Castillo, D. Barrionuevo, D. Espinoza, S. Conejeros, J. Alloy. Compd. 485 (2009) 565–568.
[9] F. Bernard, P. Rose, M. Daniele, Mater. Res. Bull. 10 (1975) 1305.
[10] S. Natansohn, J. Inorg. Nucl. Chem. 30 (1968) 741.
[11] M. Tröemel, F.W. Huetzler, H.G. Burckhardt, C. Platte, E. Muench, Z. Anorg. Allg. Chem. 551 (1987) 95.
[12] M. Udovic, M. Valant, D. Suvorov, J. Eur. Ceram. Soc. 24 (2004) 953–958.
[13] M.J. Redman, W.P. Binnie, W.J. Mallio, J. Less Common Met. 23 (1971) 313–315.
[14] B. Frit, Cr. Acad. Sci. Chim. 281 (1975) 769–772.
[15] R.D. Shannon, J.L. Gillson, R.J. Bouchard, J. Phys. Chem. Solids 38 (1977) 877–881.
[16] B. Shemirani, F.P. Koffyberg, Mater. Res. Bull. 27 (1992) 693–698.
[17] T. Siritanon, A.W. Sleight, M.A. Subramanian, J. Solid State Chem. 84 (2011) 877–880.
[18] G. Hautier, A. Miglio, D. Waroquiers, G.-M. Rignanese, X. Gonze, Chem. Mater. 26 (2014) 5447–5458.
[19] G. Kresse, J. Furthmüller, Comp. Mater. Sci. 6 (1996) 15–50.
[20] J.P. Perdew, K. Burke, M. Ernzerhof, Phys. Rev. Lett. 77 (1996) 3865–3868.
[21] P.E. Blöchl, Phys. Rev. B 50 (1994) 17953–17979.
[22] G. Kresse, D. Joubert, Phys. Rev. B 59 (1999) 1758–1775.
[23] M. Tomić, H.O. Jeschke, R. Valentí, Phys. Rev. B 90 (2014) 195121.
[24] A.V. Egorysheva, O.G. Ellert, Y.V. Zubavichus, O.M. Gajtko, N.N. Efimov, R.D. Svetogorov, V. Yu Murzin, J. Solid State Chem. 225 (2015) 97–104.
[25] Y. Fujimoto, J. Am. Ceram. Soc. 93 (2010) 581–589.
[26] R.D. Shannon, C.T. Prewitt, , Acta Crystallogr. B 25 (1969) 925–946.
[27] R.D. Shannon, Acta Crystallogr. A 32 (1976) 751–767.
[28] B.S. Murty, P. Shankar, B. Raj, B.B. Rath, J. Murday, Textbook of Nanoscience and Nanotechnology, first ed., Springer-Verlag Berlin and Heidelberg GmbH & Co. KG, Berlin, Germany, 2013.
[29] J. Li, T. Siritanon, J.K. Stalick, A.W. Sleight, M.A. Subramanian, Inorg. Chem. 50 (2011) 5747–5754.
[30] K. Ozawaa, M. Eguchib, H. Nakamuraa, Y. Sakka, Solid State Ionics 172 (2004) 109–112.
[31] M. Retuerto, A. Muñoz, M.J. Martínez-Lope, M. Garcia-Hernandez, G. André, K. Krezhov, J.A. Alonso, J. Phys. Condens. Matter. 25 (2013) 216002.
[32] A. Singh, C. Moriyoshi, Y. Kuroiwa, D. Pandey, Phys. Rev. B 85 (2012) 064116.
[33] J.-H. Park, P.M. Woodward, Int. J. Inorg. Mater. 2 (2000) 153–166.
[34] Z.X. Cheng, T.M. Silver, A.H. Li, X.L. Wang, H. Kimura, J. Magn. Magn. Mater. 283 (2004) 143–149.
[35] J.L. García-Munoz, C. Frontera, M.A.G. Aranda, C. Ritter, A. Llobet, M. Respaud, M. Goiran, H. Rakoto, O. Masson, J. Vanacken, J.M. Broto, J. Solid State Chem. 171 (2003) 84–89.
[36] M. Hervieu, Ph. Boullay, C. Michel, A. Maignan, B. Raveau, J. Solid State Chem. 142 (1999) 305–318.
[37] G. Lalitha, P.V. Reddy, J. Alloy. Compd. 494 (2010) 476–482.
[38] R. Seshadri, N.A. Hill, Chem. Mater. 13 (2001) 2892–2899.
[39] G. Berghöfer, D. Reinen, Mod. Phys. Lett. B 7 (1993) 1133–1140.
[40] O.M. Ozkendir, M.S. Bozgeyik, Eur. Phys. J. B 76 (2010) 203–208.
[41] H. Singh, A.K. Sinha, H. Ghosh, M.N. Singh, P. Rajput, C.L. Prajapat, M.R. Singh, G. Ravikumar, J. Appl. Phys. 116 (2014) 074904.
[42] A. Ibanez, T. Ericsson, O. Lindqvist, D. Bazin, E. Philippot, J. Mater. Chem. 4 (1994) 1101–1106.
[43] J. Di, J. Xia, M. Ji, H. Li, H. Xu, H. Li, R. Chen, Nanoscale 7 (2015) 11433–11443.
[44] K.H. Reddy, S. Martha, K.M. Parida, RSC Adv. 2 (2012) 9423–9436.
[45] J.F. Moulder, W.F. Stickle, P.E. Sobol, K.D. Bomben, Handbook of X-ray Photoelectron Spectroscopy, second ed., Perkin-Elmer Corp, Eden Prairie, Minnesota, 1992.
[46] J. Holmberg, S. Hansen, R.K. Grasselli, A. Andersson, Top. Catal. 38 (2006) 17–29.
[47] J.M.M. Millet, H. Roussel, A. Pigamo, J.L. Dubois, J.C. Jumas, Appl. Catal. A-Gen. 232 (2002) 77–92.
[48] L. He, Z. Wu, Z. Li, J. Ju, Q. Ou, R. Liang, J. Phys. D. Appl. Phys. 46 (2013) 175306.
[49] W. Song, S.K. So, L. Cao, Appl. Phys. A 72 (2001) 361–365.
[50] A. Walsh, J.L.F. Da Silva, S.-H. Wei, C. Körber, A. Klein, L.F.J. Piper, A. DeMasi, K.E. Smith, G. Panaccione, P. Torelli, D.J. Payne, A. Bourlange, R.G. Egdell, Phys. Rev. Lett. 100 (2008) 167402.
[51] M. Gajdoš, K. Hummer, G. Kresse, J. Furthmüller, F. Bechstedt, Phys. Rev. B 73 (2006) 045112.
[52] F.P. Koffyberg, F.A. Benko, Appl. Phys. Lett. 37 (1980) 320–322.
[53] J. Liqiang, Q. Yichun, W. Baiqi, L. Shudan, J. Baojiang, Y. Libin, F. Wei, F. Honggang, S. Jiazhong, Sol. Energy Mat. Sol. C 90 (2006) 1773–1787.
[54] J. Zhang, X. Chen, Y. Shen, Y. Li, Z. Hu, J. Chu, Phys. Chem. Chem. Phys. 13 (2011) 13096–13105.
[55] S.A. Studenikin, N. Golego, M. Cocivera, J. Appl. Phys. 84 (1998) 2287–2294.
[56] D. Li, Y.H. Leung, A.B. Djurisic, Z.T. Liu, M.H. Xie, S.L. Shi, S.J. Xu, W.K. Chan, Appl. Phys. Lett. 85 (2004) 1601–1603.
[57] C.H. Ahn, Y.Y. Kim, D.C. Kim, S.K. Mohanta, H.K. Cho, J. Appl. Phys. 105 (2009) 013502.
[58] K.N. Shinde, S.J. Dhoble, K. Park, Nano-Micro Lett. 4 (2012) 78–82.
[59] G. Blasse, Chem. Phys. Lett. 175 (1990) 237–241.
[60] J.J.M. De Bruin, M. Wiegel, G.J. Dirksen, G. Blasse, J. Solid State Chem. 107 (1993) 397–400.

Manuscript published in Journal of Alloys and Compounds

Electrical properties of $(Cs_{1-x}A_x)Al_{0.33}Te_{1.67}O_6$ (A = K and Rb) mixed valence pyrochlores

Anurak Waehayee[a], Tanachat Eknapakul[b], Narong Chanlek[c], Thanundon Kongnok[b], Surachet Rattanasuporn[c], Hideki Nakajima[c], Worawat Meevasana[b,d,e], Theeranun Siritanon[a,d,e]∗

[a]School of Chemistry, Institute of Science, Suranaree University of Technology, Nakhon Ratchasima 30000, Thailand

[b]School of Physics, Institute of Science, Suranaree University of Technology, Nakhon Ratchasima 30000, Thailand

[c]Synchrotron Light Research Institute, Nakhon Ratchasima 30000, Thailand

[d]NANOTEC-SUT Center of Excellence on Advanced Functional Nanomaterials, Suranaree University of Technology

[e]Center of Excellence-Advanced Functional Materials, Suranaree University of Technology

Abstracts

The preparation and electronic properties of $Cs_{1-x}A_xAl_{0.33}Te_{1.67}O_6$ (A = K, Rb, and Cs) are reported. Replacing Cs with smaller Rb and K reduces cell parameters of the compounds but does not affect the overall structure. Electronic conductivities of all samples were measured and explained based on the band conduction model. Although XPS Te3d$_{5/2}$ spectra indicate that all samples contain similar amount of Te^{4+}/Te^{6+} mixed valency, their conductivities are varied from about 0.1 S·cm in $CsAl_{0.33}Te_{1.67}O_6$ to 3×10^{-5} S·cm in $RbAl_{0.33}Te_{1.67}O_6$ and 3×10^{-7} S·cm in $KAl_{0.33}Te_{1.67}O_6$ at 300 K. To explain such large differences, the band structure diagrams are proposed based on the UV-Vis spectra and XPS spectra at valence band region. When the obtained activation energies of conduction and the proposed band diagram are considered, it is concluded that $AAl_{0.33}Te_{1.67}O_6$ (A = K, Rb, and Cs) are n-type semiconductors. The defect levels in these samples originate from Te^{4+} whose energy level relative to the conduction band minimum is different from samples to samples. Such differences are affected by Cs content in the structure as Cs seems to lower the band gap energy and increase the valence band maximum. It is the position of these defect levels that determines the electronic conductivity of the compounds.

Manuscript published in Journal of Alloys and Compounds

Keywords: Oxide; Mixed valence compounds; Electrical properties; X-ray Photoelectron Spectroscopy

Introduction

Post transition elements form oxides with interesting structures and properties. Several oxides containing heavy post-transition elements are known to have good electronic conductivity due to the presence of diffused s orbitals which results in wide conduction bands and low carrier mobility [1]. Some well-known examples include In_2O_3, $ZnSnO_3$, and $In_4Sn_3O_{12}$ [2-4]. However, conducting tellurium oxides are very rare. To our knowledge, the only clear examples are series of defect pyrochlores with general formula $Cs(M,Te)_2O_6$; M = 2+, 3+ and 4+ cations which show n-type semiconducting behavior due to Te^{4+}/Te^{6+} mixed valency [5].

It has been established that M cations in the mentioned formula play some roles in determining the electronic conductivities of the compounds. Smaller M cations reduce the cell parameter which compresses Te^{4+} in the structure and consequently destabilizes it. In addition, suitable M cations could provide orbitals with appropriate energy to overlap with Te 5s which could give rise to samples with higher conductivity. Only one compound in the series, $Cs(Al,Te)_2O_6$, was extensively investigated through detailed structural studies where it was concluded that Te^{4+}/Te^{6+} mixed valency in the compounds is a result of small deviations from stoichiometry [6]. However, the role of Cs in the structure remains unclear. Thus, the objectives of this work are to deepen the understanding of these series of oxides and to study the effects of cations at Cs position on the electronic properties of compounds in $Cs_{1-x}A_xAl_{0.33}Te_{1.67}O_6$; A = Rb and K series.

Experimental Section

All samples were prepared by solid state reaction. The reactants were $CsNO_3$ (Sigma-Aldrich, 99+%), $RbNO_3$ (Acros organic, 99.8%), Al_2O_3 (Acros organic, 99+ %, for Rb-doped series), $Al(OH)_3$ (Acros organic, 99.9%, for K-doped series) and TeO_2 (Acros organic, 99+%). Stoichiometric mixtures of the reactants were weighed and ground in an agate mortar and heated to 500°C for 5 h. After that, the samples were reground and sintered at 625 ^{o}C for 12 h in air. Powder X-ray diffraction (XRD) patterns were recorded by a Bruker D2 Phaser diffractometer (Cu Kα radiation, λ = 1.5406 Å) for phase identification. The X-ray Photoelectron Spectra (XPS) of Cs 3d, Rb 3d, K 2p, Al 1s, O 1s, Te $3d_{5/2}$ and valence band (VB) were recorded by a PHI5000 VersaProbe II XPS instruments (ULVAC-PHI, Japan)

Manuscript published in Journal of Alloys and Compounds

(Monochromatic X-ray of Al K_α ,1486.6 eV) at SUT-NANOTEC-SLRI joint research facility, Synchrotron Light Research Institute (SLRI), Thailand. The binding energies drift due to charging effects were corrected using the position of the C1s as a reference at 284.8 eV [7, 8]. Agilent UV-Vis-NIR spectrophotometer modeled Carry 5000 was used for optical diffuse reflectance spectroscopy (DRS). The diffuse reflectance (%R) spectra were recorded in the wavelength range of 200-2000 nm with the double beam mode. Band gap energy was obtained by extrapolation of the plot of $(K\nu)^{1/2}$ versus photon energy (ν), where K is reflectance transformed according to Kubelka–Munk function [$K = (1 - R)^2/2(R)$]. In this function, $R = (\%R_{sample}/\%R_{standard})$ [9, 10]. The electrical conductivities of all sintered samples were measured from 300 to 673 K by four-probe method using a Keysight B2901A source/measure unit.

Calculations

The density of states (DOS) were calculated based on density functional theory (DFT) using the Vienna *ab initio* simulation package (VASP) [11, 12] employing the Perdew, Burke, Ernzerhof (PBE) exchange-correlation function [13] implemented with the projector augmented-wave method (PAW) [14, 15]. Γ-centered 3×3×2 Monkhorst-Pack k-mesh was used for the Brillouin zone integrations. The cutoff energy for plane-wave basis sets was set at 520 eV. Structural relaxation was performed until the force on each ion is less than 0.01 eV/Å.

Results and discussions

Structure

Powder X-ray diffraction patterns indicate that all samples are single phase (Fig. 1). All diffractions can be indexed as AB_2O_6 defect cubic pyrochlore structure (β-pyrochlore) with $Fd\bar{3}m$ space group [16]. The defect pyrochlore structure can be explained based on the interpenetrating network of $(Al,Te)_2O_6$ corner sharing octahedral units with A cations (Cs, Rb, and K) occupying the interstitial sites. Comparing to $A_2B_2O_7$ pyrochlore, defect pyrochlore structure has lots of vacancies. In addition, there are few possible crystallographic sites for A cations. The XRD patterns in this work suggest no indication of them being at positions other than the normal 8b but small deviation from this ideal position, like the 32e position, is possible.

Manuscript published in Journal of Alloys and Compounds
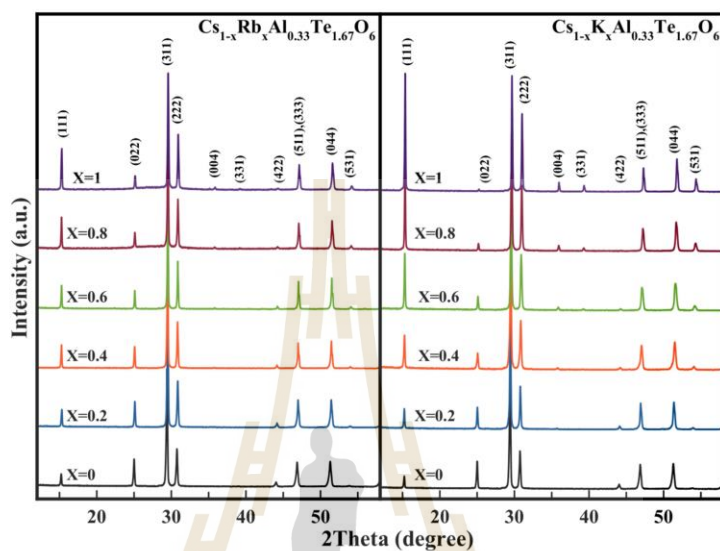
Fig. 1 XRD patterns of $Cs_{1-x}Rb_xAl_{0.33}Te_{1.67}O_6$ and $Cs_{1-x}K_xAl_{0.33}Te_{1.67}O_6$

It is worth to note that the displacive disorder of A cation from 8b to 32e position results in a nonlinear increase of cell parameters in $AAl_{0.33}W_{1.67}O_6$; A = Cs, Rb, and K [17]. However, such anomaly is not observed in this work although the samples are quite similar. Plots of calculated cell parameters versus substituting contents are linear in both series (Fig. 2). As both K^+ (1.51 Å) and Rb^+ (1.61 Å) are smaller than Cs^+ (1.74 Å), increasing their contents results in smaller cell parameters as expected [18, 19]. However, the main network of the structure is the B_2O_6 octahedral network, changing A cations has a much smaller effect on the cell parameters comparing to changing the B cations. Similar results were reported by Castro and Rasines [20].

XPS results

XPS survey spectra of $CsAl_{0.33}Te_{1.67}O_6$ (CATO), $RbAl_{0.33}Te_{1.67}O_6$ (RATO), and $KAl_{0.33}Te_{1.67}O_6$ (KATO) show the corresponding elemental compositions in each compound (Fig. 3). Cs 3d, Rb 3d and K 2p XPS spectra in Fig. 4 give semi-quantitative results on the composition of the prepared samples. The obtained binding energies are close to those

Manuscript published in Journal of Alloys and Compounds

reported in the literature [21-24]. Peak areas of each element in the samples are proportional to the nominal composition.
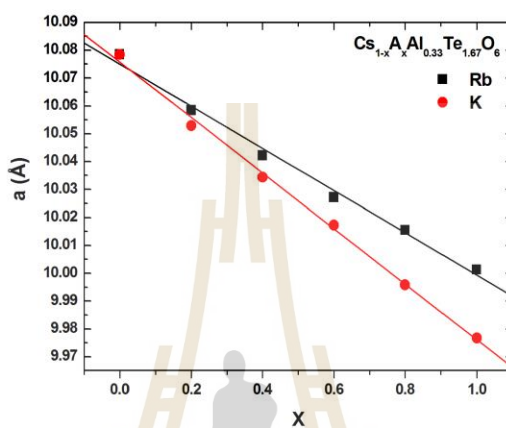
Fig. 2 Plots of cell parameters versus Rb and K content

Manuscript published in Journal of Alloys and Compounds
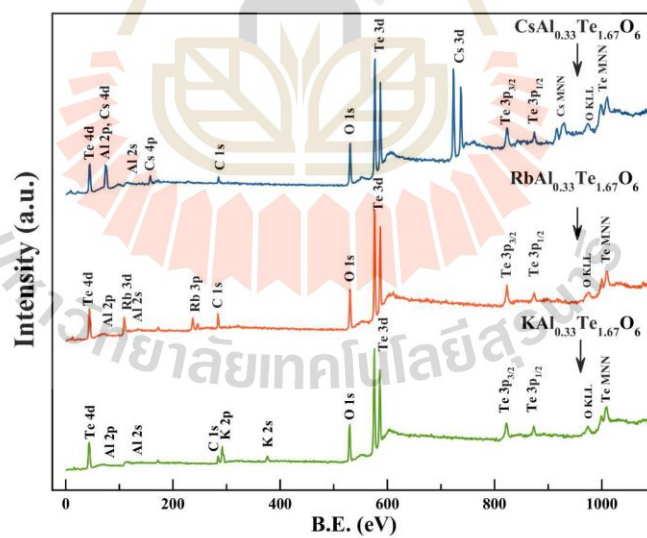
Fig. 3 XPS survey spectra of $CsAl_{0.33}Te_{1.67}O_6$, $RbAl_{0.33}Te_{1.67}O_6$, and $KAl_{0.33}Te_{1.67}O_6$
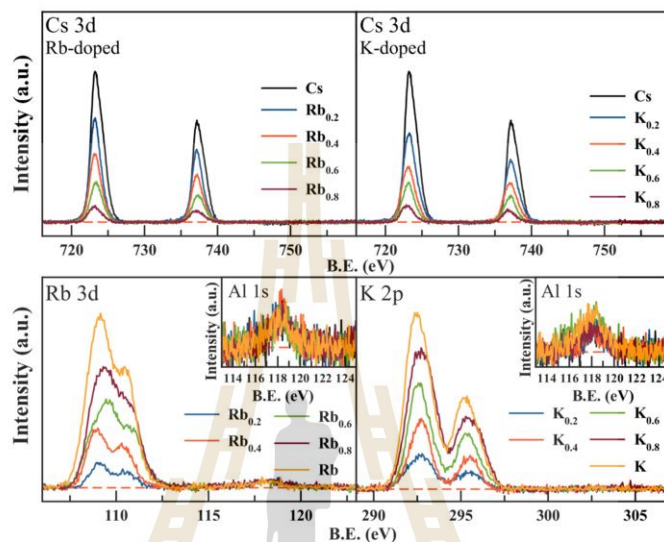
Fig. 4 Cs 3d, Rb 3d, K 2p and Al 1s XPS spectra of $Cs_{1-x}Rb_xAl_{0.33}Te_{1.67}O_6$ and $Cs_{1-x}K_xAl_{0.33}Te_{1.67}O_6$

XPS spectra of Te $3d_{5/2}$ were also examined to probe oxidation states of Te in the samples. As seen in Fig. 5, all spectra show small asymmetry with a tail on the lower energy region. These spectra were fitted using two Gaussian-Lorentzian peaks; one represents Te^{4+} at lower binding energy and the other represents Te^{6+}. For comparison, Te$3d_{5/2}$ spectra of $CsTe_2O_6$ (CTO), a known compound which contains both Te^{4+} and Te^{6+}, are also shown and fitted with the same method here. The binding energy and peak area of each peak are summarized in Table 1. It is interesting to note that while the binding energies of the observed Te^{6+} are close to the reported values, those of Te^{4+} in $Cs_{1-x}A_xAl_{0.33}Te_{1.67}O_6$ (A = K, Rb, and Cs) are slightly smaller than most reported values for Te^{4+} [25, 26]. On the other hand, the obtained values are too high to be assigned to Te(0) or Te^{2-} states [27]. As chemical environments affect the binding energy, the binding energy of Te^{4+} in these samples which is in the unique compressed octahedra is expected to be different from that of Te^{4+} in TeO_2 standard. In fact, our values are close to that reported in $Gd_2(Ti_{2-y}Te_y)O_7$ pyrochlores [28].

Manuscript published in Journal of Alloys and Compounds
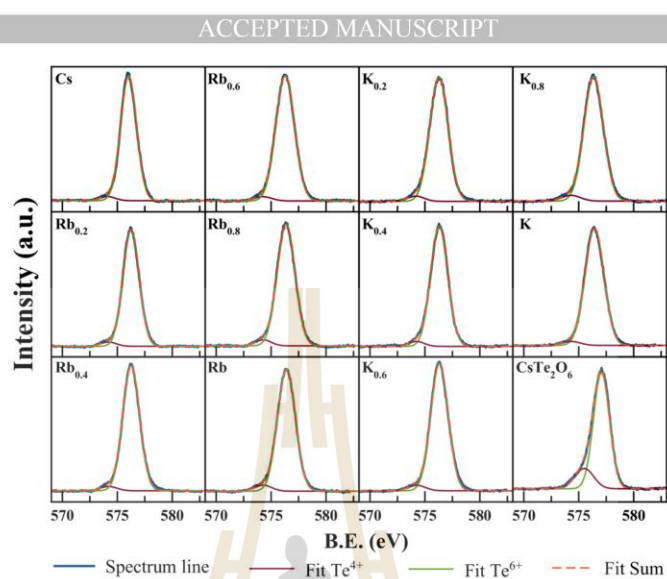
Fig. 5: XPS Te $3d_{5/2}$ spectra of the samples

It is difficult to quantitatively conclude the amount of Te^{4+} in the samples based solely on the peak areas. Nevertheless, the existence of Te^{4+} is obvious and its amount in the cubic pyrochlore samples is very low. The presence of small amount of Te^{4+} is a result of small deviation in stoichiometry as reported by Li et al.[6] who concluded that the composition of the prepared $CsAl_{0.33}Te_{1.67}O_6$ was actually $CsAl_{0.30}Te_{1.70}O_6$. A small amount of Te^{6+} must then be reduced to Te^{4+} to maintain charge neutrality. Te $3d_{5/2}$ XPS results reported here reveal the existence of Te^{4+} in all samples with similar peak areas suggesting that the Rb and K substituted samples contain similar defects with a similar amount.

Manuscript published in Journal of Alloys and Compounds

Table 1: Te $3d_{5/2}$ fitting results

Comp. (X)	Te^{6+}		Te^{4+}		Ratio of Te^{6+}: Te^{4+} (1.67)	R^2
	B.E. (eV)	FWHM (eV)	B.E. (eV)	FWHM (eV)		
0	576.03	1.70	574.12	1.62	1.62:0.05	0.9983
Rb-doped						
0.2	576.25	1.72	574.19	1.68	1.61:0.06	0.9991
0.4	576.27	1.79	574.22	1.78	1.62:0.05	0.9987
0.6	576.28	2.00	574.25	1.86	1.62:0.05	0.9994
0.8	576.36	1.90	574.28	1.68	1.60:0.07	0.9992
1.0	576.40	1.85	574.28	1.80	1.60:0.07	0.9995
K-doped						
0.2	576.28	1.89	574.29	1.68	1.61:0.06	0.9993
0.4	576.32	1.79	574.33	1.72	1.60:0.07	0.9995
0.6	576.32	1.84	574.34	1.61	1.60:0.07	0.9982
0.8	576.35	2.02	574.43	1.99	1.60:0.07	0.9987
1.0	576.42	1.97	574.46	1.87	1.61:0.06	0.9992
CsTe$_2$O$_6$						
-	577.07	1.72	575.50	2.00	1.66:0.44 (Te$^{6+}_{1.5}$: Te$^{4+}_{0.5}$)	0.9981

Manuscript published in Journal of Alloys and Compounds

XPS spectra at valence band region (Fig. 6a) give useful information regarding the electronic structure of the samples. Like most oxides, the top of the valence band is predominantly O 2p. The outstanding feature of the spectra is the position of alkali p orbitals which is at about 10, 13, and 17 eV for Cs 5p, Rb 4p, and K 3p, respectively. The positions of these states are similar to values in other reports [24, 29, 30]. Rb 4p and K 3p bands are quite separated from O 2p near the top of the valence band and should not have much contribution in it. Thus, the spectral feature and position of the valence band in Rb and K containing samples are very similar. This also implies that any effects from the difference in bond distances and angles are insignificant. Two samples containing Cs have similar spectra although there are some differences as both samples contain quite a different composition and have related, but different, crystal structure. As Cs 5p bands are clearly overlapping with O2p, Cs is believed to contribute to the valence band. The overlapping between Cs 5p and O 2p in the valence band is observed in many oxides [31, 32]. The contribution from Cs 5p broadens the valence band thus causes the shift in its position comparing to the other two samples with no Cs. In addition, the spectral shape of CTO valence band is different from others. Besides the dominant peaks contributed by O 2p, there is another small peak on top of the valence band maximum (VBM) (Fig. 6b).

To gain deeper understandings, band structure calculation was performed for CTO. The valence band of CTO may be divided into three regions (Fig. 6c). The small peaks at VBM consist of O 2p and Te 5s orbitals. The wide region at approximately -1 to -6 eV is predominantly O 2p with a small contribution from Te 4d orbital and the sharp peak at about -6 to -8 eV is formed mainly by Cs 5p orbital with some contribution from Te 5p. These main features of the valence band are qualitatively comparable to the obtained XPS spectra. It is interesting to note that the small peak at VBM is not observed in XPS spectra of the $AAl_{0.33}Te_{1.67}O_6$ series. However, as proposed by Li et al. [6] and deduced from Te $3d_{5/2}$ spectra, $AAl_{0.33}Te_{1.67}O_6$ samples should contain only about 3% of Te^{4+} which is very little comparing to 25% in CTO. Besides, it is difficult to compare the spectra of these two series as they have a different structure which leads to the different position of Te 5s.

Manuscript published in Journal of Alloys and Compounds
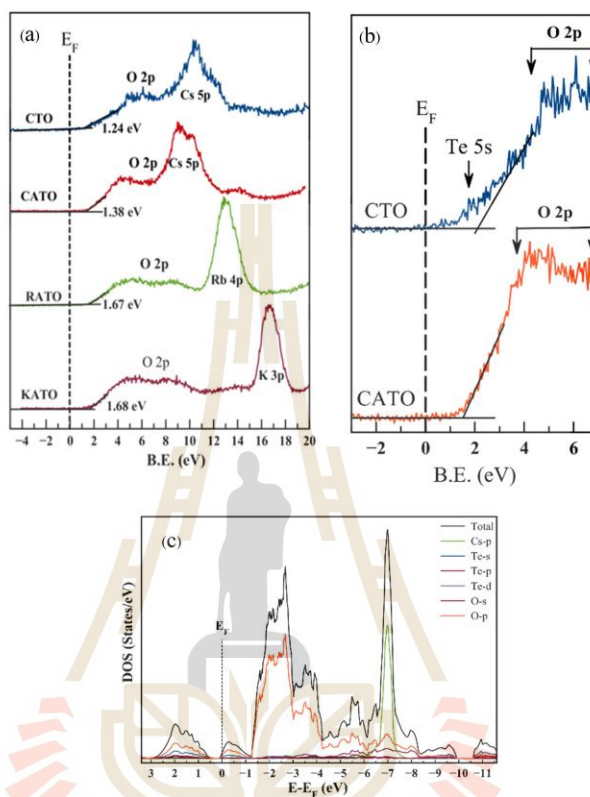
Fig. 6 XPS valence band spectra of $CsTe_2O_6$ and $AAl_{0.33}Te_{1.67}O_6$ (A = Cs, Rb, and K) (a) and the close-up of Cs containing samples showing an additional small peak near the Fermi level (b). (c) shows the calculated valence band of $CsTe_2O_6$.

Electrical properties

Electronic conductivities of $Cs_{1-x}A_xAl_{0.33}Te_{1.67}O_6$, A = Rb and K decrease with increasing A content. The effect is very significant as room temperature conductivity of $KAl_{0.33}Te_{1.67}O_6$ and $RbAl_{0.33}Te_{1.67}O_6$ are 10^3 and 10^5 times lower than that of $CsAl_{0.33}Te_{1.67}O_6$, respectively (Fig. 7). The conductivities of all samples are plotted based on Arrhenius' equation: $\sigma = Ae^{(-Ea/kT)}$ where A is pre-exponential constant, k is Boltzmann constant, Ea is activation energy, and T is absolute temperature (Fig. 7) and the activation

Manuscript published in Journal of Alloys and Compounds

energies are calculated and summarized in Table 2. It is obvious that the lower Cs content, the higher the activation energy. Interestingly, Siritanon et. al. [5] previously reported that the Arrhenius plot of $Cs(M,Te)_2O_6$ are not linear in the temperature range 50-300 K and concluded that the samples exhibit variable range hopping conduction as the plots of log conductivity vs. $1/T^{1/4}$ are linear. Therefore, the samples have different conduction mechanisms at different temperatures. In fact, crossover from variable range hopping conduction to thermally activated band conduction from low to high temperatures have been reported in many systems and believed to also be the case here [33, 34].
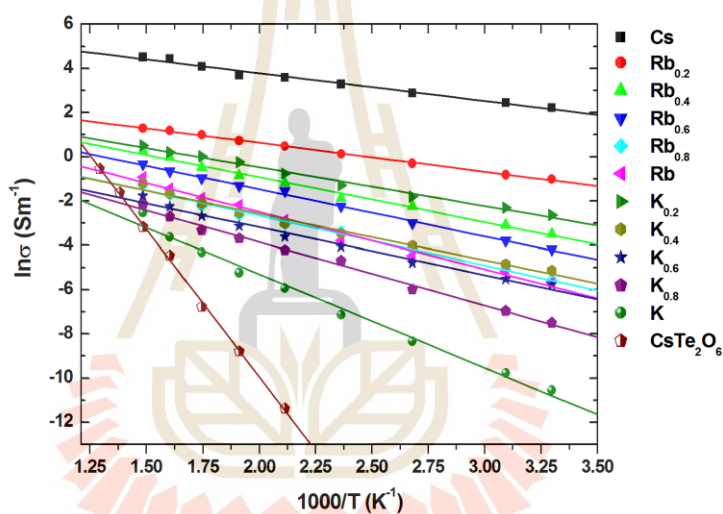
Fig. 7 Electronic conductivities of $Cs_{1-x}A_xAl_{0.33}Te_{1.67}O_6$ (A = Rb and K) and $CsTe_2O_6$ samples fitted with Arrhenius equation.

Manuscript published in Journal of Alloys and Compounds

Table 2: Activation energy and R^2 obtained from fitting the electronic conductivities of $Cs_{1-x}A_xAl_{0.33}Te_{1.67}O_6$; A = Rb and K and $CsTe_2O_6$ with Arrhenius equation.

x	E_a (eV)	R^2	x	E_a (eV)	R^2
0	0.108	0.9854	$CsTe_2O_6$	1.15	0.9987
Rb-doped			**K-doped**		
0.2	0.113	0.9985	0.2	0.151	0.9914
0.4	0.174	0.9921	0.4	0.180	0.9856
0.6	0.183	0.9972	0.6	0.186	0.9855
0.8	0.194	0.9919	0.8	0.247	0.9934
1.0	0.224	0.9870	1.0	0.364	0.9888

Optical property

The UV-Vis absorption spectra of $CsTe_2O_6$ and $AAl_{0.33}Te_{1.67}O_6$, A = Cs, Rb, and K are shown in Fig. 8a and the band gap energies obtained from the extrapolations (Fig. 8b) are summarized in Fig. 9. Although most oxides containing Cs and Te have large band gap and white color, the band gap of $CsTe_2O_6$ is only about 1.4 eV and the compound is dark brown. The unusually small band gap is a result of Te^{4+}, Te^{6+} intervalence charge transfer (IVCT) which gives rise to the absorption in a visible region corresponding to the transition from Te^{4+} $5s^2$ to Te^{6+} $5s^0$. Although there are very few reports on Te^{4+}/Te^{6+} charge transfer, a similar mechanism is widely studied in other mixed valence systems including those with post-transition cations like Sb, Sn, Tl [35, 36].

UV-Vis spectra of $AAl_{0.33}Te_{1.67}O_6$ series are obviously different from that of $CsTe_2O_6$ although the compounds also containTe^{4+}/Te^{6+} mixed valency. However, Te^{4+} and Te^{6+} in $CsTe_2O_6$ are in different crystallographic sites while those in $AAl_{0.33}Te_{1.67}O_6$ are in the same one. As λ_{max} of absorption should be directly related to the energy difference between Te^{4+} $5s^2$ and Te^{6+} $5s^0$, the similar environment around Te^{4+} and Te^{6+} in $AAl_{0.33}Te_{1.67}O_6$ results in absorptions at longer wavelengths. Therefore, it is concluded here that the very broad and

Manuscript published in Journal of Alloys and Compounds

strong absorption centering at long wavelengths is associated with IVCT of Te^{4+} and Te^{6+}. Mizoguchi et al. [35] also reported similar diffuse reflectance spectra of $BaSn_{1-x}Sb_xO_3$ which contain mixed valence ions and show a very broad absorption band due to IVCT.
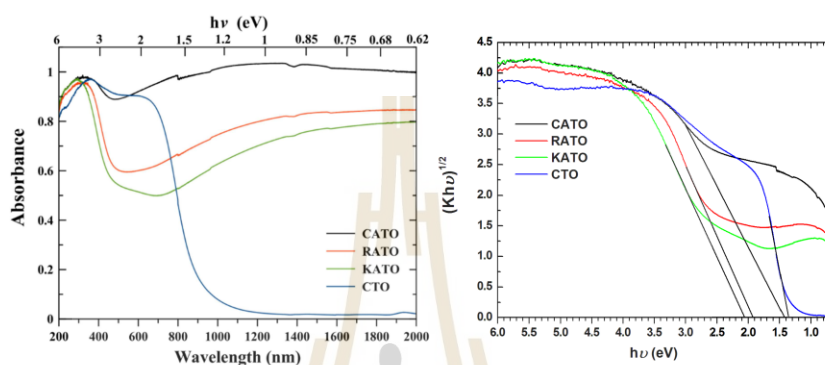
Fig. 8: UV-Vis spectra (a) and extrapolation of the band gap energy (b) of $CsTe_2O_6$ and $AAl_{0.33}Te_{1.67}O_6$ (A = Cs, Rb, and K)

Discussion

It has been established that $CsAl_{0.33}Te_{1.67}O_6$ shows relatively high conductivity [5]. Li et. al. [6] concluded that the conductivity comes from small deviations from stoichiometry which results in small amount of Te^{4+} producing mixed valence compounds. The n-type behavior in these series of compounds is explained by the presence of donor defect levels originating from Te^{4+}. In general, type of M cations in $Cs(M,Te)_2O_6$ affects the conductivities of the compounds as small M cation reduces M/Te-O distance thus destabilizes Te^{4+} in the structure increasing their energy level. In addition, some M cations could provide orbitals with appropriate energy to overlap with Te 5s which increase the conductivity.

When Cs is replaced by Rb and K in $Cs_{1-x}A_xAl_{0.33}Te_{1.67}O_6$, the difference in conductivity is very pronounced although the same Al is present. Additionally, samples containing Rb and K have much lower conductivities despite the smaller cell parameters. XPS results obtained in this work do not indicate any difference in the number of Te^{4+}, hence the number of defect levels, in all samples. In addition, we have also prepared and measured the conductivities of $CsAl_xTe_{2-x}O_6$ and $RbAl_xTe_{2-x}O_6$ with different x values. As shown in Fig. S1 (Supporting Information), the conductivities of both series exhibit similar Al content

Manuscript published in Journal of Alloys and Compounds

dependency which is also in agreement with the previous work [6]. It is, therefore, reasonable to conclude that the type and the amount of defect, e.g. Te^{4+}, are similar in all samples. If the number of Te^{4+} is similar, then the difference in conductivities must be related to Te^{4+} energy level relative to the conduction band.

Based on the band gap energy obtained from UV-Vis results and the VBM position obtained from XPS valence band spectra, we propose schematic band structure diagrams of the samples as depicted in Fig. 9. From the figure, the difference between Fermi energy level and the bottom of the conduction band (E_d) is obtained. Generally, the band diagrams of these four samples represent their semiconducting behavior. However, the activation energies of conduction indicate that their behaviors are different. The activation energy of conduction of $CsTe_2O_6$ (1.15 eV, Fig.7) is in the same order with its band gap energy suggesting the intrinsic semiconducting behavior. The conductivity of this sample is small because large energy is required to activate electrons across the band gap. It is noteworthy that E_d and the activation energy of conduction in $CsTe_2O_6$ are significantly different which indicates that there is no defect level at the Fermi energy level (E_F). On the other hand, the activation energies of $AAl_{0.33}Te_{1.67}O_6$ are close to E_d and much smaller than their band gap energy which suggests the presence of defect levels close to the conduction band within the band gap. The presence of such defect levels is a characteristic of n-type semiconductors which agrees well with the negative Seebeck coefficients [5]. E_d in these three samples indicate the position of defect levels relative to conduction band minimum (CBM) which determines conductivities of the samples.

Replacing Cs with Rb and K have two effects on the band diagram; lowering the VBM and increasing the band gap energy. It should be noted that lowering VBM in these cases is not the only cause of increasing the band gap. Without the presence of Cs, VBM of both $RbAl_{0.33}Te_{1.67}O_6$ and $KAl_{0.33}Te_{1.67}O_6$ are about 0.3 eV lower in energy. However, the band gap differences between the samples are 0.5-0.6 eV. As the conduction band should be mainly Te 5s with some contribution from Al and O, Te/Al-O bond distance and Te/Al-O-Te/Al bond angle must play important roles in determining the CBM. Additional detail studies are required to further explain this matter. Nevertheless, the combination of VBM lowering and the increase in band gap energy when Cs is replaced with Rb and K result in larger E_d and consequently lower conductivity.

Manuscript published in Journal of Alloys and Compounds
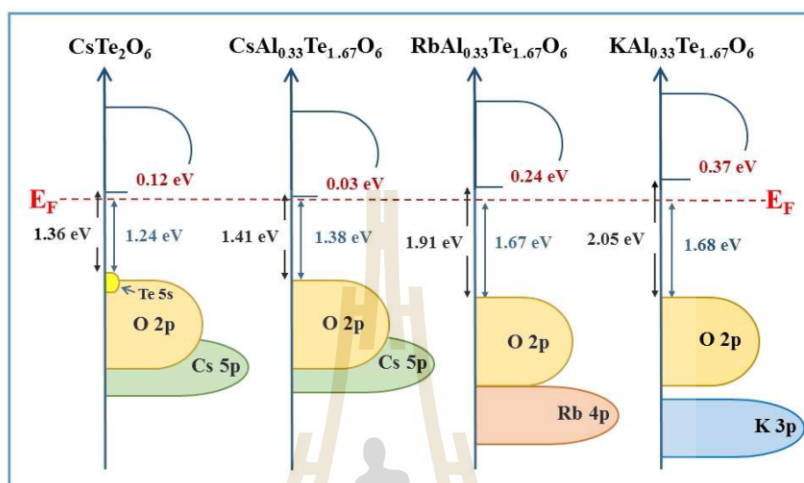
Compounds	Valence band position (eV)	Band gap energy (eV)	E_d (eV)	Activation energy of conduction (eV)
$CsTe_2O_6$	1.24	1.36	0.12	1.15
$CsAl_{0.33}Te_{1.67}O_6$	1.38	1.41	0.03	0.108
$RbAl_{0.33}Te_{1.67}O_6$	1.67	1.91	0.24	0.224
$KAl_{0.33}Te_{1.67}O_6$	1.68	2.05	0.37	0.364

Fig. 9 Schematic band structures of $CsTe_2O_6$ and $AAl_{0.33}Te_{1.67}O_6$ (A = Cs, Rb, and K)

Conclusions

Series of $AAl_{0.33}Te_{1.67}O_6$ (A = Cs, Rb, and K) with pyrochlore structure have been prepared by solid state reaction and their electronic properties have been characterized. Electrical conductivities of the compounds arise from small deviation from stoichiometry which results in Te^{4+}/Te^{6+} mixed valency as evidenced in XPS results. Although containing similar Te^{4+}/Te^{6+} mixed valency, the samples with Rb and K are significantly less conductive. Based on the obtained XPS at valence band region, optical band gap energy, and activation energy of conduction; the band diagrams are proposed and used to explain the large

Manuscript published in Journal of Alloys and Compounds

ACCEPTED MANUSCRIPT

difference in electrical conductivities. The band diagrams indicate that the samples are n-type semiconductor. The energy difference between CBM and donor states which determines the conductivity is affected by A cations. Replacing Cs with Rb and K increases this energy difference which consequently results in the lower electrical conductivity.

Supporting Information: 1. Figure showing the resistivity of $AAl_xTe_{2-x}O_6$ (A = Cs and Rb).

References

[1] H. Kawazoe, H. Yanagi, K. Ueda and H. Hosono, *Mrs Bull.* 25 (2000) 28-36.

[2] S. Noguchi and H. Sakata, *J. Phys. D: Appl. Phys.* 13 (1980) 1129.

[3] S. Cai, Y. Li, X. Chen, Y. Ma, X. Liu and Y. He, *J. Mater. Sci: Mater. Electron.* 27 (2016) 6166-6174.

[4] D. H. O'Neil, V. L. Kuznetsov, R. M. Jacobs, M. O. Jones and P. P. Edwards, *Mater. Chem. Phys.* 123 (2010) 152-159.

[5] T. Siritanon, G. Laurita, R. T. Macaluso, J. N. Millican, A. W. Sleight and M. Subramanian, *Chem. Mater.* 21 (2009) 5572-5574.

[6] J. Li, T. Siritanon, J. K. Stalick, A. W. Sleight and M. Subramanian, *Inorg. Chem.* 50 (2011) 5747-5754.

[7] W.-Y Howng and R. Thorn, *J. Phys. Chem. Solids.* 41 (1980) 75-81.

[8] Y. Lv, W. Yao, R. Zong and Y. Zhu, *Sci. Rep.* 6 (2016).

[9] R.Guje, G. Ravi, S. Palla, K. N. Rao and M. Vithal, *Mater. Sci. Eng. B* 198 (2015) 1-9.

[10] A. E. Morales, E. S. Mora and U. Pal, *Rev. Mex. Fis. S* 53 (2007) 18.

[11] G. Kresse and J. Hafner, *Phys. Rev. B* 48 (1993) 13115.

Manuscript published in Journal of Alloys and Compounds

[12] F. Fuchs, J. Furthmüller, F. Bechstedt, M. Shishkin and G. Kresse, *Phys. Rev. B* 76 (2007) 115109.

[13] J. P. Perdew, K. Burke and M. Ernzerhof, *Phys. Rev. Lett.* 77 (1996) 3865.

[14] P. E. Blöchl, *Phys. Rev. B* 50 (1994) 17953.

[15] G. Kresse and D. Joubert, *Phys. Rev. B* 59 (1999) 1758.

[16] M. Subramanian, G. Aravamudan and G. S. Rao, *Prog. Solid State Chem.* 15 (1983) 55-143.

[17] G. J. Thorogood, B. J. Kennedy, V. K. Peterson, M. M. Elcombe, G. J. Kearley, J. V. Hanna and V. Luca, *J. Solid State Chem.* 182 (2009) 457-464.

[18] R. T. Shannon and C. T. Prewitt, *Acta Crystallogr. B* 25 (1969) 925-946.

[19] R. t. Shannon, *Acta Crystallogr. A* 32 (1976) 751-767.

[20] A. Castro, I. Rasines and X. Turrillas, *J. Solid State Chem.* 80 (1989) 227-234.

[21] R. Marschall, A. Mukherji, A. Tanksale, C. Sun, S. C. Smith, L. Wang and G. Q. M. Lu, *J. Mater. Chem.* 21 (2011) 8871-8879.

[22] C. Guo, S. Yin, Q. Dong and T. Sato, *CrystEngComm* 14 (2012) 7727-7732.

[23] G. Ravi, N. K. Veldurthi, S. Palla, R. Velchuri, S. Pola, J. R. Reddy and M. Vithal, *Photochem. Photobiol.* 89 (2013) 824-831.

[24] V. Atuchin, V. Kesler, G. Meng and Z. Lin, *J. Phys. Condens. Matter.* 24 (2012) 405503.

[25] M. Sathiya, K. Ramesha, G. Rousse, D. Foix, D. Gonbeau, K. Guruprakash, A. Prakash, M. Doublet and J.-M. Tarascon, *Chem. Commun.* 49 (2013) 11376-11378.

[26] G. Tan, X. Zhang and Z. Chen, *J. Appl. Phys.* 95 (2004) 6322-6324.

[27] W. E. Sartz Jr, K. J. Wynne and D. M. Hercules, *Anal. Chem.* 43 (1971) 1884-1887.

[28] A. Heredia, M. Q. García, J. P. Mazariego and R. Escamilla, *J. Alloy Compd.* 504 (2010) 446-451.

[29] B. Slobodin, L. Surat, V. Zubkov, A. Tyutyunnik, I. Berger, M. Kuznetsov, L. Perelyaeva, I. Shein, A. Ivanovskii and B. Shulgin, *Phys. Rev. B* 72 (2005) 155205.

[30] S. Van den Berghe, J.-P. Laval, B. Gaudreau, H. Terryn and M. Verwerft, *J. nucl. mater.* 277 (2000) 28-36.

[31] S. B. Waghmode, R. Vetrivel, S. G. Hegde, C. S. Gopinath and S. Sivasanker, *J. Phys. Chem.* 107 (2003) 8517-8523.

[32] Y. Yang, X. Su, S. Pan, M. Zhang, Y. Wang, J. Han and Z. Yang, *CrystEngComm* 16 (2014) 1978-1984.

Manuscript published in Journal of Alloys and Compounds

[33] M. Han, K. Jiang, J. Zhang, W. Yu, Y. Li, Z. Hu and J. Chu, *J. Mater. Chem.* 22 (2012) 18463-18470.

[34] M. Okutan, H. I. Bakan, K. Korkmaz and F. Yakuphanoglu, *Phys. B Condens. Matter* 355 (2005) 176-181.

[35] H. Mizoguchi, P. Chen, P. Boolchand, V. Ksenofontov, C. Felser, P. W. Barnes and P. M. Woodward, *Chem. Mater.* 25 (2013) 3858-3866.

[36] L. Atkinson and P. Day, *J. Chem. Soc. A* (1969) 2423-2431.

arXiv:1805.10812v1 [cond-mat.stat-mech] 28 May 2018
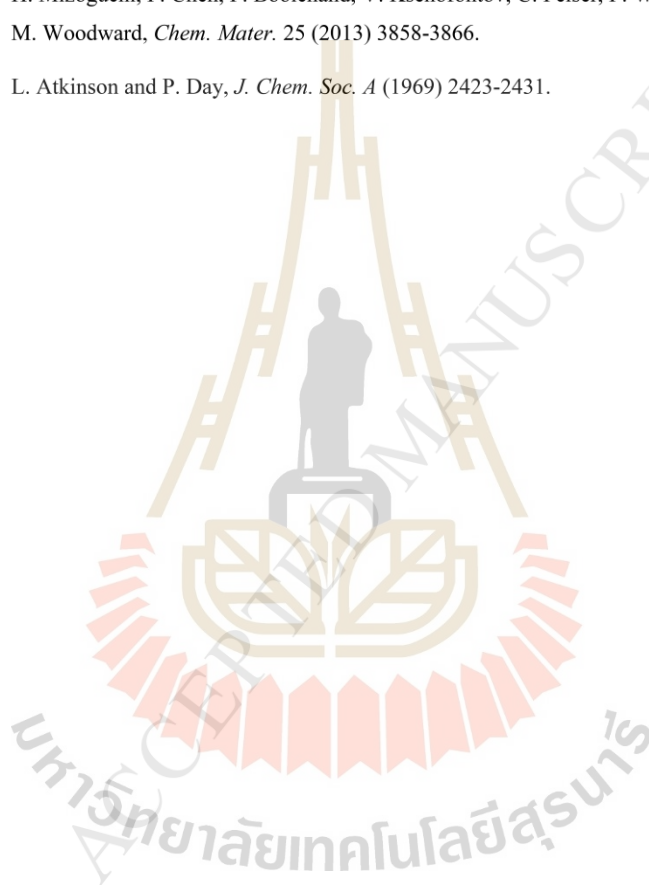
Statistical mechanics guides the motions of cm scale objects

S. Siriroj,[1] P. Simakachorn,[1,2] N. Khumtong,[2] T. Sukhonthamethirat,[2] S. Chaiyachad,[1,3] P. Chanprakhon,[1,3] K. Chanthorn,[1,3] S. Dawprateep,[1,3] T. Eknapakul,[1,3] I. Fongkaew,[1,3] C. Jaisuk,[1,3] T. Jampreecha,[1,3] W. Jindata,[1,3] Y. Kaeokhamchan,[1,3] T. Kongnok,[1,3] P. Laohana,[1,3] K. Lapawer,[1,3] S. Lowpa,[1,3] A. Mooltang,[1,3] S. Musikajaroen,[1,3] S. Nathabumroong,[1,3] A. Panpar,[1,3] S. Phumying,[1,3] S. Polin,[1,3] A. Rasritat,[1,3] A. Ritwiset,[1,3] W. Saengsui,[1,3] W. Saenrang,[1,3] T. Saisopa,[1,3] S. Sangphet,[1,3] T. Sawasdee,[1,3] S. Sonsupap,[1,3] S. Suksombat,[1,3] T. Suyuporn,[1,3] M. Tepakidareekul,[1,3] T. Thiwatwaranikul,[1,3] P. Tipsawat,[1,3] S. Waiprasoet,[1,3] and W. Meevasana[1,3,∗]

[1]*School of Physics, Suranaree University of Technology, Nakhon Ratchasima, 30000, Thailand*
[2]*SCiUS program, Suranaree University of Technology and Rajsima Wittayalai School, Nakhon Ratchasima, 30000, Thailand*
[3]*Thailand Center of Excellence in Physics, CHE, Bangkok 10400, Thailand*
(Dated: May 29, 2018)

Calculations and mechanistic explanations for the probabilistic movement of objects at the highly relevant cm to m length scales has been lacking and overlooked due to the complexity of current techniques. Predicting the final-configuration probability of flipping cars for example remains extremely challenging. In this paper we introduce new statistical methodologies to solve these challenging macroscopic problems. Boltzmann's principles in statistical mechanics have been well recognized for a century for their usefulness in explaining thermodynamic properties of matter in gas, liquid and solid phases. Studied systems usually involve a large number of particles (e.g. on the order of Avogadro's number) at the atomic and nanometer length scales. However, it is unusual for Boltzmann's principles to be applied to individual objects at centimeter to human-size length scales. In this manuscript, we show that the concept of statistical mechanics still holds for describing the probability of a tossed orthorhombic dice landing on a particular face. For regular dice, the one in six probability that the dice land on each face is well known and easily calculated due to the 6-fold symmetry. In the case of orthorhombic dice, this symmetry is broken and hence we need new tools to predict the probability of landing on each face. Instead of using classical mechanics to calculate the probabilities, which requires tedious computations over a large number of conditions, we propose a new method based on Boltzmann's principles which uses synthetic temperature term. Surprisingly, this approach requires only the dimensions of the thrown object for calculating potential energy as the input, with no other fitting parameters needed. The statistical predictions for landing fit well to experimental data of over fifty-thousand samplings of dice in 23 different dimensions. We believe that the ability to predict, in a simple and tractable manner, the outcomes of macroscopic movement of large scale probabilistic phenomena opens up a new line of approach for explaining many phenomena in the critical centimeter-to-human length scale.

PACS numbers:

Tossing a die from a significant height on a hard floor is generally thought as a random process since its motion is unpredictable from the initial state of the die. However, regardless of its random motion, one can accurately predict that the probability of a die landing on any particular face of a standard cubic die is 1/6. This predictability is the result of the six-fold symmetry of the die alone. It is non-trivial to ask, "how will this 1/6 probability change if we break this six-fold symmetry?" The motion of a macroscopic object is in principle governed by classical mechanics and Newtons laws. If all the necessary initial conditions are given, the equations of motion can be written for calculating the coordinates and momenta of an object anytime thereafter. In practice, the bouncing motion of simple objects, e.g. dice and coins, is already difficult to calculate. We are not aware of any previous work studying the motion of a bouncing die using the full die geometry, although the bouncing motion of a simplified object such as a barbell has already been reported by Nagler and Richter [1]. The calculated phase space of the final configuration of

the barbell (i.e. whether the barbell points to the left or right) is already very complex [1]. Furthermore, phase spaces with different parameters for the surrounding environment (e.g. friction coefficients) are computationally intensive to be re-calculated every time when a condition is changed. Note that if no bouncing occurs (e.g. a thick coin landing on a soft-rice bed [2]), the phase space can be calculated; our work looks into a more general case where bouncing is allowed.

Since the classical-mechanics approach is so complex as to be impracticable and computationally intractable, we looked for a simpler method that could utilize statistical principles. The Boltzmann distribution in statistical mechanics attracted our attention as the principle requires only knowing an ensemble of energy states and temperature to determine the distribution in each state of particles. By constructing a partition function based on this Boltzmann factor, $e^{-\varepsilon_i/k_B T}$ where ε_i is the energy in each state i, and T is temperature, one can predict many thermodynamic properties such as heat capacity of a solid and magnetic susceptibility as a function of tem-

Manuscript published in Condensed Matter Statistical Mechanics
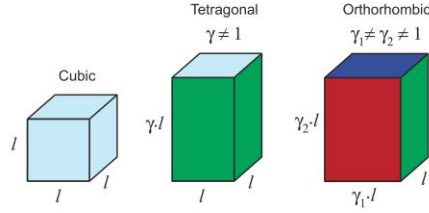
FIG. 1: Geometry of regular dice (left), tetragonal dice (middle) and orthorhombic dice (right). The parameters γ, γ_1 and γ_2 are the ratios between extended/contracted sides and the common length l.

FIG. 2: Probability distribution of landed dice being in different orientations shown in the inset figures for (a) tetragonal dice and (b) orthorhombic dice. The solid lines are model based predictions.

perature [5, 6]. The concepts of statistical mechanics are also useful at large length scales (e.g. star distribution [3], with proposed entropic forces [4]) used for objects such as stars and black holes. In this work, we are interested in applying the Boltzmann concept to a set of tossed dice in 23 different dimensions (see results in Fig. 2). The redefined temperature term, which is important for describing the outcome, is explained in a later section (see eq. (13)).

For experimental measurements, the die shape and parameters are defined as follows: Fig. 1 shows a cubic die with length of each side l. For the tetragonal and orthorhombic dice, γ, γ_1 and γ_2 are dimensionless ratios between extended/contracted sides and the common length l, describing the dimensions of each die. All dice are custom-made from solid aluminum. With l of 0.9 cm, there are 11 sizes of tetragonal dice with varied γ as displayed along x-axis in Fig. 2(a) and 11 sizes of orthorhombic dice with fixed γ_1 of 1.3 and varied γ_2 as displayed along x-axis in Fig. 2(b). For each dimension, we toss the dice around 2400 times on average by dropping them from a height of 27 cm above a leveled and flat floor composed of thick and hard ceramic. Note that the height from which the dice are dropped is many times larger than the dimension of each dice. At this height, random outcomes are expected and the regular die gives a 1/6 measured probability as expected due to symmetry (please see supplementary materials for more explanation [8]). To avoid biased measurements, the 33 persons, who tossed the dice, were not told about the prediction results beforehand.

As shown in Fig. 2(a), we have measured the final configuration probabilities of tossed tetragonal dice by varying the γ factor. The outcome appears to have a well-organized structure for the probability when plotted as a function of the dimensionless length ratio γ. As the die is colored with blue and green on 2 square faces and 4 rectangular faces respectively, the blue region in Fig. 2(a) represents the probability of the blue face being up (called γ state) and vice versa for the green region; for
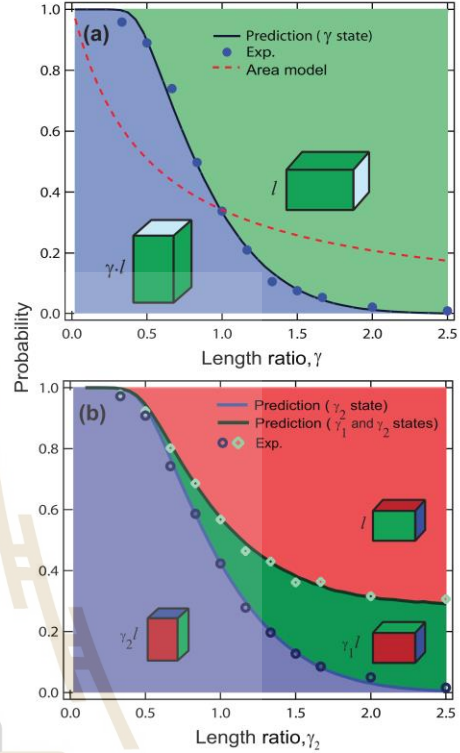
examples, a) if γ is nearly zero (i.e. a thin square sheet), the probability in observing the blue face up should be nearly 1 b) if γ is large (i.e. a long stick with square cross-section), the probability of finding the green face up should also be nearly 1 and c) if γ is exactly one (i.e. a cubic), the probability in landing with a blue(green) face up should theoretically be around 1/3 and 2/3 respectively due to the symmetry. For the orthorhombic dice, the probability outcome as a function of γ_2 is shown in Fig. 2(b). The blue region represents the probability of the blue face being up (the γ_2 state) and the same is applied for the red and green regions.

To model these experimental results, one could simply presume that the probability outcome is directly proportional to the area of the face being up. For exam-

Manuscript published in Condensed Matter Statistical Mechanics

ple, in the case of a tetragonal die with dimension of $1{\times}1{\times}1.5$ cm^3 (i.e. $\gamma = 1.5$), the area of blue faces will be $1{+}1 = 2$ cm^2 while the total area of all faces will be $1{+}1{+}1.5{+}1.5{+}1.5{+}1.5 = 8$ cm^2; hence this area model will predict that the probability of getting blue faces should be $2/8 = 0.25$ while the measured probability is only around 0.076. In Fig. 2(a), this area model for the same range of γ is plotted. This area model is clearly erroneous except for around $\gamma = 0$ and 1.

In this work, a statistical-mechanics approach is chosen and the concept of a Boltzmann distribution is applied. Through rederiving the Boltzmann distribution function we can translate and define the relevant parameters, including energy states and temperature, which are relevant to predicting and understanding our experimental results.

The Boltzmann distribution of a system at equilibrium with a total number of particles $N = \sum_i n_i$ and total energy $E = \sum_i \varepsilon_i n_i$ (for all energy states ε_i) can be derived by maximizing the entropy $S = k \ln W$ [7]. The constraints are that $N = \sum_i n_i = const$ and $E = \sum_i \varepsilon_i n_i = const$. Then one will arrive that

$$n_i = e^{-\alpha} e^{-\beta \varepsilon_i} \qquad (1)$$

where α and β are constants.

With $N = \sum_i n_i$ and definition of temperature T , we can arrive with

$$n_i = \frac{N}{Z} e^{-\varepsilon_i/kT} \qquad (2)$$

where the partition $Z = \sum_i e^{-\varepsilon_i/kT}$. Details of the derivation can be found in the supplementary information [8].

In the continuous case, an average energy $\langle \varepsilon \rangle = \langle \varepsilon(x_i, p_i) \rangle$ [5, 6] can be calculated as:

$$\langle \varepsilon \rangle = \frac{\int \int \varepsilon \cdot e^{-\varepsilon(x_i, p_i)/kT} dx_i dp_i}{\int \int e^{-\varepsilon(x_i, p_i)/kT} dx_i dp_i}. \qquad (3)$$

In this way, one can associate the temperature term with the average energy instead of using the formal definition $T \equiv \partial E/\partial S$ which may be harder to use in our case. For example, the average kinetic energy of monatomic gas is:

$$\langle \varepsilon \rangle = \frac{\int \int \int \frac{p_x^2 + p_y^2 + p_z^2}{2m} e^{-\frac{p_x^2 + p_y^2 + p_z^2}{2mkT}} dp_x dp_y dp_z}{\int \int \int e^{-\frac{p_x^2 + p_y^2 + p_z^2}{2mkT}} dp_x dp_y dp_z} = \frac{3}{2}kT \quad (4)$$

where $\varepsilon = (p_x^2 + p_y^2 + p_z^2)/2m$; hence, the temperature term $kT = 2\langle \varepsilon \rangle/3$.

In our case, the total energy of a die, which includes a) translational kinetic energy, b) rotational kinetic energy
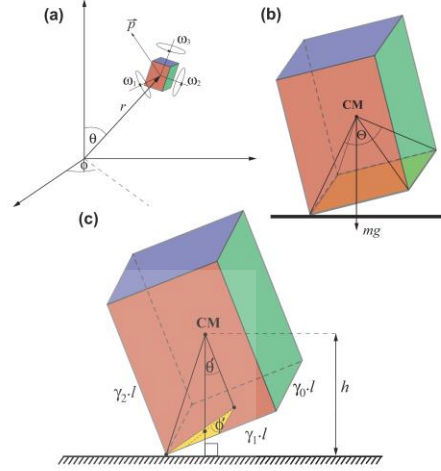

FIG. 3: Schematic diagrams of (a) a die with degrees of freedom for calculating the total energy (eq. (5)), (b) the solid angle where the weight vector points within and the final configuration will end up in γ_2 state, and (c) defined variables for integrations in eq. (8).

and c) potential energy (see Fig. 3(a)), can be written as:

$$\varepsilon_d = \varepsilon(\omega_i, p_i, r, \theta, \phi) = \sum_{i=1}^{3} \frac{p_i^2}{2m} + \sum_{j=1}^{3} \frac{1}{2} I_j \omega_j^2 + mgr \cos\theta. \qquad (5)$$

To avoid confusion with the common temperature, we will replace the term kT by $\kappa\tau$ which will be used as the redefined temperature for large objects from now on. By using eq. (3), the average energy $\langle \varepsilon_d \rangle$ as a function of $\kappa\tau$ can be calculated as:

$$\langle \varepsilon_d \rangle = \frac{\int \int \int \varepsilon(\omega_i, p_i, r, \theta, \phi) \cdot e^{-\varepsilon(\omega_i, p_i, r, \theta, \phi)/\kappa\tau} d^3p d^3\omega d^3r}{\int \int \int e^{-\varepsilon(\omega_i, p_i, r, \theta, \phi)/\kappa\tau} d^3p d^3\omega d^3r}$$
$$= 6\kappa\tau. \qquad (6)$$

The average energy can now be written as a function of $\kappa\tau$ (i.e. eq. (6) whose detailed derivation is in Supplemental Material [8]). In general, the $\kappa\tau$ term is arbitrary. However, when a specific condition is given, the $\kappa\tau$ term can be calculated via a self consistent equation. This is a crucial step. When the orthorhombic dice in Fig. 2(b) were tossed, the total energy of the dice started from the high value and then dissipated until coming to rest in

either blue, green or red configuration. In the case that the dice ended up being in blue region (γ_2 state), potential energy at some point in time (when kinetic energy is zero) must be in the configuration that a die has one corner (or more) touching the floor while the weight vector (mg) points down within the solid angle Θ as shown in Fig. 3(b); then the die may move around some more and eventually dissipates energy until it reaches the γ_2 state. These particular configurations give us the condition to calculate the average energy as follow.

$$\langle \varepsilon_d \rangle_{general} = 6\kappa\tau = \langle \varepsilon_d \rangle_{constrained}. \tag{7}$$

In our case, since the kinetic energy at that moment is zero and one corner touches the floor, we need to integrate only in angular space (θ, ϕ):

$$\langle \varepsilon_d \rangle = 6\kappa\tau = \frac{\int \varepsilon(\theta, \phi) \cdot e^{-\varepsilon(\theta,\phi)/\kappa\tau} d\Theta}{\int e^{-\varepsilon(\theta,\phi)/\kappa\tau} d\Theta}. \tag{8}$$

Instead of using the observer frame, the integral over the triangular solid angle (yellow region) in Fig. 3(c) is done in the object frame ($\acute{\theta}$, $\acute{\phi}$):

$$Ie(\gamma_0, \gamma_1, \gamma_2, \kappa\tau) = \int \varepsilon \cdot e^{-\varepsilon/\kappa\tau} d\Theta$$
$$= \int mg \cdot h(\acute{\theta}, \acute{\phi}) \cdot e^{-mgh/\kappa\tau} \sin(\acute{\theta}) d\acute{\theta} d\acute{\phi}$$
$$Iz(\gamma_0, \gamma_1, \gamma_2, \kappa\tau) = \int e^{-\varepsilon/\kappa\tau} d\Theta$$
$$= \int e^{-mgh/\kappa\tau} \sin(\acute{\theta}) d\acute{\theta} d\acute{\phi} \tag{9}$$

where

$$\acute{\phi} \in \{0, \tan^{-1}(\gamma_1/\gamma_0)\}, \tag{10}$$
$$\acute{\theta} \in \{0, \tan^{-1}(\gamma_0/\gamma_2 \cos\acute{\phi})\}, \tag{11}$$
$$h = \frac{l}{2}(\gamma_0 \sin\acute{\theta} \cos\acute{\phi} + \gamma_1 \sin\acute{\theta} \sin\acute{\phi} + \gamma_2 \cos\acute{\theta}) \tag{12}$$

whose detailed derivations can be read from Ref. [8].

To calculate the average energy, we need to integrate all the 6 faces of the die. This can be calculated using eqs. (8)-(11) where the parameters γ_0, γ_1 and γ_2 can be swapped for the integration on each face (e.g. the yellow triangle in Fig. 3(c)) and for each configuration of γ_0, γ_1 and γ_2, there are 8 equivalent pieces on the die surface. By summing Ie and Iz for all configurations, covering all the die surface, the eq. (7) can be written as:

$$\langle \varepsilon_d(\kappa\tau) \rangle = \frac{\sum_{i \neq j \neq k} 8Ie(\gamma_i, \gamma_j, \gamma_k, \kappa\tau)}{\sum_{i \neq j \neq k} 8Iz(\gamma_i, \gamma_j, \gamma_k, \kappa\tau)} = 6\kappa\tau \tag{13}$$

where each index runs from 0 to 2.
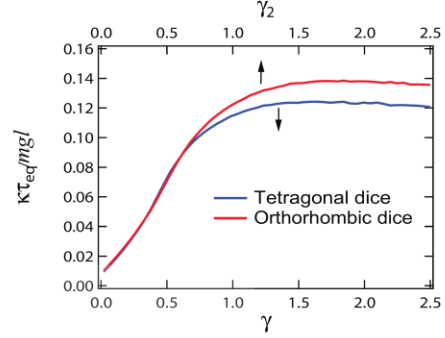
FIG. 4: Temperature

From this eq. (12), the $\kappa\tau_{eq}$ for each γ_2 of the orthorhombic dice can be calculated numerically as shown in Fig. 4. And by plugging in these calculated temperature terms $\kappa\tau_{eq}$, the probability in getting blue, green or red face of the orthorhombic dice is given by:

$$p_{orth,blue} = \frac{Iz(\gamma_0, \gamma_1, \gamma_2, \kappa\tau_{eq}) + Iz(\gamma_1, \gamma_0, \gamma_2, \kappa\tau_{eq})}{Z_{orth}}$$
$$p_{orth,green} = \frac{Iz(\gamma_0, \gamma_2, \gamma_1, \kappa\tau_{eq}) + Iz(\gamma_2, \gamma_0, \gamma_1, \kappa\tau_{eq})}{Z_{orth}}$$
$$p_{orth,red} = \frac{Iz(\gamma_1, \gamma_2, \gamma_0, \kappa\tau_{eq}) + Iz(\gamma_2, \gamma_1, \gamma_0, \kappa\tau_{eq})}{Z_{orth}}$$
$$\tag{14}$$

where $Z_{orth} = \sum_{i \neq j \neq k} Iz(\gamma_i, \gamma_j, \gamma_k, \kappa\tau_{eq})$, $\gamma_0 = 1$ and $\gamma_1 = 1.3$.

For the tetragonal dice, the calculations are the same as the case of the orthorhombic dice except setting $\gamma_0 = \gamma_1 = 1$. The temperature term for the tetragonal dice is also plotted in Fig. 4. It should be emphasized that the normalized temperature term $\kappa\tau_{eq}/mgl$ only depends on the shape (i.e. dimensionless γ terms) but not the mass and the length. Hence eq. (13) will give the same result of probability for the object with the same shape regardless of its size. This is consistent with the classical mechanics where the final configuration should not depend on mass or length of the object (e.g. a freely-falling object always accelerates at g).

Finally, the predictions from eq.(13) are calculated by using the $\kappa\tau_{eq}/mgl$ shown in Fig. 4. The predictions are then plotted in Fig. 2(a) and 2(b). The comparison with the experimental measurements shows excellent agreement with coefficients of determination (R^2): 0.996 for γ state in Fig. 2(a), 0.997 and 0.995 for γ_2 and $\gamma_1 + \gamma_2$ state in Fig. 2(b) respectively.

With the statistical approach providing for high accu-

Manuscript published in Condensed Matter Statistical Mechanics

5

racy predictions, it could open the door to many applications. Without having to resort to calculating ensembles of full trajectories, the Boltzmann formalism with redefined temperature can be used as a simple and tractable method for explaining and understanding the probability distribution of the final configuration of moving macroscopic objects which eventually come to rest, e.g. saving the cost of computation and experimental testing. This method may also find application to the packing problems [9–12]. By pouring objects into a container (without shaking), the packing factor may be difficult to calculate without knowing the probability of each object landing in a particular configuration.

* Authors to whom correspondence should be addressed. Electronic addresses: worawat@g.sut.ac.th

[1] J. Nagler and P. Richter, Phys. Rev. E. 78, 036207 (2008).
[2] E.H. Yong and L. Mahadevan, Am. J. Phys. 79, 1195 (2011).
[3] J. N. Bahcall and R. A. Wolf. Astron. J. 209, 214-232 (1976)
[4] E. Verlinde, J. High Energy Phys. 1104, 29 (2011).
[5] R. K. Pathria, "Statistical mechanics," Butterworth Heinemann, Oxford, UK, 1972.
[6] D. L. Goodstein, States of Matter, Prentice-Hall, Englewood Cliffs, NJ, 1975.
[7] Derivation of Boltzmann distribution is from the lecture note of Prof. Angel C de Dios; Also, H. A. Bent, "The Second Law," Oxford University Press, New York, 1965.
[8] See Supplemental Material at [URL] for probability as a function of dropping height and mathematical derivations.
[9] A. Donev, F. H. Stillinger, P. M. Chaikin and S. Torquato, Phys. Rev. Lett. 92, 255506 (2004)
[10] A. Donev, I. Cisse, D. Sachs, E. A. Variano, F. H. Stillinger, R. Connelly, S. Torquato, P. M. Chaikin, Science. 303, 990993 (2004)
[11] A. Jaoshvili, A. Esakia, M. Porrati and P. M. Chaikin, Phys. Rev. Lett. 104, 185501 (2010)
[12] C. Zong, Expo. Math. 32, 297364 (2014)

Disentangling small-polaron and Anderson-localization effects in ceria:
Combined experimental and first-principles study

Taras Kolodiazhnyi,[1,*] Pannawit Tipsawat,[2] Thitirat Charoonsuk,[3] Thanundon Kongnok,[2,4] Sirichok Jungthawan,[2,4,5]
Suwit Suthirakun,[5,6] Naratip Vittayakorn,[7] and Santi Maensiri[2,5]

[1]*National Institute for Materials Science, 1-1 Namiki, Tsukuba, Ibaraki 305-0044, Japan*
[2]*School of Physics, Institute of Science, Suranaree University of Technology, Nakhon Ratchasima 30000, Thailand*
[3]*Advanced Material Research Unit, Faculty of Science, King Mongkut's Institute of Technology Ladkrabang, Bangkok 10520, Thailand*
[4]*Thailand Center of Excellence in Physics (ThEP), Commission on Higher Education, 328 Si Ayutthaya Road, Bangkok 10400, Thailand*
[5]*Center of Excellence in Advanced Functional Materials, Suranaree University of Technology, Nakhon Ratchasima 30000, Thailand*
[6]*School of Chemistry, Institute of Science, Suranaree University of Technology, Nakhon Ratchasima 30000, Thailand*
[7]*Department of Chemistry, Faculty of Science, King Mongkut's Institute of Technology Ladkrabang, Bangkok 10520, Thailand*

By comparison of the electrical conductivity of ceria doped with penta- and hexavalent ions, we separate the total electron localization energy into the two contributions originating from the small polaron effects and the Coulomb interaction with the donor ions. The upper bound of the itinerant small polaron hopping energy is estimated at 66 ± 20 meV. The binding energy of the $Ce^{3+}-M^{5+/6+}$ defect complex increases from 121 meV for $M = Nb^{5+}/Ta^{5+}$ to 243 meV for $M = W^{6+}/U^{6+}$. The first-principles simulations are in qualitative agreement with the experimental findings. At low temperatures the f electrons bound to the donor defects show dielectric relaxation with the lowest activation energy of 2.7 and 17 meV for Nb(Ta)- and W-doped ceria, respectively. Remarkably, these energies are significantly smaller than the hopping energy of the itinerant small polarons. While both the electron-lattice and the electron-defect interactions cause the f electron localization in real-case ceria, the latter effects seem to be the dominant.

I. INTRODUCTION

Electron localization plays a central role in the metal-insulator transition in solids. Carrier localization can be driven by spin-/charge-density waves, Mott transition, small polaron (SP) formation, lattice disorder, etc. For example, manifestation of the Anderson-type localization [1] is found in random-field-induced carrier localization in doped Si, and random-bond-induced localization in sulfur [2]. On the other hand, n-type CeO_2 has been considered a textbook example of a SP model [3,4] where f electrons are localized at the Ce^{3+} ions as a result of a strong electron-phonon interaction and local lattice distortions of the nearby ions [5].

Very recent studies of n-type ceria, however, reveal that, in addition to the SP effects, electrons may localize next to the donor ions (or oxygen vacancies) forming a bound small polaron (BSP) [6] as illustrated in Fig. 1. In the latter case, the main cause of the BSP formation could be disorder-induced Anderson localization of the f electron next to the donor/defect site. Indeed, as was pointed out in Ref. [7], both SP and Anderson localization effects are intertwined in the partially disordered solids. The first attempt to disentangle these two effects using the first-principles calculations for reduced ceria was reported recently in Ref. [8]. It was found that the f electron localization is caused by both the polaronic effects ($E_h \approx 120$ meV) and the binding to the donor defect,

e.g., oxygen vacancy ($E_b \approx 137$ meV), where E_h is the SP hopping (diffusion) energy and E_b is the binding energy of the localized f electron to the nearest donor defect (not to be confused with the binding energy of SP).

In this paper, we attempt to disentangle the SP and the Anderson disorder effects and to get an experimental estimate of the E_h and E_b using a series of donor-doped ceria with different donor effective charges. We complement our experimental findings with the results of the first-principles calculations. Our results indicate that both the electron-lattice and electron-defect interactions contribute to the total localization energy of the f electron in ceria. However, with an increase in the effective charge of the donor ion, the electron-defect interaction becomes the dominant one. As such, the ideal SP picture is inadequate and requires us to include the defect-induced disorder effects which dominate the electron localization in real-case (i.e., defective) ceria.

II. MATERIALS AND METHODS

Polycrystalline $Ce_{1-x}M_xO_2$ ceramics, where $M = Nb$, Ta, and W, with target $x = 0–0.01$ were used for this study. Nb- and Ta-doped CeO_2 samples where the same as those reported in Ref. [6]. The details of their preparation can be found elsewhere [6]. W-doped ceramics were prepared at identical conditions to those of Nb- and Ta-doped CeO_2. The 99.99% pure WO_3 from High Purity Chemicals, Japan was used as a source of W^{6+} ion.

*kolodiazhnyi.taras@nims.go.jp

Manuscript published in Physical Review B
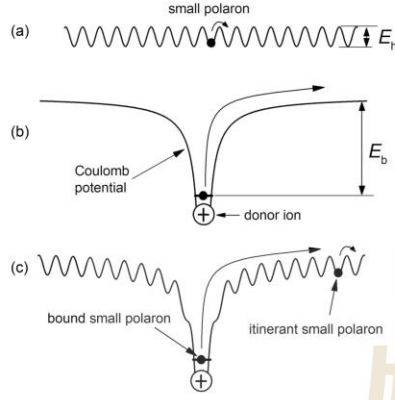
FIG. 1. Schematics of the itinerant SP (a) and the SP bound to donor defect (c) by Coulomb potential (b).

FIG. 2. Electrical conductivity of $Ce_{1-x}M_xO_2$, $M = Nb$, Ta, and W, as a function of reciprocal temperature. The concentration of Ce^{3+} per formula unit is indicated in the legend. The conductivity of Ce_2O_3 adapted from Ref. [19] is included for comparison.

The concentration of Ce^{3+} ions in the sintered ceramics was determined by fitting the dc magnetic susceptibility with the van Vleck equation, taking into account the crystal field effects as described in Ref. [9]. Magnetic moment in the 2–300 K range was measured using the Magnetic Properties Measurements System (MPMS-XL, Quantum Design, USA) at 5000 Oe. Electrical conductivity of polycrystalline ceramics were extracted from the Nyquist plot of the complex impedance, Z^*, in the 1 Hz–1 MHz frequency range. The Physical Property Measurement System (PPMS, Quantum Design, USA) was used to control the sample temperature in the 2–360 K interval.

The electron localization in doped CeO_2 was also modeled by using the Vienna Ab initio Simulation Package [10,11] based on density functional theory (DFT) [12,13]. The Perdew-Burke-Ernzerhof generalized gradient approximation was employed as the exchange and correlation energies [14–16]. The $2 \times 2 \times 2$ supercell was used to model the defect and the polaron formation in doped CeO_2. The cutoff energy for plane-wave expansion was set to 400 eV and $2 \times 2 \times 2$ mesh of special k-points was used. A denser $3 \times 3 \times 3$ k-points mesh was used for better accuracy in density of states (DOS) calculations. Due to the lack of cancellation of the Coulomb self-interaction, a Hubbard-like term [17] was introduced to account for the on-site interactions ($U_{eff} = 4.5$ eV in the case of Ce $4f$ orbitals).

The polaron formation is investigated by calculating self-trapping energy of an excess electron (E^{ST}), i.e., the energy gained by a SP formation, that is defined as [8]

$$E^{ST} = E_{tot}(\text{polaron}) - E_{tot}(\text{delocalized}), \qquad (1)$$

where $E_{tot}(\text{polaron})$ is the total energy of the supercell containing a SP, and $E_{tot}(\text{delocalized})$ is the total energy of supercell with an extra electron delocalized in conduction band [8]. The positive/negative value of E^{ST} indicates that the polaron formation is unfavorable/favorable with reference to the delocalized electronic state. The formation energy of a

dopant M substituting for Ce atom, $E^f(M^q)$, where $M = Nb$, Ta, W, and U, is given by [18]

$$E^f = E_{tot}(M^q) - [E_{tot}(\text{bulk}) + \mu_M - \mu_{Ce}] + q(E_{VBM} + E_F) + \Delta^q, \qquad (2)$$

where $E_{tot}(M^q)$ is the total energy of the supercell containing the defect in the charge state q (note that this charge state is not the oxidation number), and $E_{tot}(\text{bulk})$ is the total energy of perfect bulk CeO_2 with the same supercell. The μ_M, where $M = Nb$, Ta, W, and U, is a chemical potential of a dopant that substitutes Ce atom with a chemical potential μ_{Ce}. The value of chemical potential is irrelevant when comparing the relative stability of a similar defect for different charge states. In this paper, the formation energies reported here were obtained by setting chemical potential of all elements to zero. The Fermi level, E_F, representing the energy of the electron reservoir is a variable in this formalism and referenced to the valence band maximum (VBM, E_{VBM}) of bulk. Finally, Δ^q is the charge-state dependent correction due to the finite size of the supercells [20,21].

III. RESULTS AND DISCUSSION

A. Experimental results

Temperature dependence of electrical conductivity, σ, for selected Nb-, Ta-, and W-doped CeO_2 is shown in Fig. 2. The activation energy of conductivity, E_σ, for $Ce_{1-x}W_xO_2$ extracted from the Arrhenius-type dependence is 309 ±17 meV. This energy is notably higher than the $E_\sigma \sim 190 \pm 21$ meV found in Nb- and Ta-substituted CeO_2 [6]. A large difference between the activation energies of Nb(Ta)- and W-doped CeO_2 is highly unusual for a SP model of ceria which claims that the SP hopping energy, E_h, is independent on the type of the donor dopant. This claim is based on the major assumption that the E_h in ceria is determined by the

Manuscript published in Physical Review B

electron-phonon interactions, whereas the defects and disorder play a secondary role. While this assumption may still be valid for the ideal, defect-free ceria, the experimental data for a real-case ceria points to a different picture.

In contrast to what would have been expected in the ideal SP scenario, we speculate that the large difference in the E_σ for n-type ceria comes from the different types of the donor dopants. In particular, the different values of E_σ for Nb(Ta)- and W-doped CeO_2 may be associated with the different effective charges, Δq, of the donor ions. For a purely ionic picture, the Δq for $Ta^{5+}(Nb^{5+})$ and W^{6+} ions substituting for Ce^{4+} host is $+1|e|$ and $+2|e|$, respectively.

The Nb and Ta ions substituting Ce host are expected to have an oxidation state of 5+. This is based on the fact that we are not aware of any Nb- or Ta-based metal oxide compound sintered in air ($P_{O_2} = 0.2$ atm) where oxidation states of Nb or Ta are lower than 5+. This assumption is also confirmed by the first-principles DFT calculations in Ref. [22] and in our DFT calculations presented in the paper. For oxidation state of U^{6+}, we rely on the DFT calculations presented in Ref. [23] that show P_{O_2} independent region above $P_{O_2} = 10^{-15}$ atm that confirms that the Ce^{3+} concentration is fixed by the donor dopants. Our DFT calculations also indicate the U^{6+} ground state. For W dopant, we rely on our DFT results, which indicate that the W^{6+} is the most energetically favorable state. Another indirect evidence that the electrons are localized on Ce^{3+} $4f$ rather than on the W $5d$ orbitals is the absence of the Curie-Weiss behavior of magnetic susceptibility.

To distinguish between the itinerant SP and the defect-bound SP effects, the SP conductivity in ceria can be expressed as

$$\sigma = e\mu n \approx e\mu_0 \exp(-E_h/k_B T)[Ce^{3+}]\exp(-E_b/k_B T), \quad (3)$$

where the term $\mu_0 \exp(-E_h/k_B T)$ accounts for the SP mobility and the term $[Ce^{3+}]\exp(-E_b/k_B T)$ accounts for the concentration of the itinerant SPs. The $[Ce^{3+}]$ is the concentration of the Ce^{3+} ions, k_B is the Boltzmann constant, and T is the absolute temperature. According to Eq. (3), the total activation energy of conductivity, E_σ, is a sum of the SP hopping and defect binding energies: $E_\sigma = E_h + E_b$. As shown schematically in Fig. 1, the SP transport occurs by the bound SP first becoming itinerant by breaking away from the donor defect followed by the phonon-assisted hopping of itinerant SP.

How one can distinguish experimentally between the E_h and E_b? One has little control over the SP hopping (diffusion) energy, E_h, as it is not easy to modify the optical and acoustic phonons under ambient pressure. We focus, therefore, on the [f electron—defect] binding energy, E_b. Here we make a major assumption that the main contribution to E_b comes from the electrostatic interaction between the donor defect and the f electron. We believe that this assumption is justified by the strongly localized nature of the $4f$ electron in ceria. In this case, E_b will depend on the effective charge of the donor defect, Δq, as

$$E_b \propto \Delta q/r, \quad (4)$$

where r is the distance between the donor defect and the Ce^{3+} ion (i.e., $r \sim 3.83$ Å when donor is located on the cation site).
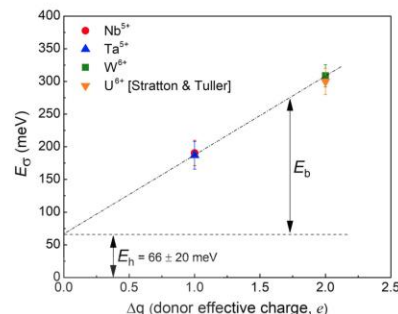
FIG. 3. Activation energy of the conductivity of the donor-doped ceria as a function of the effective charge of the donor ion, Δq.

Therefore, by varying the donor effective charge, Δq, one can vary the E_b.

The experimental E_σ for the different values of the effective donor charge are summarized in Fig. 3 for Nb-, Ta-, W-, and U-doped CeO_2. The E_σ for U-doped ceria was adapted from Ref. [24]. Remarkably, the experimental values of activation energy of conductivity for W^{6+}- and U^{6+}-doped ceria agree within the standard deviation as do the E_σ values for the Nb^{5+}- and Ta^{5+}-doped ceria.

We speculate that the higher E_σ values for W(U)-doped ceria as compared to the Nb(Ta)-dopants are attributed to the higher Δq in the former compounds and serve as an indirect support that the main contribution to the E_b comes from the Coulomb interactions between the point defects and f electrons. A linear extrapolation of E_σ to $\Delta q = 0$ in Fig. 3 yields $E_h \sim 66 \pm 20$ meV, which is the estimated hopping energy of the itinerant SP in ceria. The E_b values obtained from Fig. 3 for Nb(Ta)- and W(U)-doped ceria are 121 and 243 meV, respectively. A twofold enhancement in E_b for W(U) dopants as compared to the Nb(Ta) dopants is in quantitative agreement with that predicted by Eq. (4).

This excellent agreement, however, might be somewhat accidental because of the rather crude assumptions made in the estimation of the donor effective charge. This is particularly relevant to the W^{6+} defect, which is charge compensated by the two Ce^{3+} ions. Assuming the coaxial configuration of the $Ce^{3+}–W^{6+}–Ce^{3+}$ defect, the effective charge of the $W^{6+}–Ce^{3+}$ defect dipole felt by the second Ce^{3+} ion will be reduced by ca. 25%. Importantly, this will lead to the *vanishing* of the E_h energy estimated from Fig. 3 (not shown). We conclude, therefore, that if the SP effects are present in ceria, they should probably contribute less than 66 meV to the SP hopping energy and that the $E_h \sim 66$ meV should be considered as the upper bound limit.

Next, we examine the dynamics of the BSP in ceria at low temperatures. According to a simple model of the charged point defects, the [$Ce^{3+}–M^{5+}$] defect complex (where $M=$ Nb, Ta) can be treated as an electric dipole with a fixed M^{5+} position as depicted in Fig. 4(a). In case of an ideal noninteracting dipole, in the absence of the SP effects, (i.e., no local lattice distortion), the f electron can occupy 12

Manuscript published in Physical Review B
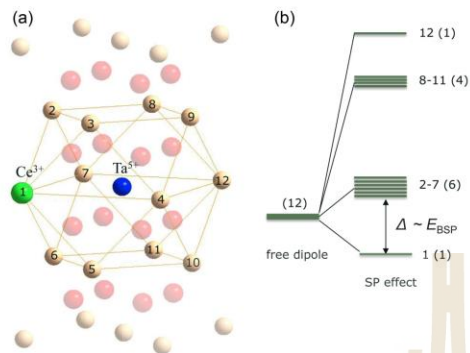
FIG. 4. (a) Schematic of the $Ce^{3+}-M^{5+}$ dipolar defect in ceria. (b) Energy diagram of the $Ce^{3+}-M^{5+}$ dipole. The degeneracy of the energy levels is indicated in the brackets.

equivalent Ce sites next to the M^{5+} donor and the energy of the "free" dipole will be 12-fold degenerate [Fig. 4(b)]. When the SP effects and dipole-dipole interactions come into play, the degeneracy will be (partially) removed as depicted in Fig. 4(b). The ground state will be separated from the first excited sixfold degenerate states by the energy $\Delta = E_{BSP}$, where E_{BSP} is the energy required to move the BSP along with the local lattice distortion from ground state 1 to one of the six equivalent neighbor Ce sites labeled as 2,3,…7 in Fig. 4(a). The next exited state is fourfold degenerate and requires the higher energy to move the BSP from site 1 to one of the four equivalent next-neighbor Ce sites labeled 8, 9 …11. in Fig. 4(a). The hopping of the f electron between the 12 Ce sites bound to the donor defect can be viewed as a reorientation (i.e., rotation) of the electric dipole which can be detected by the dielectric spectroscopy if the E_{BSP} is not too large.

The localization of the Ce $4f$ electron near the donor defect will break the local symmetry. This will be affected by the displacements of the nearby oxygens and by the displacement of the donor ion itself, which we have ignored for simplicity in Fig. 4(a). Therefore, the real energy splitting most likely will be more complex than the one proposed in Fig. 4(b). The DFT calculations reported in literature for Ce^{3+} and for PrO_2 (which is also $4f^1$ electron system) indicate that the eight neighbor oxygens shift by a different distance from the Ce^{3+} (Pr^{4+}) ion [25]. More accurate and complementary spectroscopic techniques such as low-temperature far IR and Raman, specific heat, x-ray absorption spectroscopy, may provide more clarity to this question in the future studies.

Figure 5 shows an example of the low-T dependence of the real part of the dielectric constant, ε', and dielectric loss, tan δ, for $Ce_{0.9995}Ta_{0.0005}O_2$ ceramics measured at selected ac frequencies, f, from 1 Hz to 1 MHz. In contrast to undoped CeO_2 whose ε' and tan δ shown as thick black lines in Fig. 5 are almost independent on temperature and frequency, the donor-doped ceria shows a pronounced low-T dielectric anomaly at $T < 70$ K (Fig. 5). At higher temperatures, the
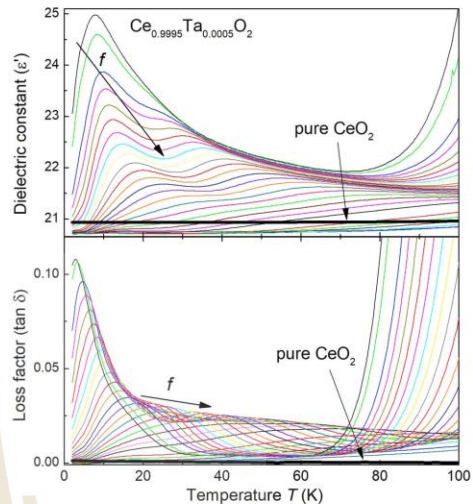
FIG. 5. Low-temperature dependence of the dielectric constant (top panel) and dielectric loss, tan δ (bottom panel) of $Ce_{0.9995}Ta_{0.0005}O_2$ ceramics measured at selected ac frequencies, f, from 1 Hz to 1 MHz. The thick solid black lines are the dielectric data for pure CeO_2 measured at 70 Hz and 100 kHz.

ε' increases dramatically due to the Maxwell-Wagner effect as a result of an increase in the SP concentration. We attribute the low-temperature $\varepsilon'(T)$ anomaly to the dielectric relaxation of the dipolar defects associated with the localized hopping of the BSP trapped next to the (donor) defect cite. Similar dielectric anomaly due to the relaxation of the BSPs is found in Nb-doped ceria. With increasing donor content, the $\Delta\varepsilon' = \varepsilon'_0 - \varepsilon'_\infty$ (where ε'_0 and ε'_∞ are the low- and high-frequency dielectric constants, respectively) in $Ce_{1-x}M_xO_2$ goes through the maximum at $x \sim 0.002$ and decreases for $x > 0.004$ (Fig. 6). The decrease in the $\Delta\varepsilon'$ at higher x is associated with the dipole-dipole interactions and disorder effects as the concentration of the defects increases.

To estimate the energy scale of the relaxation dynamics of the BSP, we follow the frequency dependence of several tan δ peaks that can be seen in Fig. 5. The frequency at which tan δ shows a maximum at $T = T_m$ is plotted as a function of $1/T$ in Fig. 7. The f vs $1/T$ dependence was fitted with the Arrhenius equation:

$$f = f_0 \exp\left(-\frac{E_a}{k_B T}\right), \qquad (5)$$

where f is the applied frequency, f_0 is the attempt frequency of the dipole reorientation, E_a is the energy barrier of the re-orientation process and T is the temperature of the tan δ maximum. The fit to Eq. (5) yields activation energies of ca. 2.73, 4.96, and 16.2 meV (Fig. 7). These are attributed to the (hopping) energies separating the BSP ground state from the several BSP excited states depicted in Fig. 4(b).

Manuscript published in Physical Review B
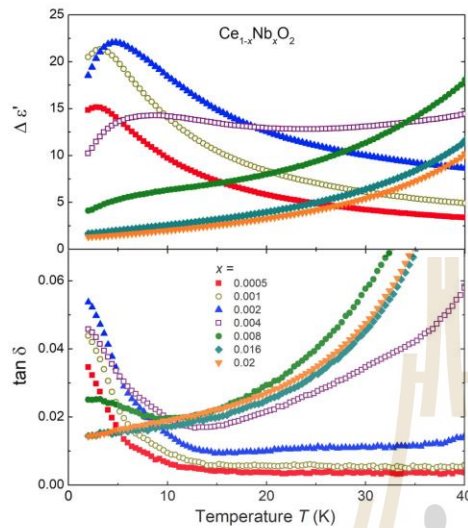
FIG. 6. Top panel: Low-temperature dependence of $\Delta\varepsilon' = \varepsilon_0'$ − ε_∞', where ε_0' was measured at 1 Hz and ε_∞' was measured at 1 MHz. (bottom panel) Dielectric loss, tan δ of $Ce_{1-x}Nb_xO_2$ ceramics measured at $f = 1$ Hz.

It is interesting that the hopping energy of the BSP (i.e., ∼3–16 meV) is significantly lower that that of the hopping energy of the itinerant SP (∼66 meV). Although the BSP and the itinerant SP will experience different local lattice environment and, therefore, will have different hopping energies, it is still somewhat surprising that the energy difference is so large. It is quite plausible that we have overestimated the hopping energy of the itinerant SP as discussed above.
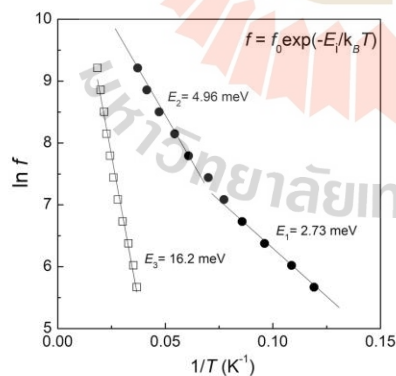

FIG. 7. Frequency dependence of the tan δ peak as a function of $1/T$ for $Ce_{0.9995}Ta_{0.0005}O_2$ ceramics.
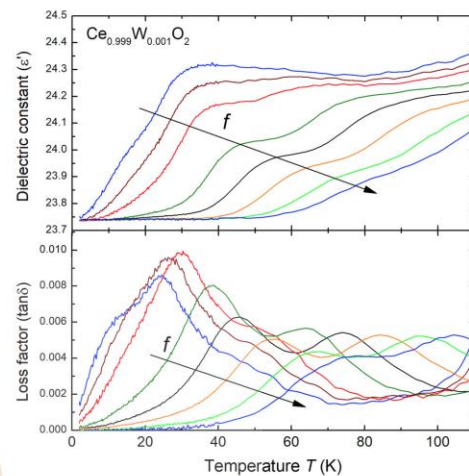
FIG. 8. Low-temperature dependence of the dielectric constant (top panel) and dielectric loss, tan δ (bottom panel) of $Ce_{0.999}W_{0.001}O_2$ ceramics measured at selected ac frequencies, f, from 4 Hz to 5 kHz.

In contrast to the Nb(Ta)-doped ceramics, the W-doped ceria demonstrates significantly weaker dielectric relaxation at low T as shown in Fig. 8. Both the ε' and tan δ anomalies in W-doped CeO_2 are more than one order of magnitude smaller than those found in Nb(Ta)-doped ceria (compare with Figs. 5 and 6). The activation energies of the series of the low-T dielectric relaxations estimated from the frequency dependence of the tan δ peaks in $Ce_{0.999}W_{0.001}O_2$ ceramics are ∼17, 27, and 62 meV; that is higher than those found in the Nb(Ta)-doped samples. A much weaker dielectric anomaly in W-doped ceria can be understood from the geometric considerations: In contrast to the Ce^{3+}–Nb^{5+} defect, the coaxial Ce^{3+}–W^{6+}–Ce^{3+} defect has zero total electric moment and, therefore, cannot contribute to the dielectric relaxation unless it adopts a noncoaxial geometry (as found in our
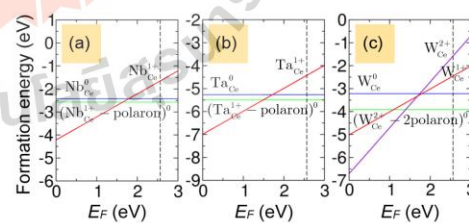

FIG. 9. Formation energies of (a) Nb_{Ce}, (b) Ta_{Ce}, and (c) W_{Ce} in different charge states as a function of Fermi level (E_F). The blue, green, red, and purple lines indicate neutral charge state M_{Ce}^0, neutral complex $(M_{Ce}^{n+} - n$ polaron$)^0$, 1+ charge state M_{Ce}^{1+}, and 2+ charge state M_{Ce}^{2+}, respectively.

Manuscript published in Physical Review B
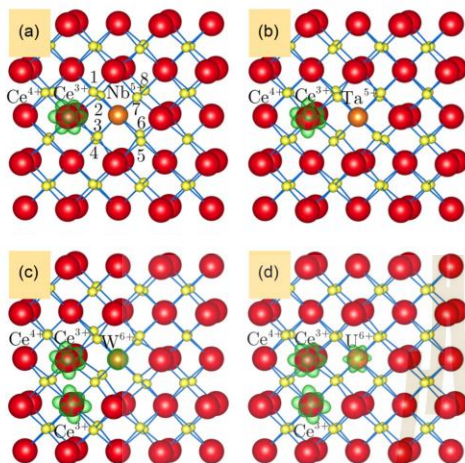
FIG. 10. Calculated spin densities of the favorable configuration of (a) $(Nb_{Ce}^{1+} - 1$ polaron$)^0$, (b) $(Ta_{Ce}^{1+} - 1$ polaron$)^0$, (c) $(W_{Ce}^{2+} - 2$ polarons$)^0$, and (d) $(U_{Ce}^{2+} - 2$ polarons$)^0$, respectively. The position of the first-nearest-neighbor O atoms surrounding the dopant M is labeled by i =1, 2, 3, ...8) as indicated in panel (a). The distance from the dopant M to O_i atom (M-O_i) is listed in Table I.

first-principles simulations). Moreover, we expect that part of the W^{6+} ions will be partially compensated by accidental acceptor impurities and oxygen interstitials, thus creating a small concentration of the W^{6+}–Ce^{3+} dipolar defects which can contribute to the weak dielectric relaxation in the W-doped CeO_2. The higher activation energies of the dipolar relaxation may be attributed to larger random fields and local lattice distortions experienced by the BSP in the W-doped CeO_2. The first-principles findings discussed below largely corroborate these experimental-based conclusions.

B. Results of the first-principles calculations

CeO_2 has experimental bandgap of 3.2 eV [26] with flat conduction bands of localized electrons [8]. The localized electrons distort the neighboring O atoms around Ce^{3+} called a SP. The calculated self-trapping energy of an excess electron in CeO_2 is −0.14 eV in our calculation (−0.30 eV in HSE06

and −0.54 eV in DFT+ U calculation as reported by Sun and coworkers [8]). The negative energy indicates that localization of an excess electron in the form of SP is favorable over delocalization state. An excess electron from any donor-type defect (such as O vacancy or donor-type dopant substituting Ce atom) can be trapped in CeO_2 in the form of SP.

The favorable defect configurations as a function of E_F for different charge states are found from the formation energy plot as shown in Fig. 9. Stable charge states for Nb_{Ce} and Ta_{Ce} are 0 and 1+ while for W_{Ce} and U_{Ce} they are 0 and 2+. The calculated band gap of CeO_2 is 2.56 eV such that it is reasonably safe to ensure that the neutral (0) charge state is favorable for n-type. In case of neutral charge state, the defect itself could be $n+$ charged while the excess electron is trapped on the nearest-neighbor Ce atom forming $[M^{n+} - nCe^{3+}]^0$ polaron defect complex having a hydrogeniclike bond as shown in Fig. 10.

For pentavalent Ta- and Nb-doped ceria, a polaron is localized on the nearest-neighbor Ce atom. For hexavalent W- and U-doped ceria, two polarons are localized on two nearest-neighbor Ce atoms which are close to each other. The $[M^{n+} - nCe^{3+}]^0$ defect complex has an electric dipole moment which will contribute to the electric polarization in doped CeO_2.

It is interesting to note that, among the studied dopant ions, W-doped ceria shows the highest self-trapping polaron energy $E^{ST} = -0.695$ eV followed by U, Ta, Nb with $E^{ST} = -0.442, -0.228$, and −0.147 eV (Table I). The SP occupies only one spin component that is the defect-induced state below conduction band as shown in Fig. 11. For Nb-, Ta-, and W-doped ceria, all eight neighboring O atoms move inward to the dopant because the dopants are slightly smaller than Ce. The bond length of M-O_i [$i = 1, 2, 3 ... 8$ as indicated in Fig. 10(a)] is distorted from 2.343 Å of pristine CeO_2 and listed in Table I. In Nb-, Ta-, and W-doped ceria, four M-O_i bonds that form a tetrahedral configuration around the dopant are obviously shorter than 2.343 Å of pristine CeO_2. This indicates a more covalent character of the four M-O_i bonds while the remaining four oxygen atoms form the dangling bonds. Our result is in good agreement with the DFT calculation of Muhich *et al.* [22]. On the other hand, U-doped ceria shows no covalent character and U tends to move toward the two Ce^{3+}. Therefore, the M-O_i bonds that share the O atom with the Ce^{3+} are shorter than the Ce^{4+}.

To compare our results with the oxidation number of referenced Ce compounds, Bader charge analysis [27,28] has been carried out and the results have been listed in Table II. The

TABLE I. Bond length of M-O_i for polarons shown in Figs. 10(a), 10(b) 10(c), and 10(d), where 1,2,3 ...8 indicates the position of the O atom as labeled in Fig. 10(a). The calculated bond length of Ce–O of pristine ceria is 2.343 Å. E^{ST} represents energy difference between polaron state and delocalized state. For Nb-, Ta-, and W-doped ceria, the four O atoms that form a tetrahedral configuration around the dopant are underlined.

| Configuration	M–O_i bond [Å]	E^{ST}
$[Nb^+ - Ce^{3+}]^0$	2.337, <u>1.978</u>, <u>1.954</u>, 2.514, 2.541, <u>2.002</u>, <u>1.979</u>, 2.462	−0.147
$[Ta^+ - Ce^{3+}]^0$	<u>1.953</u>, 2.507, 2.296, <u>1.972</u>, <u>1.972</u>, 2.446, 2.510, <u>1.993</u>	−0.228
$[W^{2+} - 2Ce^{3+}]^0$	<u>1.874</u>, 2.779, 2.170, <u>1.875</u>, <u>1.888</u>, 2.692, 2.374, <u>1.906</u>	−0.695
$[U^{2+} - 2Ce^{3+}]^0$	<u>2.198</u>, 2.242, 2.157, <u>2.198</u>, **2.238**, 2.242, 2.242, **2.239**	−0.442
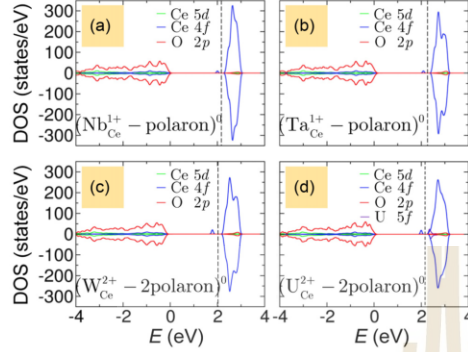
FIG. 11. Density of states (DOS) from spin-polarized calculations of (a) $(Nb_{Ce}^{1+} - 1 \, polaron)^0$, (b) $(Ta_{Ce}^{1+} - 1 \, polaron)^0$, (c) $(W_{Ce}^{2+} - 2 \, polarons)^0$, and (d) $(U_{Ce}^{2+} - 2 \, polarons)^0$, respectively. The valence band maximum is set to zero and the dashed line represents Fermi level. The localized state (small polaron) is slightly below the conduction band.

referenced cerium(III) (Ce_2O_3) and cerium(IV) (CeO_2) oxides have Bader charges of $+1.99$ and $+2.39$ $|e|$, respectively. For Nb- and Ta-doped ceria, the dopant gives an excess electron to a neighboring Ce forming a polaron as shown in Figs. 10(a) and 10(b) with the Bader charge value of $+2.14$ and $+2.16$ $|e|$, respectively, that are close to the value of cerium(III) (Ce_2O_3). In other words, the oxidation state of neighboring Ce is changed from Ce^{4+} to Ce^{3+}. With polaron formation, the Bader charge of Nb and Ta are $+2.62$ and $+2.78$ $|e|$, which is close to niobium(V) ($+2.61$ $|e|$) and tantalum(V) ($+2.72$ $|e|$) oxide, respectively. For W- and U-doped ceria, the two neighboring Ce atoms are also reduced to Ce^{3+} due to the two polarons formation as shown in Figs. 10(c) and 10(d).

TABLE II. Bader charges of the dopant M and Ce ion in donor-doped ceria and reference compounds.

Defect	M, [$|e|$]	Ce, [$|e|$]
Ce_2O_3		$+1.99$
CeO_2		$+2.39$
NbO_2	$+2.30$	
Nb_2O_5	$+2.61$	
$[Nb^+ - Ce^{3+}]^0$	$+2.62$	$+2.14$
TaO_2	$+2.34$	
Ta_2O_5	$+2.72$	
$[Ta^+ - Ce^{3+}]^0$	$+2.78$	$+2.16$
WO_2	$+2.21$	
W_2O_5	$+2.92$	
WO_3	$+2.90$	
$[W^{2+} - 2Ce^{3+}]^0$	$+2.88$	$+2.16, +2.17$
UO_2	$+2.50$	
U_2O_5	$+2.73$	
UO_3	$+3.01$	
$[U^{2+} - 2Ce^{3+}]^0$	$+2.80$	$+2.12, +2.12$

TABLE III. Binding energy of removing small polarons from the $(M_{Ce}^{n+} - n \, polaron)^0$ complex. E_b^{1st} and E_b^{2nd} stand for the binding energy of removing the first and the second polarons, respectively.

Configuration	E_b^{1st} [eV]	E_b^{2nd} [eV]
$(Nb_{Ce}^{1+} - 1 \, polaron)^0$	0.369	
$(Ta_{Ce}^{1+} - 1 \, polaron)^0$	0.516	
$(W_{Ce}^{2+} - 2 \, polarons)^0$	0.264	1.107
$(U_{Ce}^{2+} - 2 \, polarons)^0$	0.182	0.209

respectively. The W and U center becomes more positive with the value of $+2.88$ $|e|$ ($+2.90$ $|e|$ for tungsten(VI) oxide) and $+2.80$ $|e|$ ($+3.01$ $|e|$ for uranium(VI) oxide), respectively.

Interactions between SPs and the donor defect M_{Ce}^{n+} in $Ce_{1-x}M_xO_2$ are examined by calculating the binding energy that is the energy required to separate a SP from the $(M_{Ce}^{n+} - n \, polaron)^0$ complex. The binding energy of removing the first and the second SPs are given by

$$E_b^{1st} = E_{tot}\big[\big(M_{Ce}^{n+} - (n-1)polaron\big)^+\big] + E_{tot}[polaron]$$
$$- E_{tot}\big[\big(M_{Ce}^{n+} - n \, polaron\big)^0\big] - E_{tot}[bulk] \quad (6)$$

and

$$E_b^{2nd} = E_{tot}\big[\big(M_{Ce}^{n+} - (n-2)polaron\big)^{2+}\big] + E_{tot}[polaron]$$
$$- E_{tot}\big[\big(M_{Ce}^{n+} - (n-1)polaron\big)^+\big] - E_{tot}[bulk], \quad (7)$$

respectively, where $E_{tot}[(M_{Ce}^{n+} - n \, polaron)^0]$ is the total energy of the supercell containing $(M_{Ce}^{n+} - n \, polaron)^0$ complex ($n = 1$ for Nb and Ta, $n = 2$ for W and U), $E_{tot}[(M_{Ce}^{n+} - (n-1)polaron)^+]$ is the total energy of the supercell containing $(M_{Ce}^{n+} - (n-1)polaron)^+$ complex, $E_{tot}[(M_{Ce}^{n+} - (n-2)polaron)^{2+}]$ is the total energy of the supercell containing $(M_{Ce}^{n+} - (n-2)polaron)^{2+}$ complex, $E_{tot}[bulk]$ is the total energy of the perfect bulk supercell and $E_{tot}[polaron]$ is the total energy of an isolated SP. The results of the calculated binding energies are shown in Table III indicating that SPs are strongly bound to the M_{Ce}^{n+} defect. We found that removing the second polaron from $(W_{Ce}^{2+} - 2 \, polaron)^0$ and $(U_{Ce}^{2+} - 2 \, polaron)^0$ complexes requires more energy than removing the first one.

In general, the first-principles simulations are in qualitative agreement with our experimental findings. For Nb- and Ta-doped ceria, the f electron is localized on the nearest Ce site to the donor ion. In case of W- and U-doped ceria, the two Ce^{3+} ions are found on the nearest and next-nearest sites to the donor defect but they do not form a coaxial $Ce^{3+} - M^{6+} - Ce^{3+}$ defect complex as was intuitively suggested based on our low-T dielectric data. The energy scale of the BSP binding energy to the donor defect is of the same order of magnitude as the one estimated from the experimental data. However, the large difference in the E_b^{1st} values for Nb- and Ta-doped CeO_2 (Table III) is not supported by the experimental data (Fig. 3). The origin of the large discrepancy with the experimental data may be too small of a supercell used in our DFT simulations and/or the type of the electron correlation functional employed. For example, Sun *et al.* reported much smaller values

Manuscript published in Physical Review B

of the BSP binding energy to the oxygen vacancy obtained by the hybrid functional-based first-principles simulations [8].

IV. CONCLUSIONS

Early reports on the electron transport of donor-doped and partially reduced ceria have shaped a solid opinion that the f electron localization in CeO_2 is driven by the electron-phonon interactions in the form of SPs [29–31]. Since then, n-type CeO_2 has become (and still remains) a textbook example of the SP model in metal oxides with the number of the first-principles simulations far exceeding the experimental reports.

More recent experimental and simulation reports on ceria suggest that the Anderson localization caused by defects and random fields has been overlooked [6,8,32]. The experimental findings that do not fit with the SP scenario are the absence of the SP "overcrowding" effect [6,33] a very large scatter in the activation energy of the electrical conductivity [6,34–36], a strong dependence of the activation energy on the type of the donor defect, and other impurities [32,37,38], an absence of the correlation between the SP binding energy and the SP optical absorption band [6,32].

Both the experimental data and the first-principles simulations confirm the localized nature of the charge carriers in the donor-doped ceria [39–41]. We argue, however, that in contrast to the SP scenario, the main driving force for the localization in the real-case ceria is the Anderson localization stemming from the random fields and strong Coulomb interaction between the f electrons and the (donor) defects.

Probably one of the most important results of this study is the very low activation energy of the BSP dynamics in ceria as revealed by the low-T dielectric spectroscopy. It appears that the "hopping" energy of the SP bound to the donor defect is more than an order of magnitude smaller than the binding energy of the $Ce^{3+}-M^{5+/6+}$ defect complex. This may indicate that the SP effects in ceria are an order of magnitude weaker than previously thought. We hope that these experimental findings will be taken as a reference standard for more refined and accurate first-principles simulations of electron localization in ceria.

[1] P. W. Anderson, Phys. Rev. **109**, 1492 (1959).

[2] P. K. Gosh and W. E. Spear, J. Phys. C **1**, 1347 (1968).

[3] T. Holstein, Ann. Phys. **8**, 343 (1959).

[4] S. D. Kang, M. Dylla, and G. J. Snyder, Phys. Rev. B **97**, 235201 (2018).

[5] H. L. Tuller and A. S. Nowick, J. Phys. Chem. Solids **38**, 859 (1977).

[6] T. Kolodiazhnyi, T. Charoonsuk, Y.-S. Seo, S. Chang, N. Vittayakorn, and J. Hwang, Phys. Rev. B **95**, 045203 (2017).

[7] P. W. Anderson, Nature (London) Phys. Sci. **235**, 163 (1972).

[8] L. Sun, X. Huang, L. Wang, and A. Janotti, Phys. Rev. B **95**, 245101 (2017).

[9] T. Kolodiazhnyi, H. Sakurai, A. A. Belik, and O. V. Gornostaeva, Acta Mater. **113**, 116 (2016).

[10] G. Kresse and J. Hafner, Phys. Rev. B **48**, 13115 (1993).

[11] D. Sanchez-Portal, E. Artacho, and J. M. Soler, Solid State Commun. **95**, 685 (1995).

[12] W. Kohn and L. J. Sham, Phys. Rev. **140**, A1133 (1965).

[13] F. Fuchs, J. Furthmüller, F. Bechstedt, M. Shishkin, and G. Kresse, Phys. Rev. B **76**, 115109 (2007).

[14] P. E. Blöchl, Phys. Rev. B **50**, 17953 (1994).

[15] G. Kresse and D. Joubert, Phys. Rev. B **59**, 1758 (1999).

[16] J. P. Perdew, K. Burke, and M. Ernzerhof, Phys. Rev. Lett. **77**, 3865 (1996).

[17] J. Hubbard, Proc. R. Soc. London. Series A. Math. Phys. Sci. **276**, 238 (1963).

[18] C. G. Van De Walle and J. Neugebauer, J. Appl. Phys. **95**, 3851 (2004).

[19] T. Kolodiazhnyi, H. Sakurai, M. Avdeev, T. Charoonsuk, K. V. Lamonova, Yu. G. Pashkevich, B. J. Kennedy, Phys. Rev. B **98**, 054423 (2018).

[20] A. Janotti, J. B. Varley, M. Choi, and C. G. Van de Walle, Phys. Rev. B **90**, 085202 (2014).

[21] A. Janotti and C. G. Van de Walle, Phys. Rev. B **76**, 165202 (2007).

[22] C. Muhich and A. Steinfeld, J. Mater. Chem. A **5**, 15578 (2017).

[23] T. Zacherle, A. Schriever, R. A. De Souza, and M. Martin, Phys. Rev. B **87**, 134104 (2013).

[24] T. G. Stratton and H. L. Tuller, J. Chem. Soc. Faraday Trans. **83**, 1143 (1987).

[25] C. H. Gardiner, A. T. Boothroyd, P. Pattison, M. J. McKelvy, G. J. McIntyre, and S. J. S. Lister, Phys. Rev. B **70**, 024415 (2004).

[26] Z. C. Orel and B. Orel, Phys. Status Solidi B **186**, K33 (1994).

[27] D. A. Andersson, S. I. Simak, N. V. Skorodumova, I. A. Abrikosov, and B. Johansson, Phys. Rev. B **76**, 174119 (2007).

[28] G. Balducci, J. Kaspar, P. Fornasiero, M. Graziani, M. S. Islam, and J. D. Gale, J. Phys. Chem. B **101**, 1750 (1997).

[29] I. K. Naik and T. Y. Tien, J. Phys. Chem. Solids **39**, 311 (1978).

[30] I. K. Naik and T. Y. Tien, J. Electrochem. Soc. **126**, 562 (1979).

[31] H. L. Tuller and A. S. Nowick, J. Electrochem. Soc. **126**, 209 (1979).

[32] T. Charoonsuk, N. Vittayakorn, and T. Kolodiazhnyi, J. Appl. Phys. **123**, 165704 (2018).

[33] E. K. H. Salje, Polarons and bipolarons in WO_{3-x} and $YBa_2Cu_3O_7$, in *Polarons and Bipolarons in High-T_C Superconductors and Related Materials*, edited by E. K. H. Salje, A. S. Alexandrov, and W. Y. Liang (Cambridge University Press, Cambridge, 1995).

[34] M. C. Göbel, G. Gregori, and J. Maier, Solid State Ionics **215**, 45 (2012).

[35] R. N. Blumenthal and R. L. Hofmaier, J. Electrochem Soc. **121**, 126 (1974).

Manuscript published in Physical Review B

[36] R. N. Blumenthal and R. K. Sharma, J. Solid State Chem. **13**, 360 (1975).

[37] M. R. De Guire, M. J. Shingler, and E. Dincer, Solid State Ionics **52**, 155 (1992).

[38] P. V. Ananthapadmanabhan, S. B. Menon, D. S. Patil, and N. Venkatramani, J. Mat. Sci. Lett. **11**, 501 (1992).

[39] M. Nakayama, H. Ohshima, M. Nogami, and M. Martin, Phys. Chem. Chem. Phys. **14**, 6079 (2012).

[40] E. Shoko, M. F. Smith, and R. H. McKenzie, J. Phys. Chem. Solids **72**, 1482 (2011).

[41] J. J. Plata, A. M. Marquez, and J. F. Sanz, J. Phys. Chem. C **117**, 14502 (2013).
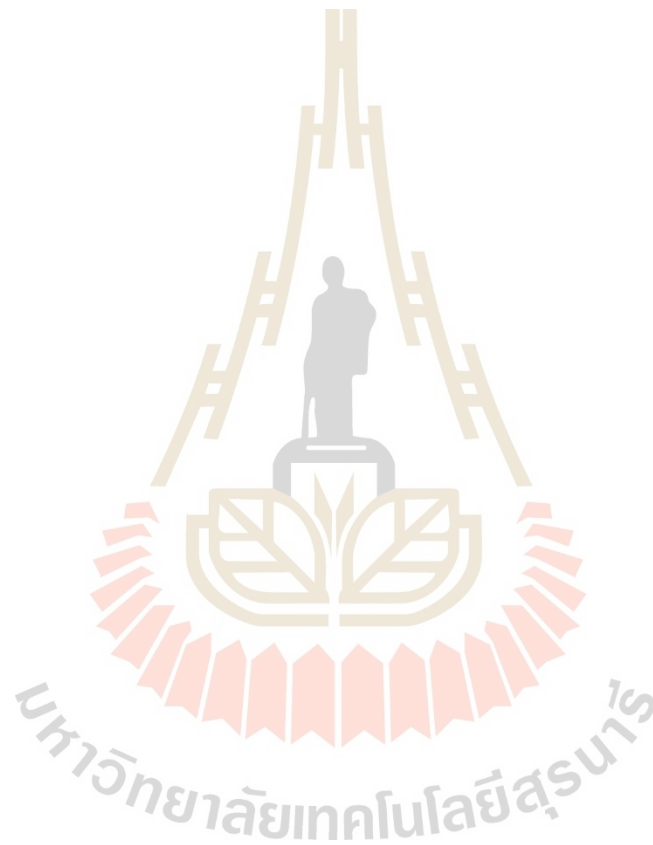
Manuscript published in ACS OMEGA

Article

Effects of the van der Waals Interactions on Structural and Electronic Properties of CH₃NH₃(Pb,Sn)(I,Br,Cl)₃ Halide Perovskites

Narasak Pandech, Thanundon Kongnok, Nirawith Palakawong, Sukit Limpijumnong, Walter R. L. Lambrecht, and Sirichok Jungthawan*

Cite This: *ACS Omega* 2020, 5, 25723−25732

Read Online

ACCESS | Metrics & More | Article Recommendations | Supporting Information

ABSTRACT: In hybrid perovskite materials like $CH_3NH_3PbI_3$, methylammonium (MA) lead iodide (MAPI), the orientation of the MA^+ cations and their ordering can significantly affect the structure of the inorganic framework. Although the states near the band edges are known to be primarily derived from the Pb and halogen orbitals rather than from the organic ion, the latter may have an indirect effect through their impact on the structural relaxation. In this work, we investigate both the structural relaxation effects of the inorganic framework in response to the MA^+ orientation and their impact on the electronic structure near the band edges. Calculations are performed for $MA(Pb,Sn)X_3$ with (X = I, Br, and Cl) materials for both Pb- and Sn-based compounds. The work focuses on the high-temperature α-phase, which is nominally cubic if averaged over all possible MA orientations and in which no alternating rotations of the octahedral occur, so that the unit cell is the smallest possible. The effects of van der Waals (vdW) corrections to density functional theory on the structural relaxation are investigated. Our results reveal that the vdW interactions between the MA^+ cation and the inorganic framework can strongly affect the optimized orientation and position of the molecule and the resulting distortion of the inorganic framework. Consequently, it also affects the electronic properties of the materials and specifically can change the band structure from direct to indirect band gaps. The robustness of this result is studied by comparing hybrid functional calculations and quasiparticle self-consistent GW calculations as well as spin−orbit coupling.
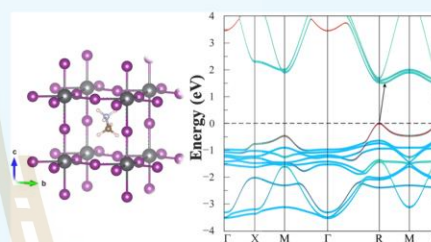
■ INTRODUCTION

Perovskites are crystalline materials with an ABX_3 structure similar to the $CaTiO_3$ mineral. The A-site cations are 12-fold coordinated, and divalent B-site cations are 6-fold coordinated. In the class of organic−inorganic halide perovskite materials, the A-site is a monovalent organic cation, for example, methylammonium ($CH_3NH_3^+$, MA^+), the B-site is a divalent metal, for example, Pb^{2+}, Sn^{2+}, Ge^{2+}, and the X-site is occupied by the halogen ions, for example, I^-, Br^-, and Cl^-. Recently, hybrid halide perovskite materials have emerged as new promising materials in photovoltaic applications. This class of materials has been known for a long time and has been studied in relation to their very particular dielectric properties.[1] However, the first application of organo-halide perovskite materials in photovoltaics can be traced back to 2009, with the work of Kojima and co-workers.[2] After the pioneering work, the number of applications of the hybrid perovskite in photovoltaics rapidly increased, especially in the case of lead-halide perovskite materials.[3−5] Notably, the solar cell efficiencies of halide perovskites have remarkably risen to about 20% such that they are a good alternative to Si solar cells.[6−8] However, their stability and structural transformations remain a challenge.

The crystal structures of Pb- and Sn-based halide perovskite materials are temperature-dependent. Their exact structures are still under dispute because of the complexity introduced by the MA^+ cation group. Experimentally, many research groups have attempted to identify the structures of the materials using neutron powder diffraction and also synchrotron X-ray powder diffraction.[5,9] At high temperature, the α-structure is cubic (with the space group $Pm\bar{3}m$ if the molecular orientations are ignored or MA is replaced by a symmetric Cs ion). However, the Pb or Sn ferroelectric displacement in its octahedron or the MA in-phase orientation can lead to a non-centrosymmetric tetragonal $P4mm$ space group.[3] The β-phase occurs by alternatingly tilting the octahedra clock and counterclockwise

Manuscript published in ACS OMEGA

about a single axis, thereby doubling the unit cell to a $\sqrt{2} \times \sqrt{2} \times 1$ cell and making the system tetragonal. In CsSnI$_3$, this leads to the $P4/mbm$ group because the tilts are in phase in the c-direction. However, with the additional ferroelectric symmetry breaking of the MA ions, the space group becomes $I4cm$.[3] Others however assigned the $I4/mcm$ spacegroup[5] to this phase in MAPbI$_3$. This phase occurs in SrTiO$_3$ where it also exhibits rotation of the octahedra about the z-axis but which alternates between clockwise and counterclockwise along the c-axis, thereby doubling the cell again to $\sqrt{2} \times \sqrt{2} \times 2$. On the other hand, the $I4/mcm$ phase which does maintain an inversion symmetry could also result from alternating the MA dipole orientations.[10] The transition temperature to this phase depends on the material and occurs at ~180 K in MAPbI$_3$[5] and 200 K in MASnI$_3$.[3] Finally, a second transition occurs at a lower temperature to an orthorhombic γ-phase in which octahedral tilts occur about two orthogonal axes, and the cell is doubled in the c-direction. The full space group determination in this phase has not been achieved for the different organic ions but is $Pnma$ in the case of the symmetric A ion and is thus assumed to be derived from this phase.[5] In MAPbI$_3$, this transition occurs between 100 and 150 K,[5] while for the Sn case, it occurs closer to 100 K.[3] In the low-temperature structure, the BX_6 octahedra are strongly deformed and restrict the rotational motion of MA$^+$ cations.[5] In this case, the organic cations are fully ordered and pinned and can rotate only along the C–N axis.[5,9] When the temperature increases, tetragonal and cubic structures appear. In the high-temperature structures, the organic cations become free to rotate inside the dodecahedral cages, and they are disordered.[5,9] Nuclear magnetic resonance measurements[11] have shown that the probable location of the MA cations cannot be determined in the cubic phase, and the reorientation time of the MA cations is in the order of picoseconds. Therefore, the presence of organic molecules and their mobility are a challenge in the study of these types of materials.

In organic–inorganic halide perovskite materials, the MA-cation groups reside within the network of corner-sharing BX_6 octahedra and are stabilized by van der Waals (vdW) interactions. Some previous theoretical works[12–15] have already revealed the importance of the presence of dispersive forces in these types of materials on structural properties. The effect of the MA orientations on the electronic structure is less clear. Because the states near the band edges are either Pb-s, I-p mixed at the valence band maximum (VBM) or Pb-p like at the conduction band minimum (CBM), one may think that the MA has little effect on them. On the other hand, the MA orientations can affect the overall symmetry and this may lead to splitting of the CBM.

In this work, we conducted vdW-corrected density functional theory (DFT) calculations to examine the importance of vdW interactions on the MA-cation structural parameters and consequently to examine the electronic properties of the MABX_3 (B = Pb, Sn; X = I, Br, Cl) halide perovskite materials. Our results reveal that the inclusion of the vdW interactions in DFT calculations affects the MA-cation orientation, which influences the structural properties of the inorganic network and consequently affects the electronic properties of the materials. Because the Perdew–Burke–Ernzerhof (PBE) and even vdW-corrected DFT can significantly underestimate the gap, we also conduct calculations of the same structures using the quasiparticle self-consistent GW (QSGW) method. Finally,

spin–orbit coupling (SOC) is known to be important in particular in the Pb-based compounds. Thus, we study the effect of both GW self-energy corrections and SOC on the electronic structure in relation to the orientation of the MA molecules and their corresponding induced structural distortions. The SOC in combination with the electric field-induced symmetry breaking arising from the dipolar molecules leads to the Rashba effect, which can affect the location of CBM in k-space.

■ RESULTS AND DISCUSSION

Structural Relaxation. Before we go into our calculated results, we want to refer to two previous studies of the molecular orientations in the cubic phase of MAPbI$_3$ that are particularly relevant to our study. Motta et al.[16] performed a full structural optimization of MAPbI$_3$ within generalized gradient approximations (GGAs) including vdW corrections. It has been found that the results are sensitive to the initial orientation of the molecule being along [100] or [111]. In the former case, the molecule rotates toward a [110] or equivalent direction, while in the latter case, it remains in the [111] direction. Both the [110] and [111] orientations thus appear to be the favored orientations. We here extend that approach to the other halogens and to the case of Sn instead of Pb. Bechtel et al.,[17] on the other hand, took a more systematic approach for mapping out the energy landscape. They define all possible rotation degrees of freedom of the molecule, defined by a polar angle θ and azimuthal angle ϕ of the C–N axis of the molecule versus the [001] and [100] cubic axes, the rotation angle α of the molecule about its own axis, and the displacement of the molecule from its center along its own axis. They then map out the energy of the molecule as a function of these variables but while keeping the inorganic framework fixed. They found that the molecule translates along its own direction away from the nominal center of the dodecahedral site, in other words, the displacement of the molecule is important. The favored orientations found in this work are close [100] and [111] directions. Consequently, the initial orientation of the molecule for structural relaxations is either [100], [110], or [111] direction. The molecule and the framework are fully allowed to relax. Subsequently, we also performed calculations with constraint where the position of the molecule is kept at some angle as in the energy landscape studies of Bechtel et al.,[17] but the inorganic framework is allowed to fully relax along with the possible displacement of the molecule relative to the framework. All of these calculations were then performed with and without vdW corrections to ascertain their importance. After discussing the structural results, we will then examine their effect on the electronic band structure in the next section. Ferroelectric ordering was found to be slightly preferable energetically by Quarti et al.[10] On the other hand, Weller et al.[5] indicate the disordered alternating non-polar orientation of the MA molecules.

Let us start the discussion by presenting the relaxed crystal geometries. Initially, the structural optimizations have been performed at the level of the GGA–PBE calculations with and without including the vdW interactions for revealing the effects of internal interactions between the organic cation and the BX_6 inorganic framework. We perform a full structural relaxation without any symmetry constraints from the ideal cubic perovskite structure with staggered H-atoms arrangement (the H-atoms on the C-end and on the N-end are not aligned

with each other but rotated with respect to each other by 60°) adopted from Motta et al.'s calculation,[16] as depicted in Figure 1. The relaxations have been performed with various initial
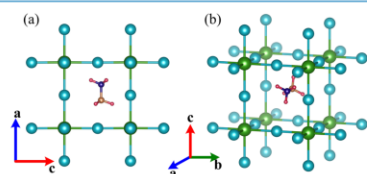
**Figure 1.** Illustration of the ideal cubic structure of $CH_3NH_3BX_3$ with staggered H-atoms arrangement in CH_3NH_3 molecule which is oriented along the [100] direction viewed along (a) b-crystallographic axis and (b) arbitrary crystallographic axis. Green, cyan, blue, orange, and red spheres represent the B-site atoms, X-site atoms, N-atoms, C-atoms, and H-atoms, respectively.

configurations of the MA cation, namely, oriented along the [100], [110], or [111] directions, as listed in Table 1. We note that the relaxation process is extremely sensitive to the initial MA-cation orientation. For example, when we started the relaxation with the MA^+ cation oriented along the [111] direction, the relaxed structure preserves its original MA^+ cation orientation in both cases of with and without including vdW interactions, as depicted in Figure 2c,d, respectively. This result is similar to that of Motta et al.[16] The calculated change in angle $(\Delta\theta)$ of the C−N axis with respect to its initial orientation direction is very small, as shown in Table 1. In contrast, if we start the structural relaxation with the MA^+ cation oriented along the [100] direction, the relaxed structure does not preserve its original MA^+ cation orientation, instead, it may end up with the MA^+ cation orientated along the [10−
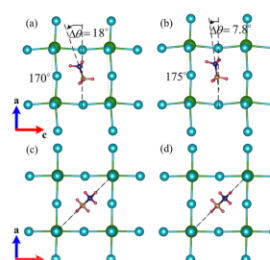

Figure 2. Illustration of relaxed structures of the cubic $CH_3NH_3PbI_3$ with and without vdW interactions (left and right panels, respectively) for different orientations of the MA^+ cation. (a,b) Relaxed structure of the MA cation initially oriented along the [100] direction. (c,d) Relaxed structure of the MA cation initially oriented along the [111] direction. The pictures are viewed along the y-axis or showing the x−z plane.

1] direction, as depicted in Figure 2a,b. The reason why particularly the [10−1] direction is favored as opposed to the in-principle equivalent [1±10] or [101] depends on the particular chosen orientation of the molecule about its own axis. As we will show later, the H atoms are in such positions to favor rotating in this particular direction by optimizing the hydrogen bonds with the halogen. This is why the vdW interactions are important in the structural optimization of these types of materials. In this case, the MA^+ cation shifts down along the x−z plane (see the inset of Figure 3) with the change in angle, $(\Delta\theta)$ around 18° (in the case of MAPbI$_3$) when including the vdW interaction, as shown in Table 1. However, if one does not include the vdW interaction in the calculation, the calculated $\Delta\theta$ in this case is around 7.8° and

Table 1. Calculated Lattice Constants a, b, and c (Å), Unit Cell Volume V (Å^3), Deviate Angle from the Given Initial MA Orientation, $\Delta\theta$ (in Degree), Relative Energy (Rel. Energy, in meV), B−X−B Bond Angle (in Degree), and Hydrogen Bond Length (Å) of MABX_3,[a]

compounds	int. MA orient.	rel. energy	$\Delta\theta$	a	b	c	V	B−X−B bond angle	H_N−X	H_C−X
					calculated structural parameters				H-bonding	
MAPbI$_3$	[100]	0.00	18 (7.8)	6.34 (6.48)	6.30 (6.43)	6.38 (6.49)	254.7 (270.2)	169.5 (174)	2.72 (2.8)	3.36 (3.6)
	[110]	14.4	9 (5.6)	6.34 (6.48)	6.40 (6.57)	6.27 (6.32)	252 (270.4)	175 (175)	2.75 (2.8)	3.40 (3.6)
	[111]	21.0	0.9 (0.5)	6.34 (6.47)	6.34 (6.47)	6.34 (6.47)	255.3 (270.4)	178 (178)	2.71 (2.7)	3.38 (3.6)
MAPbBr$_3$	[100]	0.00	23 (12.7)	5.94 (6.03)	5.89 (6.03)	6.03 (6.13)	211 (222.8)	169.1 (172)	2.45 (2.5)	3.31 (3.4)
	[110]	18.6	6.8 (4.6)	5.98 (6.08)	5.98 (6.08)	5.89 (6.03)	209.8 (221)	174 (173)	2.55 (2.5)	3.50 (3.5)
	[111]	35.4	0.9 (1.2)	5.97 (6.08)	5.97 (6.08)	5.97 (6.08)	212.7 (223.4)	177 (177)	2.41 (2.5)	3.10 (3.5)
MAPbCl$_3$	[100]	0.00	26 (17.5)	5.67 (5.74)	5.63 (5.73)	5.79 (5.90)	184.7 (193.8)	168 (171)	2.3 (2.4)	3.17 (3.2)
	[110]	23.1	6.6 (4.6)	5.73 (5.83)	5.73 (5.83)	5.63 (5.73)	184.2 (193.9)	174 (174)	2.3 (2.4)	3.3 (3.2)
	[111]	46.4	0.8 (1.3)	5.73 (5.83)	5.73 (5.83)	5.73 (5.83)	187.6 (197.2)	175 (176)	2.3 (2.4)	2.9 (3.2)
MASnI$_3$	[100]	0.00	20.1	6.26	6.19	2.27	243	172	2.7	3.3
	[110]	6.4	8.5	6.26	6.26	6.17	241.3	174	2.8	3.4
	[111]	20.3	0.01	6.24	6.24	6.24	243.4	177.4	2.7	3.3
MASnBr$_3$	[100]	0.00	26.5	5.89	5.80	5.95	202.9	170.6	2.43	3.2
	[110]	9.00	8.6	5.91	5.91	5.80	201.6	171	2.45	3.1
	[111]	34.6	0.03	5.88	5.79	5.95	204.5	176	2.47	3.05
MASnCl$_3$	[100]	0.00	28.4	5.72	5.55	5.75	182.6	171	2.25	2.89
	[110]	8.92	4.6	5.71	5.71	5.54	179.2	172	2.25	2.86
	[111]	33.17	0.03	5.70	5.70	5.70	185.4	176	2.26	2.85

[a]The numbers in parenthesis are obtained without including vdW.

Manuscript published in ACS OMEGA
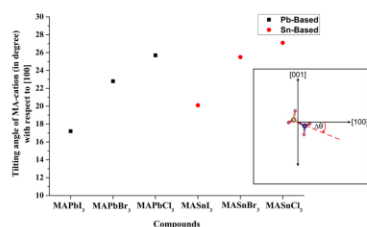
Figure 3. vdW-calculated tilting angle of the MA cation with respect to the initial [100] orientation ($\Delta\theta$), as represented in an inserted picture.

the relaxed structure is less distorted, as shown in Figure 2b. Including the vdW interaction, the calculated $\Delta\theta$ of the C−N axis with respect to the [100] direction increases when the halogen atom is changed from I$^-$ to Br$^-$ to Cl$^-$ in both Pb- and Sn-based cases, as shown in Figure 3. The increase of the angle indicates a stronger interaction between the organic MA$^+$ cation and the BX_6 inorganic framework and causes the relaxed structure to become more distorted, as indicated by a B−X−B bond angle tabulated in Table 1. The calculated lattice parameters, when including the vdW interaction, are in very good agreement with the experimental values, with an error less than 1%. If the calculation does not include the vdW interaction, the calculated lattice parameters are larger than the experimental values by an error more than 3%. The calculated lattice constants of the MAPbX_3 (X = I, Br, and Cl) with vdW-included are 6.34, 5.96, and 5.71 Å which are in good agreement with the experimental values of 6.33, 5.90, and 5.67 Å, respectively.[1] For the MASnX_3 (X = I, Br, and Cl), the calculated lattice constants with vdW-included are 6.25, 5.89, and 5.68 Å, which are also in good agreement with the experimental values of 6.23, 5.88, and 5.67 Å, respectively.[3,18]

If we focus on the relaxed structures, the significant difference between these structures is the deformation of the BX_6 octahedra. In the case of initial [100] orientation, the relaxation of the MA$^+$ cation induces the deformation and the symmetry reduction of the inorganic BX_6 octahedra. Such distortion causes the B−X−B bonds to not lie parallel to the crystal directions but instead be slightly tilted by ∼10° from the ideal cubic structure when the vdW interaction is included (see Table 1). However, when excluding vdW interactions, they only tilted by ∼5° from the ideal cubic structure. In the case of [111] orientation, the B−X−B bond angles are very close to 180°, indicating that the relaxed structure preserves a high symmetry cubic structure. In this case, the relaxed structure of the [111] orientation is still simple cubic (see Table 1). In contrast, the relaxed structure of the initial [100] orientation becomes tetragonal ($c/a \neq 1$).

Additionally, the hydrogen bond lengths were calculated and are listed in Table 1. The results show that the hydrogen atoms on the NH$_3$-side are closer to the BX_6 inorganic framework than those of the CH$_3$-side. It can be implied that the hydrogen atoms in NH$_3$-side dominate the strong interaction with the BX_6 inorganic framework. Although the relaxed structure is sensitive to the initial MA$^+$ cation configuration, it is worth noting that the energy difference between these configurations is very small. The energy difference is calculated to be in the 21−50 meV range in favor of a direction near the [10−1] direction (tilted from [100] by $\Delta\theta \sim 18°$ in the case of MAPbI$_3$), which is consistent to the previous studies of MAPbI$_3$.[16,17] The lowest energy structure we found (MAPbI$_3$ case) is consistent with the lowest energy structure calculated by Qiaoling Xu et al.[19] using $2 \times 2 \times 2$ supercell calculations, the MA cations are found in favored orientation to the [012] direction with the relative energy of ∼60 meV per formula unit. Indeed, it can be implied that these MA$^+$ cation configurations represent the local energy minima.

After the full structural relaxation of the initial [100] orientation has been carried out, it is still unclear why the MA$^+$ cation rotated downward in the x−z plane instead of other
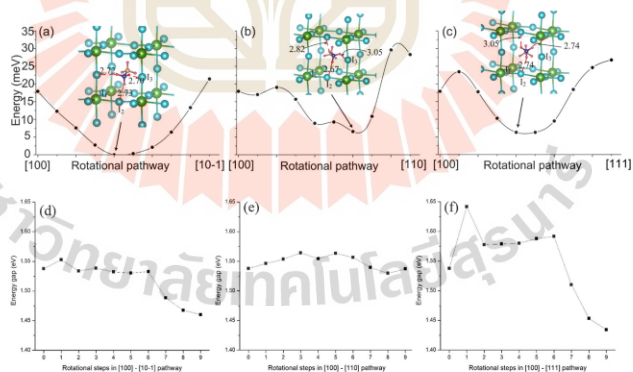
Figure 4. (a−c) Calculated relative energy and (d−f) variation of the band gap, for MAPbI$_3$ case, as a function of the rotational pathway of the C−N axis with respect to the [100] direction. (a,d) [100] → [10−1], (b,e) [100] → [110], and (c,f) [100] → [111]. The C−N atoms are fixed at each rotational angle, while the other atoms are allowed to relax. The inserts show the orientation and the hydrogen bond lengths (red dashed lines) that can be formed with the nearest halogen atoms near the minimum configuration.

Manuscript published in ACS OMEGA

directions. Therefore, we have chosen the MAPbI$_3$ case as an example for further study. We performed the ground state energy calculation as a function of the rotational angle of the C−N axis with respect to the [100] direction, including the vdW interactions. Several pathways, namely, [100] → [10−1], [100] → [110], and [100] → [111] are considered. In the calculations, the staggered H-atoms arrangement is applied, the C−N axis and C−N bond length are fixed at each rotational angle while the other atoms and cell volume are allowed to relax. The calculated energies as a function of rotational angle in different pathways are depicted in Figure 4. From the plot, we can see that the calculated energies in the [100] → [10−1] pathway decrease until the rotational angle is around 20° and then the energy increases. This is consistent with the full unconstrained minimization presented above. At the lowest energy structure, three hydrogen atoms in NH$_3$-side bond with I$^-$ atoms almost equally, as depicted in Figure 4a. The energy difference between [100] and [10−1] orientations is very small, 3.5 meV. On the other hand, the calculated energies in the [100] → [110] pathway slightly fluctuate with the rotational angle and end up with the energy 10 meV higher than that of the [100] orientation. In this case, at the lowest energy point, one of the hydrogen atom in NH$_3$-side bonds with the I$^-$ atom stronger than other two hydrogen atoms, as depicted in Figure 4b. In the case of the [100] → [111] pathway, the calculated energy slightly increases and then decreases until the rotational angle is around 22°, then increase and end up with the energy 9 meV higher than that of the [100] orientation. In this case, at the lowest energy structure, two of hydrogen atoms on the NH$_3$-side present stronger bonds with the I$^-$ atoms than the other hydrogen atom, as depicted in Figure 4c. The lowest energies along the [100] → [110] and [100] → [111] pathways are ~7 meV higher than along the [100] → [10−1] pathway. In addition, we can see that the energy difference in the 15−25° range of the [100] → [10−1] pathway is very shallow, indicating several local minima around that point. The difference in these different pathways lies in the way that the molecule's H-atoms are positioned relative to the halogen atoms along these paths. The more complex behavior for other than the optimal rotation pathway (a) shows that there is some optimal orientation of the molecule about its own axis such that it best optimizes the H bonds with the halogens.

From our calculated ground state energies in different pathways, we conclude that the fully structural relaxation process of the initial [100] orientation with the given staggered H-atoms arrangement, including the vdW interaction, ends up with the MA$^+$ cation rotated downward in the x−z plane from [100] toward [10−1] in a local minimum energy near the [10−1] direction with the deviate angle, $\Delta\theta$, listed in Table 1.

Electronic Properties. The significant differences in the structural geometries are expected to impact on the electronic structure of the studied MABX$_3$. First, let us pick MAPbI$_3$ as an example to explain the effect of the vdW interaction on the electronic properties of the studied materials. The electronic band structures along the high symmetry points of the Brillouin zone calculated by using the GGA−PBE without SOC with different MA$^+$ cation orientations of the MAPbI$_3$ are depicted in Figure 5. Our GGA−PBE calculated band structures reveal that the orientations of the MA$^+$ cation have a profound impact on the nature of the band gap of MAPbI$_3$. In the case of the [111] orientation, the relaxed structure keeps the high symmetry of the cubic structure and
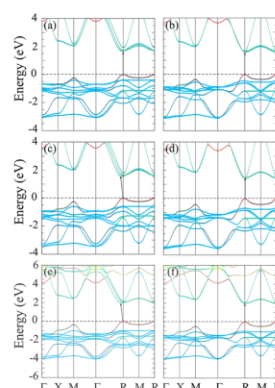

Figure 5. Calculated band structures without SOC of the CH$_3$NH$_3$PbI$_3$ for (a,b) PBE without including vdW, (c,d) PBE with including vdW, and (e,f) Heyd−Scuseria−Ernzerhof (HSE) with including vdW. Left and right panels represent the MA$^+$ cation initially orientated along [100] and [111] directions. The red, skyblue, and lime colors of each band represent the spd-projected wavefunction character of s, p, and d orbitals, respectively. The calculated VBM energies were shifted to zero.

gives the direct band gap at the R-point (0.5, 0.5, 0.5) of the Brillouin zone both with and without vdW interactions, as depicted in Figure 5b,d. On the other hand, in the case of the initial [100] orientation, the relaxed structures are strongly distorted due to the cation rotation and consequently affect the band structure: the CMB shifts along the $R \to \Gamma$ line, the band gap becomes indirect, as depicted in Figure 5c. These results are in good agreement with Motta et al.[16] Please note that the Grimme DFT-D3 approach changes the total energy and hence relaxation but not the exchange correlation potential used for the band structure calculations. In the case of exclusion of vdW interactions, the calculated band gap remains direct for both [100] and [111] orientations, as depicted in Figure 5a,b, respectively. This indicates that the relaxed structures do not present enough distortion to modify the band structure significantly, and the vdW correction is necessary for the structural relaxation of the halide perovskite systems.

The vdW-calculated band gap without SOC of MAPbI$_3$ lies in the 1.45−1.55 eV (see Table 2) range close to the experimental value of about 1.55 eV,[2,20] while the calculated band gap without vdW-interaction lies in 1.6−1.7 eV, slightly larger than the experimental values. The GGA−PBE calculations usually underestimate the band gap of semiconductors. However, as already shown in the case of MAPbI$_3$,[21] the agreement here is due to a fortuitous cancellation of the errors of the GGA underestimated band gap and the lack of spin−orbit interactions which would tend to overestimate the gap. To test the robustness of the indirect band gap, we also used the HSE06 hybrid functional to calculate the electronic band structures of the MAPbI$_3$ by using the GGA−PBE + vdW-relaxed structures. The band structures of the MAPbI$_3$ calculated by the HSE-functional without SOC are also depicted in Figure 5e,f, and we can see that the

Manuscript published in ACS OMEGA

Table 2. Calculated Band Gaps (in eV) of the Studied MABX_3 Compounds for Different MA Orientations at Varying Levels of Approximation and Compared with the Available Experimental Data[a]

compounds	int. MA orient.	PBE	calculated band gap (eV)			QSGW+SOC	expt.
			PBE+SOC	HSE	QSGW		
MAPbI$_3$	[100]	1.55	0.47	1.99	2.47	1.79	1.55
	[110]	1.50	0.48				
	[111]	1.45	0.44	1.95	2.40	1.65	
MAPbBr$_3$	[100]	1.93	0.84	2.51	3.13	2.55	2.30
	[110]	1.86	0.84				
	[111]	1.80	0.70	2.43	3.01	2.28	
MAPbCl$_3$	[100]	2.41	1.30	3.10	3.91	3.49	2.90
	[110]	2.30	1.33				
	[111]	2.31	1.23	3.04	3.80	3.33	
MASnI$_3$	[100]	0.50	0.10	1.29			1.20
	[110]	0.47	0.10				
	[111]	0.49	0.10	1.26 (0.77)			
MASnBr$_3$	[100]	0.76	0.32	1.90			2.14
	[110]	0.76	0.38				
	[111]	0.75	0.30	1.88			
MASnCl$_3$	[100]	1.83	1.46	3.10			3.6
	[110]	1.33	1.03				
	[111]	1.49	1.06	2.94			

[a]Note: the HSE band gaps of Pb-based are obtained with 25% exact exchange, while the HSE band gaps of Sn-based are obtained with 55% exact exchange based on the experimental band gap of MASnI$_3$, and a number in parenthesis is obtained with 25% exact exchange.

indirect band gap persists when the screened hybrid functional is included. However, the calculated band gap of the MAPbI$_3$ by using the HSE06 lies in the range of 1.90−1.95 eV (see Table 2), larger than that one from the experimental value, as expected.

We note that indirect gaps or, more specifically, a displacement of the CBM away from the high symmetry point has previously been obtained due to the Rashba[15] effect. However, the results here are obtained without SOC and thus have a different origin: namely the distortions of the inorganic framework in response to the orientation of the MA molecules. The B-6p contributes to the CMB, while the X-5p and B-6s contribute to the VMB of these materials. From our calculated results, it is clear that the molecular orientation can strongly influence the electronic structure of the hybrid perovskites by affecting the X−B−X inorganic framework which take part in the frontier orbital and a little bit change the band gap of the materials, which will be discussed in the next section.

For the other studied compounds, the direct band gaps are also found in the case of the [111] orientation, while the indirect band gaps are found in all cases of distorted BX_6 octahedral due to the cation rotation. However, the GGA−PBE calculations now underestimate the band gap, as shown in Table 2, when compared with the experimental values. This shows that the good agreement for MAPbI$_3$ is really a coincidence, and less perfect cancellation of errors occurs in the other cases. The full band structures in GGA−PBE without SOC have significant errors even for methylammonium lead iodide. The electronic band structures of the other compounds are depicted in Figure 6. We can also see that the indirect band gaps persist for all studied compounds in the case of initial [100] orientation when the screened hybrid functional is included. The HSE-calculated band gap without SOC of MAPbBr$_3$ and MAPbCl$_3$ lies between 2.43 and 2.51 eV and 3.04 and 3.10 eV, respectively (see Table 2), which is slightly larger than the experimental values. The HSE-calculated band gap without SOC of Sn-based compounds lies in the 1.26−

1.29 eV range for MASnI$_3$, 1.88−1.90 eV for MASnBr$_3$, and 2.94−3.10 eV for MASnCl$_3$ which is slightly smaller than the experimental values (see Table 2).

While the above study indicates that the indirect gap found in the structures obtained from the initial [100] direction of the molecule is robust when considering different functionals, we need to further study the combined effect of SOC and the gap corrections beyond semilocal functionals. In fact, the distortion-induced shift of the CBM may be related to the closeness of the bands which remain nearly degenerate at the R-point when SOC is neglected. One might expect that adding SOC could remove this effect. However, when we add SOC alone without using hybrid functionals to open the gap, the latter will be so strongly reduced that the CBM is then close to the VBM and this may then lead to other artifacts. Instead of combining HSE with SOC, we decided here to use the QSGW +SO because it is in principle an even more accurate approach.

The band structures of the Pb-based compounds in QSGW approximation and at the GGA−PBE-relaxed structures are shown in Figure 7. We can see from our calculated results that the QSGW band structures of the initial [111] MA orientation exhibit the direct band gap at R-point both with and without SOC. On the other hand, the QSGW band structures of the near [10−1] MA$^+$ orientation are different: the CBM is slightly shifted from $R \rightarrow \Gamma$ as found in our DFT band structures without SOC. This indirect nature is already obtained in QSGW even without SOC. Nonetheless, the band structures are still substantially different when SOC is included, namely, they are spin-split and the origin of the indirect gap is now clearly affected by the Rashba effect.

Our calculated QSGW band structures in the case of MAPbI$_3$ are qualitatively consistent with the studies of Brivio et al.[15] results in which the representative [100] configuration of the MA$^+$ cation was selected. In their work, a similar spin-splitting of the CBM and a shift of the CBM away from the R-point is found. On the other hand, for a smaller NH$_4$ molecule instead of the MA, this Rashba effect is not observed. This is

Manuscript published in ACS OMEGA
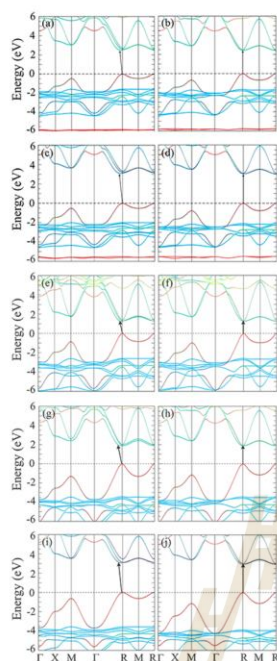
Figure 6. HSE-calculated band structures without SOC of the other studied compounds. (a,b) for MAPbBr$_3$, (c,d) for MAPbCl$_3$, (e,f) for MASnI$_3$, (g,h) for MASnBr$_3$, and (i,j) for MASnCl$_3$. Left and right panels represent the MA$^+$ cations initially oriented along [100] and [111] directions, respectively.
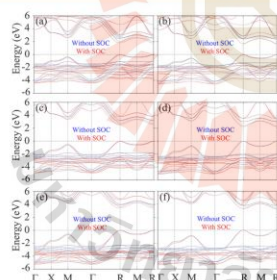

Figure 7. Calculated band structures in QSGW approximation with (red) and without (blue) SOC of the (a,b) CH$_3$NH$_3$PbI$_3$, (c,d) CH$_3$NH$_3$PbBr$_3$, and (e,f) CH$_3$NH$_3$PbCl$_3$. Left and right panels represent the MA$^+$ cation initially oriented along [100] and [111] directions, respectively.

because the NH$_4$ molecule has a much smaller molecular dipole character than the MA molecule. In recent work, the size of this effect was studied as a function of local distortions

obtained from molecular dynamics snapshots and found to be present even in CsPbI$_3$ due to the possibility of local Pb off-centering which like the MA molecules also can lead to the required symmetry breaking to have a Rashba effect.[15] Their calculated QSGW band gaps are 2.70 eV (SOC = 0) and 1.67 eV (added SOC). Our calculated band gaps in QSGW approximation are also listed in Table 2. We can see that the QSGW band gaps calculated without SOC are much larger than the experimental values, and the gaps are reduced by approximately 0.7 ± 0.1 eV when the SOC is considered. We note here that the orientations of the MA$^+$ cation are found to have an important impact on the nature of the band gap also at the level of QSGW approximation.

To further describe the indirect band gap, let us define the energy difference between the CBM and the conduction band at R-point of the Brillouin zone, $\Delta E \equiv E^R - E^{CBM}$, as shown by an inset in Figure 9. The PBE calculated ΔE of the studied
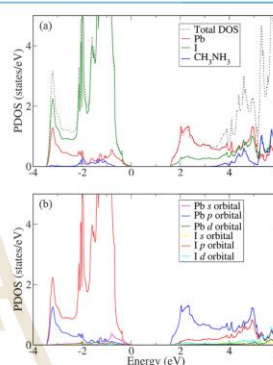
Figure 8. (a) Calculated total density of states (DOS) (dashed line) of CH$_3$NH$_3$PbI$_3$ for the case of [111]-oriented molecule and projected DOS (PDOS) on the Pb atom (red), I-atoms (green), and CH$_3$NH$_3$ (blue). (b) PDOS on orbitals of the Pb atom and I atoms.

compounds is depicted in Figure 9. From our calculated results, we can see that the ΔE of the Pb-based compounds is larger than that of the Sn-based compounds. This is resulting from the more distorted structure of the Pb-based compounds compared to the Sn-based ones. We note that the band gap
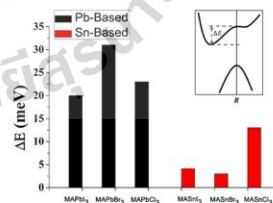
Figure 9. PBE-calculated energy difference, ΔE between the CBM and the conduction band at R-point (π/a, π/a, and π/a) of the Brillouin zone in the case of the indirect band gap.

Manuscript published in ACS OMEGA

shifting does not occur only with the $[10-1]$ orientation, the indirect band gap does appear for the equivalent orientations, for examples, $[10\pm1]$, $[01\pm1]$, and $[1\pm10]$. In addition, in the case of the $[101]$ orientation, the CBM shifts along the $R \rightarrow M$ line (Supporting Information, Figure S1).

The MA$^+$ cation has often been assumed to not have any significant contribution to the electronic structure around the band edges. From our calculated DOS results of MAPbI$_3$, it is obviously seen that the bottom of the conduction band mainly consists of the p orbitals of the Pb atom, while the top of the valence band is mainly derived from the p orbital of the I atoms and the Pb-s orbital, as depicted in Figure 8b. When considering the organic molecule, the highest occupied molecular orbital of the MA$^+$ cation is found deep below the valence band, $\sim$5 eV below the VBM. Thus, one may argue that there is no effect of the MA$^+$ cation in the optical and electronic response of such materials, rather it does only contribute to their structural cohesion by donating its charge to the rest of the system. However, a closer inspection of the DOS projected on the various atoms (Figure 8a) reveals that there is a small contribution of the MA cation, $\sim$0.5 eV below the VBM. This indicates that indeed there is an interaction between the MA cation and the inorganic PbI$_6$ octahedral framework in the form of hydrogen bonding. To further understand the effect of the interactions between the MA cation and the inorganic framework in electronic properties of these materials, we removed the MA cation from the PBE + vdW-relaxed structure of the initial $[100]$ orientation and calculated the electronic band structures. This is to check the interactions between the MA cation and the framework. Note that, by removing the MA cation, one electron is missing from the band, therefore there is a hole in the valence band and the Fermi-level shifted down, below the VBM. To do charge neutralizing, we added one electron to the system and then calculated the band structure. The calculated band structure in this case preserves the same feature of indirect band gap as one obtained from the MAPbI$_3$ unit cell (Supporting Information, Figure S2). This indicates that the MA cation in the system just donates its electron to the inorganic framework, it does not affect the band structure near the band edge. However, its orientations played a role in the relaxed structure of the inorganic framework and caused the structural distortion of the framework, leading to the symmetry breaking and the CBM is a bit shifted away from high symmetry point. In our cases, the rotation of the MA cation can create a variation of the band gap of MAPbI$_3$ $\sim$0.2 eV ($\sim$13% wrt. experimental gap of 1.55 eV), as shown in Figure 4d−f. Therefore, in the real system, the cation rotations would slightly change the band gap. The lowest and highest band gaps are found to be 1.43 and 1.64 eV which correspond to the calculated absorption spectrum of $\sim$865 and $\sim$756 nm, respectively. It is expected that the variation of the band gap for this material would be within 0.2 eV. The average band gap of MAPbI$_3$ is 1.54 eV which corresponded to the calculated absorption spectrum $\sim$805 nm. From all our calculated results, it has been revealed that the vdW correction is important to obtain an accurate description of the interactions between the MA cation and the inorganic framework for the structural relaxation of the halide perovskite system. This interaction induces the deformation of the PbI$_6$ octahedral framework, leading to the distorted structure of PbI$_6$ framework; the band structure is changed from direct to indirect band gap.

■ CONCLUSIONS

In this work, we have performed DFT + vdW correction calculations with various initial MA$^+$ cation orientations, namely $[100]$, $[110]$, and $[111]$ for revealing the effects of the internal interactions between the MA$^+$ cation and the BX_6 inorganic framework of the CH$_3$NH$_3$$BX_3$ (B = Pb, Sn; X = I, Br, Cl) halide perovskite materials. Our calculations reveal that the vdW interactions between the MA$^+$ cation and the inorganic framework are critical for internal geometry optimization and electronic properties calculations. Full structural relaxations, including vdW-corrected DFT, give the better agreement of the lattice parameters with the experimental values than obtained without them. More importantly, full relaxations, including vdW interactions of the MA cation initially oriented along the $[100]$ direction, give a strongly distorted structure of the BX_6 inorganic framework, which results from the MA$^+$ cation rotation and consequently affects the electronic band structure, which changes from direct to indirect band gap. On the other hand, the relaxations without vdW correction do not present enough distortion of the BX_6 inorganic framework, the electronic band structures remain direct band gap.

This result is found to be robust when considering different halogens and occurs in both Sn- and Pb-based compounds. It is also robust when using a more accurate hybrid functional or the GW method. Finally, the indirect gap is maintained for this orientation when including both quasiparticle self-energy corrections at the GW level and SOC. The latter leads to the Rashba effect which spin-splits the bands, but the indirect nature is already present before adding the SOC. This clearly demonstrates that the main origin of the indirect gap lies in the distortions resulting from the structural distortions of the organic ion with the inorganic framework.

Computational Methods. The structural properties of studied materials were predicted using the first-principle DFT which is implemented in the Vienna *ab initio* simulation package (VASP) code.[22,23] The semilocal GGAs combined with the PBE[24] functional are used as the primary exchange−correlation functional. The vdW corrections were also employed to study their effects on the structural and electronic properties of the materials. The projected augmented wave[23,25] method with plane-wave basis set cut-off energy of 520 eV is employed in all calculations. The conjugate gradient algorithm[26] is used for the structural optimization until the change of the energy on each atom is less than 1×10^{-4} eV. For the structural optimization and electronic properties calculations, the Monkhorst−Pack k-points sampling[27] with 8 × 8×8 mesh is used for the Brillouin-zone integrations. Recent studies[12−14] revealed that vdW force plays an important role in the range of materials with weak interactions, such as organic−inorganic halide perovskite compounds, especially in their geometry optimization. Therefore, in order to study the effects of internal interactions between the MA$^+$ cation and BX_6 inorganic framework, full structural relaxations (volume and atomic position are allowed to relax), including vdW interactions, have been performed using the zero damping DFT-D3 method described by Grimme et al.[28] Then, the relaxed structures have been used to calculate the corresponding electronic band structures both at the DFT and many-body perturbation theory GW level.[29−31]

The cubic primitive cell of the MABX_3 (12 atoms per unit cell) has been used in this work. As a matter of fact, under

working temperature, the MA molecules are nearly free to rotate inside the cuboctahedral BX_6. It is more important to investigate the range of the change in the energy level near the band edge. In this work, various MA orientations within the cubic unit cell have been studied in order to determine the range of variation of electronic structures as molecules rotating inside the perovskite cage. Our calculated results are able to qualitatively explain the change of CBM of MAPbI$_3$ which is affected by molecular rotational and is in good agreement with both other calculations using the supercell approach[13,16,19] and the experiment performed by Hutter et al.[32] The orientation of the MA cation significantly affects the BX_6 inorganic framework and consequently the electronic properties of the materials.

It is well known that the GGA−PBE usually underestimates band gaps of semiconductors. However, for MAPbI$_3$, the GGA−PBE without SOC gives fortuitously good agreement of the calculated band gap with the experimental measurement. This is due to a compensation of the errors of the GGA−PBE and the lack of SOC. Therefore, the more accurate HSE-screened hybrid functional (HSE06)[33] is also used to calculate the band structures without including SOC for the band gaps. It is well known that the DFT method treats core electrons by effective pseudopotential. In order to study the effects of core electrons, one may need the full-potential all-electron methods to explain the electronic properties of the materials. Subsequently, to compare with the DFT method, we also calculated the band structures using the full-potential linearized muffin-tin orbital all-electron method,[34,35] as implemented in Questaal Suite.[31] In this method, the band structures are calculated using the QSGW method.[35,36] The GW method is a many-body perturbation theoretical method introduced by Hedin[37,38] in which the self-energy is approximated in terms of the one-electron Green's function G and screened Coulomb interaction, W, schematically $\Sigma = iGW$. While the GW self-energy operator is energy-dependent and non-Hermitian in the QSGW approach, we replace it by an energy-independent but still non-local operator, determined in a self-consistent manner. From a starting independent particle Hamiltonian H_0, and its eigenvalues and eigenfunctions, we obtain both the Green's function G_0 and the polarization function P_0. The screened Coulomb interaction is then given by $W = v + vP_0W$, and the self-energy is obtained as $\Sigma = iG_0W_0$. This quantity is actually obtained in the basis set of the eigenstates of H_0. From it, we then extract a correction to the exchange correlation potential

$$[\Delta v_{xc}]_{ij} = \frac{1}{2} \text{Re} \left\{ \Sigma_{ij}(\varepsilon_i) + \Sigma_{ij}(\varepsilon_j) \right\} - v_{xc}^0$$

which is added to the previous H_0 to obtain a new H_0, and the procedure is iterated until $\Delta v_{xc} = 0$. At convergence, the quasiparticle energies equal the Kohn−Sham eigenvalues. Hence, the name quasiparticle self-consistent. The energy dependence of the GW self-energy and its imaginary part or lifetime are thus ignored, but the quasiparticle energies are correctly including the dynamical effects of the electron−electron interaction.

■ ASSOCIATED CONTENT

Ⓢ Supporting Information

The Supporting Information is available free of charge at https://pubs.acs.org/doi/10.1021/acsomega.0c03016.

Band structures of the fully relaxed crystal structure including vdW interactions calculated using the GGA−PBE without SOC of MAPbI3 for the MA cation initially orientated along the [101] direction; calculated band structures of the PBE + vdW-relaxed structure of the MAPbI3 unit cell with the MA cation initially orientated in the [100] direction; and calculated band structures of the PBE + vdW-relaxed structure of Pb−I host without the MA cation in the structure (PDF)

■ AUTHOR INFORMATION

Corresponding Author

Sirichok Jungthawan − *School of Physics, Institute of Science and Center of Excellence in Advanced Functional Materials, Suranaree University of Technology, Nakhon Ratchasima 30000, Thailand; Thailand Center of Excellence in Physics, Ministry of Higher Education, Science, Research and Innovation, Bangkok 10400, Thailand;* ● orcid.org/0000-0003-0989-6512; Email: sirichok@g.sut.ac.th

Authors

Narasak Pandech − *School of Physics, Institute of Science, Suranaree University of Technology, Nakhon Ratchasima 30000, Thailand; Thailand Center of Excellence in Physics, Ministry of Higher Education, Science, Research and Innovation, Bangkok 10400, Thailand*

Thanundon Kongnok − *School of Physics, Institute of Science, Suranaree University of Technology, Nakhon Ratchasima 30000, Thailand; Thailand Center of Excellence in Physics, Ministry of Higher Education, Science, Research and Innovation, Bangkok 10400, Thailand*

Nirawith Palakawong − *School of Physics, Institute of Science, Suranaree University of Technology, Nakhon Ratchasima 30000, Thailand; Thailand Center of Excellence in Physics, Ministry of Higher Education, Science, Research and Innovation, Bangkok 10400, Thailand*

Sukit Limpijumnong − *School of Physics, Institute of Science, Suranaree University of Technology, Nakhon Ratchasima 30000, Thailand; The Institute for the Promotion of Teaching Science and Technology, Bangkok 10110, Thailand*

Walter R. L. Lambrecht − *Department of Physics, Case Western Reserve University, Cleveland, Ohio 44106-7079, United States;* ● orcid.org/0000-0002-5377-0143

Complete contact information is available at: https://pubs.acs.org/10.1021/acsomega.0c03016

Notes

The authors declare no competing financial interest.

Manuscript published in ACS OMEGA

■ REFERENCES

(1) Poglitsch, A.; Weber, D. Dynamic disorder in methylammoniumtrihalogenoplumbates (II)observed by millimeter-wave spectroscopy. *J. Chem. Phys.* **1987**, *87*, 6373−6378.

(2) Kojima, A.; Teshima, K.; Shirai, Y.; Miyasaka, T. Organometal Halide Perovskites as Visible-Light Sensitizers for Photovoltaic Cells. *J. Am. Chem. Soc.* **2009**, *131*, 6050−6051.

(3) Stoumpos, C. C.; Malliakas, C. D.; Kanatzidis, M. G. Semiconducting Tin and Lead Iodide Perovskites with Organic Cations: Phase Transitions, High Mobilities, and Near-Infrared Photoluminescent Properties. *Inorg. Chem.* **2013**, *52*, 9019−9038.

(4) Park, J.-S.; Choi, S.; Yan, Y.; Yang, Y.; Luther, J. M.; Wei, S.-H.; Parilla, P.; Zhu, K. Electronic Structure and Optical Properties of α-$CH_3NH_3PbBr_3$ Perovskite Single Crystal. *J. Phys. Chem. Lett.* **2015**, *6*, 4304−4308.

(5) Weller, M. T.; Weber, O. J.; Henry, P. F.; Di Pumpo, A. M.; Hansen, T. C. Complete structure and cation orientation in the perovskite photovoltaic methylammonium lead iodide between 100 and 352 K. *Chem. Commun.* **2015**, *51*, 4180−4183.

(6) Sahoo, S. K.; Manoharan, B.; Sivakumar, N. Chapter 1—Introduction: Why Perovskite and Perovskite Solar Cells? In *Perovskite Photovoltaics*; Thomas, S., Thankappan, A., Eds.; Academic Press, 2018; pp 1−24.

(7) Tonui, P.; Oseni, S. O.; Sharma, G.; Yan, Q.; Tessema Mola, G. Perovskites photovoltaic solar cells: An overview of current status. *Renewable Sustainable Energy Rev.* **2018**, *91*, 1025−1044.

(8) Shi, Z.; Jayatissa, A. Perovskites-Based Solar Cells: A Review of Recent Progress, Materials and Processing Methods. *Materials* **2018**, *11*, 729.

(9) Whitfield, P. S.; Herron, N.; Guise, W. E.; Page, K.; Cheng, Y. Q.; Milas, I.; Crawford, M. K. Structures, Phase Transitions and Tricritical Behavior of the Hybrid Perovskite Methyl Ammonium Lead Iodide. *Sci. Rep.* **2016**, *6*, 35685.

(10) Quarti, C.; Mosconi, E.; De Angelis, F. Interplay of Orientational Order and Electronic Structure in Methylammonium Lead Iodide: Implications for Solar Cell Operation. *Chem. Mater.* **2014**, *26*, 6557−6569.

(11) Knop, O.; Wasylishen, R. E.; White, M. A.; Cameron, T. S.; Oort, M. J. M. V. Alkylammonium lead halides. Part 2. $CH_3NH_3PbX_3$ (X = Cl, Br, I) perovskites: cuboctahedral halide cages with isotropic cation reorientation. *Can. J. Chem.* **1990**, *68*, 412−422.

(12) Egger, D. A.; Kronik, L. Role of Dispersive Interactions in Determining Structural Properties of Organic−Inorganic Halide Perovskites: Insights from First-Principles Calculations. *J. Phys. Chem. Lett.* **2014**, *5*, 2728−2733.

(13) Li, J.; Rinke, P. Atomic structure of metal-halide perovskites from first principles: The chicken-and-egg paradox of the organic-inorganic interaction. *Phys. Rev. B* **2016**, *94*, 045201.

(14) Yin, W.-J.; Shi, T.; Yan, Y. Unusual defect physics in $CH_3NH_3PbI_3$ perovskite solar cell absorber. *Appl. Phys. Lett.* **2014**, *104*, 063903.

(15) Brivio, F.; Butler, K. T.; Walsh, A.; van Schilfgaarde, M. Relativistic quasiparticle self-consistent electronic structure of hybrid halide perovskite photovoltaic absorbers. *Phys. Rev. B: Condens. Matter Mater. Phys.* **2014**, *89*, 155204.

(16) Motta, C.; El-Mellouhi, F.; Kais, S.; Tabet, N.; Alharbi, F.; Sanvito, S. Revealing the role of organic cations in hybrid halide perovskite $CH_3NH_3PbI_3$. *Nat. Commun.* **2015**, *6*, 7026.

(17) Bechtel, J. S.; Seshadri, R.; Van der Ven, A. Energy Landscape of Molecular Motion in Cubic Methylammonium Lead Iodide from First-Principles. *J. Phys. Chem. C* **2016**, *120*, 12403−12410.

(18) Chiarella, F.; Zappettini, A.; Licci, F.; Borriello, I.; Cantele, G.; Ninno, D.; Cassinese, A.; Vaglio, R. Combined experimental and theoretical investigation of optical, structural, and electronic properties of $CH_3NH_3SnX_3$ thin films (X=Cl, Br). *Phys. Rev. B: Condens. Matter Mater. Phys.* **2008**, *77*, 045129.

(19) Xu, Q.; Stroppa, A.; Lv, J.; Zhao, X.; Yang, D.; Biswas, K.; Zhang, L. Impact of organic molecule rotation on the optoelectronic

properties of hybrid halide perovskites. *Phys. Rev. Mater.* **2019**, *3*, 125401.

(20) Lee, M. M.; Teuscher, J.; Miyasaka, T.; Murakami, T. N.; Snaith, H. J. Efficient Hybrid Solar Cells Based on Meso-Superstructured Organometal Halide Perovskites. *Sci* **2012**, *338*, 643.

(21) Mosconi, E.; Amat, A.; Nazeeruddin, M. K.; Grätzel, M.; De Angelis, F. First-Principles Modeling of Mixed Halide Organometal Perovskites for Photovoltaic Applications. *J. Phys. Chem. C* **2013**, *117*, 13902−13913.

(22) Kresse, G.; Furthmüller, J. Efficient iterative schemes for ab initio total-energy calculations using a plane-wave basis set. *Phys. Rev. B: Condens. Matter Mater. Phys.* **1996**, *54*, 11169−11186.

(23) Kresse, G.; Joubert, D. From ultrasoft pseudopotentials to the projector augmented-wave method. *Phys. Rev. B: Condens. Matter Mater. Phys.* **1999**, *59*, 1758−1775.

(24) Perdew, J. P.; Burke, K.; Ernzerhof, M. Generalized Gradient Approximation Made Simple. *Phys. Rev. Lett.* **1996**, *77*, 3865−3868.

(25) Blöchl, P. E. Projector augmented-wave method. *Phys. Rev. B: Condens. Matter Mater. Phys.* **1994**, *50*, 17953−17979.

(26) Golub, G. H.; Ye, Q. Inexact Preconditioned Conjugate Gradient Method with Inner-Outer Iteration. *SIAM J. Sci. Comput.* **1999**, *21*, 1305−1320.

(27) Monkhorst, H. J.; Pack, J. D. Special points for Brillouin-zone integrations. *Phys. Rev. B: Condens. Matter Mater. Phys.* **1976**, *13*, 5188−5192.

(28) Grimme, S.; Antony, J.; Ehrlich, S.; Krieg, H. A consistent and accurate ab initio parametrization of density functional dispersion correction (DFT-D) for the 94 elements H-Pu. *J. Chem. Phys.* **2010**, *132*, 154104.

(29) Bhandari, C.; Lambrecht, W. R. L.; van Schilfgaarde, M. Quasiparticle self-consistent GW calculations of the electronic band structure of bulk and monolayer V_2O_5. *Phys. Rev. B: Condens. Matter Mater. Phys.* **2015**, *91*, 125116.

(30) Bhandari, C.; van Schilgaarde, M.; Kotani, T.; Lambrecht, W. R. L. All-electron quasiparticle self-consistent GW band structures for $SrTiO_3$ including lattice polarization corrections in different phases. *Phys. Rev. Mater.* **2018**, *2*, 013807.

(31) Pashov, D.; Acharya, S.; Lambrecht, W. R. L.; Jackson, J.; Belashchenko, K. D.; Chantis, A.; Jamet, F.; van Schilfgaarde, M. Questaal: A package of electronic structure methods based on the linear muffin-tin orbital technique. *Comput. Phys. Commun.* **2020**, *249*, 107065.

(32) Hutter, E. M.; Gélvez-Rueda, M. C.; Osherov, A.; Bulović, V.; Grozema, F. C.; Stranks, S. D.; Savenije, T. J. Direct−indirect character of the bandgap in methylammonium lead iodide perovskite. *Nat. Mater.* **2017**, *16*, 115−120.

(33) Heyd, J.; Scuseria, G. E.; Ernzerhof, M. Hybrid functionals based on a screened Coulomb potential. *J. Chem. Phys.* **2003**, *118*, 8207−8215.

(34) Methfessel, M.; van Schilfgaarde, M.; Casali, R. A. In *A Full-Potential LMTO Method Based on Smooth Hankel Functions, Electronic Structure and Physical Properties of Solids*; Dreyssé, H., Ed.; Springer Berlin Heidelberg: Berlin, Heidelberg, 2000; pp 114−147.

(35) Kotani, T.; van Schilfgaarde, M.; Faleev, S. V. Quasiparticle self-consistent GW method: A basis for the independent-particle approximation. *Phys. Rev. B: Condens. Matter Mater. Phys.* **2007**, *76*, 165106.

(36) van Schilfgaarde, M.; Kotani, T.; Faleev, S. Quasiparticle Self-Consistent GW Theory. *Phys. Rev. Lett.* **2006**, *96*, 226402.

(37) Hedin, L. New Method for Calculating the One-Particle Green's Function with Application to the Electron-Gas Problem. *Phys. Rev.* **1965**, *139*, A796−A823.

(38) Hedin, L.; Lundqvist, S. Effects of Electron-Electron and Electron-Phonon Interactions on the One-Electron States of Solids. In *Solid State Physics*; Seitz, F., Turnbull, D., Ehrenreich, H., Eds.; Academic Press, 1970; Vol. 23, pp 1−181.

First-Principles Study of Alkali Metal Intercalated in 2H-MoS₂

Thanundon Kongnok,[1,*] Sirichok Jungthawan,[1,2] and Sukit Limpijumnong[1,2]
[1] School of Physics and NANOTEC-SUT Center of Excellence on Advanced Functional Nanomaterials, Suranaree University of Technology, Nakhon Ratchasima 30000, Thailand
[2] Thailand Center of Excellence in Physics (ThEP), Commission on Higher Education, Bangkok 10400, Thailand
*e-mail: Thanundon_kongnok@hotmail.com

Abstract: MoS_2 is Transition Metal Dichalcogenide (TMDC) material and semiconductor having layered honeycomb structure (2H). MoS_2 monolayers are bounded weakly by the Van der Waals interaction. In the bulk form, MoS_2 has an indirect band gap where valence band maximum and conduction band minimum are located at the Γ point and the middle point between Γ-K point, respectively. But in monolayer form the band gap becomes direct and is located at the K point. The electronic characteristic of the monolayer can be reproduced in the MoS_2 bulk by means of alkali metal intercalation such as Li, Na, K, and Rb into the interlayer spacing. With different atomic radii, the expansion of the interlayer spacing is tunable. The interactions between the layers can be investigated by varying the type of alkali metal elements. For K intercalation, the expansion is large enough to reduce the electronic interactions between the monolayers creating a quasi-monolayer character. In this work, the effects of alkali metal intercalation are investigated by using first-principles calculations. The results show that the band gap is gradually increased with increasing interlayer spacing. The band gap type is changed from indirect to direct caused by the expansion of the interlayer spacing between the layers and the contribution of electron donation from alkali metal to the conduction states of MoS_2. The characteristic of these delocalized states on the MoS_2 layer slightly increase the lattice parameter of MoS_2 layer. The plot of the difference of charge density between intercalated MoS_2 and pristine MoS_2 indicates electron migration from S and intercalated alkali metal to d_z^2 atomic orbital of Mo. Our results suggest that the different atomic size of intercalated alkali metals could provide an opportunity to tune the interactions between the layers of TMDC material.

Abstract submitted for the Siam Physics Congress 2016, Ubon Ratchathani (2016)

First-Principles Study of Alkali Metal Intercalated in 2H-MoS$_2$

Thanundon Kongnok,[1, *] Sirichok Jungthawan,[1, 3] and Sukit Limpijumnong[1, 2, 3]

[1] School of Physics, Institute of Science, and NANOTEC-SUT Center of Excellence on Advanced Functional Nanomaterials, Suranaree University of Technology, Nakhon Ratchasima 30000, Thailand

[2] Thailand Center of Excellence in Physics (ThEP), Commission on Higher Education, Bangkok 10400, Thailand

[3] Synchrotron Light Research Institute, Nakhon Ratchasima 30000, Thailand

*e-mail: Thanundon_kongnok@hotmail.com

Abstract: MoS$_2$ is a compound in transition metal dichalcogenide (TMDC) family that is semiconductor with layered honeycomb structure (2H) having strong in-plane bonding and weak out-of-plane van der Waals (VDW) interactions. In the bulk form, MoS$_2$ has an indirect band gap where valence band maximum and conduction band minimum are located at the Γ point and the middle point between Γ-K point, respectively. Alternatively, the monolayer form has direct band gap (at the K point) which is more suitable for device applications. However, exfoliation of bulk MoS$_2$ into monolayer results in a considerable defect density that has extremely low photoluminescence quantum yield. It has been proposed that the electronic characteristic of the monolayer can be reproduced experimentally in MoS$_2$ by K intercalation [1]. In this work, the effects of alkali metal intercalation (such as Li, Na, K, and Rb) are investigated by using first-principles calculations. The results show significant expansion of interlayer spacing and contribution of electron donation from alkali metal to the conduction band of MoS$_2$. The expansion of the interlayer spacing depends on atomic radii of the intercalated metals. Moreover, band gap type is changed from indirect to direct because of the expansion of the interlayer spacing reduces the electronic interactions between adjacent layers creating a quasi-monolayer character. The effects of K concentration have been investigated by varying the number of K atoms in the 2×2×1 supercell of MoS$_2$K$_x$ (where x = 0.25, 0.50, 0.75 and 1.00). In order to compare the results from supercell calculations with the primitive cell, the electronic structures from supercell calculations are unfolded [2] onto the high symmetry paths as defined in the first Brillouin zone of the primitive cell. It has been found that the interlayer spacing of MoS$_2$K$_{0.25}$ is large enough to exhibit quasi-monolayer character. The unfolded electronic structures show a direct band gap located at the K point with larger band gap than bulk MoS$_2$. The Fermi level is a bit higher than conduction band minimum due to electron donation from alkali metal. Our results suggest that different atomic radii and concentration of intercalated alkali metals could provide an opportunity to tune band gap type and value of TMDC materials.

[1]   Eknapakul, T., et al., *Electronic structure of a quasi-freestanding MoS(2) monolayer.* Nano Lett, 2014. **14**(3): p. 1312-6.

[2]   Tomić, M., H.O. Jeschke, and R. Valentí, *Unfolding of electronic structure through induced representations of space groups: Application to Fe-based superconductors.* Physical Review B, 2014. **90**(19).

Abstract submitted for the International Union of Materials Research Societies-
International Conference in Asia 2020, Chiang Mai (2020)

Unfolding of supercell-band structure from density functional theory calculation and visualization of the unfolded band with orbital-projected.

Thanundon Kongnok[a,*], Sirichok Jungthawan[a, b, c]

[a]School of Physics, Institute of Science, and NANOTEC-SUT Center of Excellence on Advanced Functional Nanomaterials, Suranaree University of Technology, Nakhon Ratchasima 30000, Thailand
[b]Center of Excellence in Advanced Functional Materials, Suranaree University of Technology, Nakhon Ratchasima, 30000, Thailand
[c] Thailand Center of Excellence in Physics, Ministry of Higher Education, Science, Research and Innovation, 328 Si Ayutthaya Road, Bangkok, 10400, Thailand

*Corresponding Author's E-mail: kongnok.t@gmail.com

Abstract

Density functional theory (DFT) plays an important role in studying many physical properties of various materials. For periodic boundary condition, Bloch theorem is mainly used in the calculations due to the translational symmetry. A problem arises in the practical use of DFT calculations whenever we encounter with systems that the original translational symmetry is broken such as defect calculations. Supercell calculations are inevitable where its size determines the periodicity of the band structure through the Bloch theorem. This results in a smaller Brillion zone compared with the Brillion zone of primitive cell and a folded band structure consisting of many folded bands. The folding of the band structure raises complication and difficulty in interpretation of the results from electronic band structures measurement data such as angle-resolved photoemission spectroscopy (ARPES) which is a direct measurement of band structure. The problem can be alleviated by unfolding of the folded bands through induced representations of space group reported by Tomić and co-workers [1]. The unfolding method provides an opportunity to study electronic structures of real materials, that are imperfect, allowing ones to compare the unfolded band structures with experimental results. The visualization of the unfolded bands with orbital-projected by a Python script so-called PROPLOT will be given in this talk.

"Keywords: unfolding method; defect calculations; orbital-projected"

References
[1] *Tomić, M., H.O. Jeschke, and R. Valentí, Unfolding of electronic structure through induced representations of space groups: Application to Fe-based superconductors. 2014. Physical Review B, 90(19): 195121*

First-Principles Study of Alkali Metal Intercalated in Transition Metal Dichalcogenides

Thanundon Kongnok,[1] Sirichok Jungthawan,[1,2] and Sukit Limpijumnong[1,2]

[1] *School of Physics and NANOTEC-SUT Center of Excellence on Advanced Functional Nanomaterials, Suranaree University of Technology, Nakhon Ratchasima 30000, Thailand*
[2] *Thailand Center of Excellence in Physics (ThEP), Commission on Higher Education, Bangkok 10400, Thailand*

Transition Metal Dichalcogenides (TMDC) materials are semiconductors having layered structure, such as MoS_2, $MoSe_2$, $MoTe_2$, WS_2, WSe_2 and WTe_2. In these layered structure, TMDCs monolayers are bounded weakly by the Van der Waals interaction. In the bulk form, these TMDCs have an indirect band gap where valence band maximum and conduction band minimum are located at the Γ point and near the middle point between Γ-K point, respectively. However, the band gap of a monolayer TMDC is direct and is located at the K point. The electronic characteristic of the monolayer can be restored in the layered structure TMDCs by intercalating alkali metal such as Li, Na, K, and Rb in the interlayer gap [1]. The expansion of the interlayer gap is large enough to reduce the electronic interaction between the monolayers; creating a quasi-monolayer character. In this work, the effects of the intercalation are investigated by using first-principles calculations. The results show that the band gap is increased and changes from indirect to direct; caused by the expansion of the interlayer spacing between layers and the contribution of electrons from alkali metal to the conduction band. The contributed electrons from the intercalated metal into the conduction band are delocalized in the layer that slightly increases the lattice constant. Our results suggested that the different atomic size of intercalated alkali metals provides an opportunity to tune the interlayer spacing, hence, electronic characteristics for broad applications in nanoelectronics and optoelectronics.

[1] T. Eknapakul, P. D. C. King, M. Asakawa, P. Buaphet, R.-H. He, S.-K. Mo, H. Takagi, K. M. Shen, F. Baumberger, T. Sasagawa, S. Jungthawan, and W. Meevasana, Nano Lett. **14**, 1312 (2014).

Contact: Thanundon_kongnok@hotmail.com

ABSTRACT:

First-Principles Study of Electronic and Optical Properties of Alkali Metal Intercalated Transition Metal Dichalcogenides

Thanundon Kongnok[1,*], Sukit Limpijumnong[1,2,3] and Sirichok Jungthawan[1,2]

[1] *School of Physics, Institute of Science, and NANOTEC-SUT Center of Excellence on Advanced Functional Nanomaterials, Suranaree University of Technology, Nakhon Ratchasima 30000, Thailand*
[2] *Thailand Center of Excellence in Physics (ThEP), Commission on Higher Education, Bangkok 10400, Thailand*
[3] *Synchrotron Light Research Institute, Nakhon Ratchasima 30000, Thailand*

*Presenting author's email: Kongnok.t@gmail.com

MoS_2 is a compound in transition metal dichalcogenide (TMDC) family that is semiconductor with layered honeycomb structure having strong in-plane bonding and weak out-of-plane van der Waals interactions. In the bulk form, MoS_2 has an indirect band gap, whereas monolayer form has direct band gap which is more suitable for device applications. It has been proposed that the electronic characteristic of the monolayer can be reproduced experimentally in MoS_2 by K intercalation [1]. In this work, the effects of alkali metal (such as Li, Na, K, and Rb) intercalation are investigated by using first-principles calculations in the 2×2×1 supercell. The electronic structures from supercell calculations are unfolded [2] onto the high symmetry paths as defined in the first Brillouin zone of the primitive cell. The results show significant expansion of interlayer spacing and contribution of electron donation from alkali metal to the conduction band of MoS_2. The expansion obviously depends on atomic radii of the intercalated metals. Moreover, band gap type is changed from indirect to direct because the expansion of the interlayer spacing reduces the electronic interactions between adjacent layers creating a quasi-monolayer character. It has been found that the interlayer spacing of $MoS_2K_{0.25}$ and $MoS_2Rb_{0.25}$ are large enough to exhibit quasi-monolayer character. Furthermore, the effects of concentration of alkali metal have been investigated by varying concentration of K. We found that in-plane lattice constant increases proportional to the concentration. Our results suggest that different atomic radii and concentration of intercalated alkali metals could provide an opportunity to tune electronic structures of TMDC materials.

First-Principles Study of Electronic and Optical Properties of Alkali Metal Intercalated Transition Metal Dichalcogenides

Thanundon Kongnok (1), Sukit Limpijumnong (1,2,3) and Sirichok Jungthawan (1,2)

(1) School of Physics, Institute of Science, and NANOTEC-SUT Center of Excellence on Advanced Functional Nanomaterials, Suranaree University of Technology, Nakhon Ratchasima 30000, Thailand; (2) Thailand Center of Excellence in Physics (ThEP), Commission on Higher Education, Bangkok 10400, Thailand; (3) Synchrotron Light Research Institute, Nakhon Ratchasima 30000, Thailand

Presenting author's email: Kongnok.t@gmail.com

MoS_2 is a compound in transition metal dichalcogenide (TMDC) family that is semiconductor with layered honeycomb structure having strong in-plane bonding and weak out-of-plane van der Waals interactions. In the bulk form, MoS_2 has an indirect band gap, whereas monolayer form has direct band gap which is more suitable for device applications. It has been proposed that the electronic characteristic of the monolayer can be reproduced experimentally in MoS_2 by K intercalation [1]. In this work, the effects of alkali metal (such as Li, Na, K, and Rb) intercalation are investigated by using first-principles calculations in the 2×2×1 supercell. The electronic structures from supercell calculations are unfolded [2] onto the high symmetry paths as defined in the first Brillouin zone of the primitive cell. The results show significant expansion of interlayer spacing and contribution of electron donation from alkali metal to the conduction band of MoS_2. The expansion obviously depends on atomic radii of the intercalated metals. Moreover, band gap type is changed from indirect to direct because the expansion of the interlayer spacing reduces the electronic interactions between adjacent layers creating a quasi-monolayer character. It has been found that the interlayer spacing of $MoS_2K_{0.25}$ and $MoS_2Rb_{0.25}$ are large enough to exhibit quasi-monolayer character. Furthermore, the effects of concentration of alkali metal have been investigated by varying concentration of K. We found that in-plane lattice constant increases proportional to the concentration. Our results suggest that different atomic radii and concentration of intercalated alkali metals could provide an opportunity to tune electronic structures of TMDC materials.

References
[1] Eknapakul, T., et al., Electronic structure of a quasi-freestanding MoS_2 monolayer. 2014. Nano Lett **14(3)**: 1312-6.
[2] Tomić, M., H.O. Jeschke, and R. Valentí, Unfolding of electronic structure through induced representations of space groups: Application to Fe-based superconductors. 2014. Physical Review B, **90(19)**: 195121.

CURRICULUM VITAE

Mr. Thanundon Kongnok was born on May 30, 1990 in Khon Kaen, Thailand. He received his bachelor's degree in science in 2012 from the Department of Physics, Faculty of Science, Khon Kaen University. In 2013, he got a scholarship from External Grants and Scholarships for Graduate Students (OROG) at Suranaree University of Technology to support his tuition fees. He also proudly received a scholarship from the Thailand Research Fund (TRF) to pursue the Ph.D. program at the School of Physics, Suranaree University of Technology, under the supervision of Assoc. Prof. Dr. Sirichok Jungthawan. He published an article in an international journal and participated in several national and international conferences during the course of his Ph.D. program. Details of the publication and abstracts of his presentations can be found in Appendix B.